Structuring light from optical spin-orbit interaction

Vagharshak Hakobyan

université de BORDEAUX

THÈSE PRÉSENTÉE

POUR OBTENIR LE GRADE DE

DOCTEUR DE L'UNIVERSITÉ DE BORDEAUX

ECOLE DOCTORALE DES SCIENCES PHYSIQUES DE L'INGÉNIEUR

SPÉCIALITE : LASER, MATIÈRE ET NANOSCIENCESS

par Vagharshak HAKOBYAN

MISE EN FORME DE LA LUMIÈRE PAR INTERACTION SPIN-ORBITE OPTIQUE

Structuring light from optical spin-orbit interaction

Sous la direction de : Etienne BRASSELET

Soutenue le 28/11/2024

Membres du jury :

M. BRASSELET Etienne	Directeur de recherche	Université de Bordeaux	Directeur de thèse
M. ALONSO Miguel	Professeur	Aix Marseille Université	Présidente
M. GROSJEAN Thierry	Directeur de recherche	Institut Femto-ST	Rapporteur
M. GUILLON Marc	Maitre de conférences	University Paris Cité	Rapporteur
M. MAIRESSE Yann	Directeur de recherche	Université de Bordeaux	Examinateur

Acknowledgments

I want to convey my deep appreciation to my scientific advisor Etienne Brasselet. I'm grateful for his trust, support, and the valuable knowledge he has shared with me throughout my PhD journey. I would like to extend my sincere gratitude to the committee members Thierry Grosjean, Marc Guillon, Miguel Alonso, and Yann Mairesse for their valuable work, comments and suggestions, which all have contributed to enhance the quality of my thesis.

I deeply appreciate the contributions of all my collaborators and coauthors on the carried research and publications associated with this work. A special thanks to Andrew Forbes, Keshaan, Mwezi and the Structured Light Laboratory for their hospitality during my visits and the research projects we have undertaken together. I am grateful to my team members, Samlan, Nicolas, Emma, Elena, Georgiy, Gregorio, Mufeeduzaman, Rasi, Nina, and Delphine, for generously sharing their time, knowledge, and resources with me. I would also like to express my appreciation to the friendly and professional staff at Laboratoire Ondes et Matière d'Aquitaine for welcoming me into this scientific community and providing a supportive working environment.

To all my friends, thank you for your consistent support, companionship and the time we have shared together during this journey. Lastly, I would like to express my deepest gratitude to my family, to whom my thesis is dedicated, for their unwavering support and encouragement, which have been essential in helping me navigate and complete my PhD journey.

Titre : Mise en forme de la lumière par interaction spin-orbite optique

Résumé : L'interaction spin-orbite pour la lumière permet le couplage entre les degrés de liberté associés à l'état de polarisation de la lumière et ceux associés à l'espace. Ce couplage est particulièrement important dans les milieux qui sont à la fois inhomogènes et anisotropes. Dans ce travail, nous exploitons la mise en forme des propriétés de biréfringence artificielle ou naturelles de matériaux optiques tels que la silice, le nitrure de silicium, le silicium ou les cristaux liquides pour façonner différentes propriétés d'un faisceau lumineux. En particulier, nous démontrons la réalisation d'éléments optiques originaux permettant la transformation d'un faisceau gaussien en un faisceau de Laguerre-Gauss. En exploitant la superposition de tels modes générés par le couplage spin-orbite optique, nous montrons qu'il est possible de façonner des textures de polarisation de type skyrmion. Enfin, en tirant parti de la dépendance en longueur d'onde du niveau d'interaction spin-orbite, des dispositifs électro-optiques à base de cristaux liquides sont proposés pour moduler spectralement la topologie de la distribution de phase spatiale du champ lumineux, ce qui ouvre un champ d'applications dans la mise en forme d'impulsions optiques ultra-brèves.

Mots clés : Lumière structurée, Mise en forme de faisceau, Interaction spin-orbite, Modalité, Optique, Moment angulaire de la lumière

---

Title : Structuring light from optical spin-orbit interaction

Abstract : The spin-orbit interaction for light allows coupling between the degrees of freedom associated with the polarization state of light and those associated with space. Such coupling is particularly important in media that are both inhomogeneous and anisotropic. In this work, we exploit the shaping of artificial or natural birefringence properties of optical materials such as silica, silicon nitride, silicon, or liquid crystals to shape different properties of a light beam. In particular, we demonstrate the realization of original optical elements that allow the transformation of a Gaussian beam into a Laguerre-Gauss beam. By exploiting the superposition of such modes generated by optical spin-orbit coupling, we show that it is possible to shape skyrmion-like polarization textures. Finally, by exploiting the wavelength dependence of the level of spin-orbit interaction, liquid crystal-based electro-optical devices are proposed to spectrally modulate the topology of the spatial phase distribution of the light field, opening a field of applications in the shaping of ultrashort optical pulses.

Keywords: Structured light, Beam shaping, Spin-orbit interaction, Modality, Optics, Light angular momentum

---

Unité de recherche

Labartoire Ondes et Matière d'Aquitaine (UMR 5798), Université de Bordeaux, 351 Cours de la Libération, 33405 Talence cedex, France

Contents

CHAPTER 1

Structured light

The shaping of light in both temporal and spatial domains is a fundamental requirement of modern photonics technologies, today referred to as structured light [1]. This concept involves the precise control, both in space and time, of various degrees of freedom in light fields, such as spectrum, amplitude, phase, and polarization. The ability to tailor these aspects of light has become increasingly important for both fundamental research and practical applications in optics and photonics, for instance in high-resolution imaging, optical communication, quantum information processing, and advanced materials science.

1.1 Background

1.1.1 Gaussian beam

We start by introducing a Gaussian beam which is the fundamental solution of the paraxial scalar Helmholtz equation and that is the incident beam to which we apply various kinds of structuring strategies, each of them typically corresponding to a chapter of this thesis work. Within a complex representation framework, the corresponding electric field for a monochromatic fully polarized Gaussian beam of power $\mathcal{P}$ with wavelength λ, propagating along the z axis, is described as

$$\mathbf{E}(r,z,t) = \sqrt{\frac{2\mathcal{P}}{\pi\epsilon_0 c}}\frac{1}{w(z)}\exp\Big[\frac{-r^2}{w^2(z)}\Big]\exp\Big[\frac{ik_0r^2}{2R(z)}\Big]\exp[-iG(z)]\exp(i(k_0z-\omega t))\mathbf{e} \quad (1.1)$$

where

- ϵ_0 is the vacuum permittivity, and c is the speed of light in vacuum,
- $w(z) = w_0\sqrt{1+z^2/z_R^2}$ is the beam radius at a given z, where w_0 is the waist (minimum radius) of the beam, and $z_R = \pi w_0^2/\lambda$ is the Rayleigh distance,
- $k_0 = 2\pi/\lambda$ is the wavevector that defines the propagation direction,

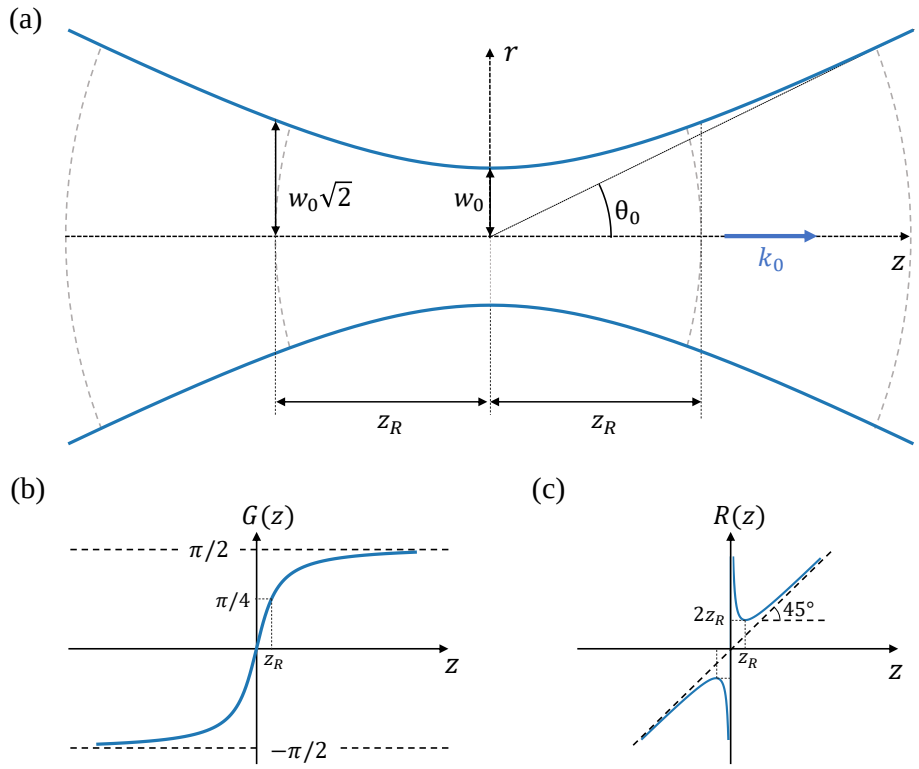

Figure 1.1 Illustration of Gaussian beam. (a) The solid curves refer to the locations, in the meridional plane (r, z), where the intensity equals $\exp(-2)$ of its on-axis ($r = 0$) value. w_0 is the beam waist at $z = 0$, z_R is the Rayleigh length at which the curvature $1/R(z)$ is maximal and for which the beam waist radius $w(z_R) = w_0\sqrt{2}$, and $\theta_0 = \frac{\lambda}{\pi w_0}$ is the characteristic divergence angle of the beam. (b) The Gouy phase reaches its asymptotic $\pm\pi/2$ values as $z \to \pm\infty$, respectively. (c) The radius of curvature reaches its minimum value at $z = z_R$ and asymptotically approaches a slope of 1, corresponding to a 45° angle with respect to the z axis as $z \to \pm\infty$.

- $G(z) = \arctan(z/z_R)$ is the Gouy phase,
- ω is the angular frequency of the electric field,
- $R(z) = z[1 + (z_R/z)^2]$ is the radius of curvature of the optical wavefront
- **e** is a complex unit vector defining the polarization state of light. It defines how the electric field evolves with time at a given position and is presented with more details in the next section.

A simple schematic representation of a Gaussian beam is shown in Fig. 1.1. In addition to amplitude and phase, polarization is another property of light whose description and possible transformation in the presence of light-matter interaction will be briefly presented in what follows within our specific context. We refer to [2] for a tutorial overview of how to describe the polarization state of light.

1.1.2 Polarization state of light

In general, the polarization state of paraxial light is represented as a 2D complex vector. For fully polarized light it can be described as

$$\mathbf{e}(x,y) = (\cos\psi\cos\chi - i\sin\psi\sin\chi)\mathbf{x} + (\sin\psi\cos\chi + i\cos\psi\sin\chi)\mathbf{y} \tag{1.2}$$

where $0 \le \psi \le \pi$ is the azimuth angle between the major axis of the so-called polarization ellipse and the x axis, and $-\pi/4 \le \chi \le \pi/4$ is the ellipticity angle, $\tan\chi$ being the signed ratio between the minor and major axes of the ellipse as illustrated in Fig. 1.2(a) and 1.2(b), while $\mathbf{x}$ and $\mathbf{y}$ refer to the unit vectors in Cartesian coordinate system. The polarization ellipse represents the trajectory of the tip of the electric field vector as time goes by. We note that for the azimuth angle, ψ and $\psi + \pi$ states represent an identical polarization ellipse, hence an identical polarization state and the sign of χ tells about the rotation direction of the real electric field in the transverse plane (x, y), as illustrated in Fig. 1.2(a) and 1.2(b). We use the convention where we label the polarization state as left-handed (right-handed) when the tip of the electric field vector describes an ellipse that rotates counterclockwise (clockwise) when observer looks at the source, i.e., $0 < \chi \le \pi/4$ and $-\pi/4 \le \chi < 0$, respectively, see Fig. 1.2(a) and 1.2(b). Such a convention adopted to define the polarization state handedness is better appreciated when looking at the spatial trajectory defined by the tip of the real electric field at a given time. This is illustrated in Fig. 1.3 for the particular case of the two circular polarization states. Indeed, one gets left/right helical trajectories for $\chi = \pm\pi/4$, respectively.

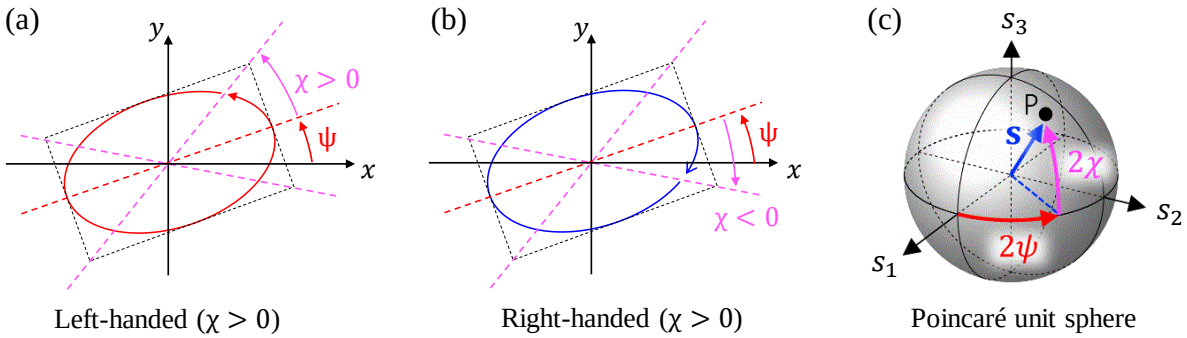

Figure 1.2 (a) Left- ($\chi > 0$) and (b) right- ($\chi < 0$) handed polarization ellipses. (c) Geometric representation of an arbitrary polarization state described by ψ and χ angles on the so-called Poincaré unit sphere where the axes are the reduced Stokes parameters (s_1, s_2, s_3).

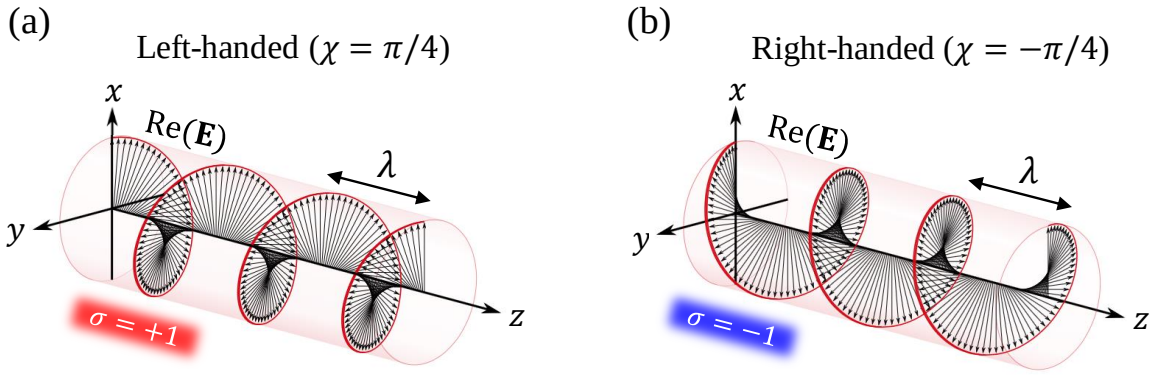

Figure 1.3 Illustration of the electric field (black arrows) tip's trajectory (red curves) at a given time for (a) left- and (b) right-handed circularly polarized light, also identified by the helicity parameter $\sigma = \pm 1$, along the propagation axis z. The helical pitch of the trajectory equals the wavelength λ.

A useful representation of the polarization state is given by the Stokes vector $\mathbf{S} = (S_0, S_1, S_2, S_3)$ defined from the (E_x, E_y) components of the complex electric field [3],

$$S_0 = |E_x|^2 + |E_y|^2 , \tag{1.3}$$
$$S_1 = |E_x|^2 - |E_y|^2 , \tag{1.4}$$
$$S_2 = 2\mathrm{Re}(E_x^* E_y) , \tag{1.5}$$
$$S_3 = 2\mathrm{Im}(E_x^* E_y) . \tag{1.6}$$

Indeed, such a vector is experimentally accessible by doing polarization projections onto six polarization states, namely

$$S_0 = I_H + I_V = I_D + I_A = I_L + I_R , \tag{1.7}$$
$$S_1 = I_H - I_V , \tag{1.8}$$
$$S_2 = I_D - I_A , \tag{1.9}$$
$$S_3 = I_L - I_R , \tag{1.10}$$

where I_H, I_V, I_D, I_A are the measured intensities of the field after a linear polarizer orientated at 0°, 90°, 45°, −45° with respect to the x axis, respectively. In addition, I_L and I_R are the measured intensities after left- and right-handed circular polarizers, which consist of a quarter-waveplate (QWP) followed by a linear polarizer.

A geometric representation of polarization states is introduced by Poincaré using reduced Stokes vector $\mathbf{s} = (S_1, S_2, S_3)/S_0$. According to this representation, any polarization state (assuming fully polarized fields) can be associated to a point on the surface of a unit sphere called Poincaré sphere in the (s_1, s_2, s_3) frame [4–6] as illustrated in

Polarization state	$\mathbf{e}$	Jones vector
Linear at angle ψ from x	$\cos\psi\,\mathbf{e}_x + \sin\psi\,\mathbf{e}_y$	$\begin{pmatrix}\cos\psi\\ \sin\psi\end{pmatrix}$
Horizontal	$\mathbf{e}_x$	$\begin{pmatrix}1\\ 0\end{pmatrix}$
Vertical	$\mathbf{e}_y$	$\begin{pmatrix}0\\ 1\end{pmatrix}$
Diagonal	$\frac{\mathbf{e}_x+\mathbf{e}_y}{\sqrt{2}}$	$\frac{1}{\sqrt{2}}\begin{pmatrix}1\\ 1\end{pmatrix}$
Antidiagonal	$\frac{\mathbf{e}_x-\mathbf{e}_y}{\sqrt{2}}$	$\frac{1}{\sqrt{2}}\begin{pmatrix}1\\ -1\end{pmatrix}$
Left-handed circular	$\mathbf{e}_+ = \frac{\mathbf{e}_x+i\,\mathbf{e}_y}{\sqrt{2}}$	$\frac{1}{\sqrt{2}}\begin{pmatrix}1\\ i\end{pmatrix}$
Right-handed circular	$\mathbf{e}_- = \frac{\mathbf{e}_x-i\,\mathbf{e}_y}{\sqrt{2}}$	$\frac{1}{\sqrt{2}}\begin{pmatrix}1\\ -i\end{pmatrix}$
Elliptical with major axis along x	$\cos\chi\,\mathbf{e}_x + i\sin\chi\,\mathbf{e}_y$	$\begin{pmatrix}\cos\chi\\ i\sin\chi\end{pmatrix}$

Table 1.1 Representation of a selection of polarization states of light.

Fig. 1.2(c). The polarization state coordinates on the Poincaré sphere are defined as follows

$$\begin{aligned} s_1 &= \cos 2\psi \cos 2\chi, \\ s_2 &= \sin 2\psi \cos 2\chi, \\ s_3 &= \sin 2\chi. \end{aligned} \tag{1.11}$$

On the Poincaré sphere the equatorial line ($\chi = 0$) represents linearly polarized light with all possible values for the azimuth angle. Indeed, $\psi = 0$ corresponds to horizontal (H), $\psi = \pi/4$ diagonal (D), $\psi = \pi/2$ vertical (V), and $\psi = -\pi/4$ antidiagonal (A) polarization states. The "north" and "south" poles, where $\chi = \pm 45°$, represent left-handed (L) and right-handed (R) circular polarization states respectively, and all the other points represent elliptical polarization states.

A convenient alternative way to present the polarization state is the so-called Jones representation, which introduces unit vectors to describe the polarization state. Typical examples are summarized in Table 1.1 where the column notation refers to $(\mathbf{x}, \mathbf{y})$ basis.

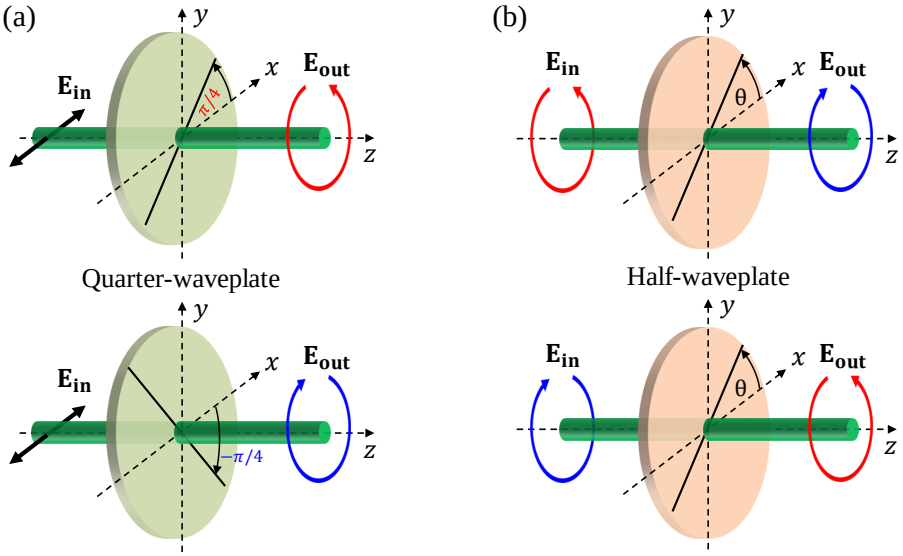

Figure 1.4 (a) Quarter-waveplate converting a linear polarization state into left-handed (top) and right-handed (bottom) circular polarization states when the slow axis is oriented at $\pm\pi/4$ with respect to the linear polarization state, accordingly. (b) Half-waveplate converting a circular polarization state from a given handedness to the opposite one. Top: from left- to right-, bottom: from right- to left-handed circular polarization states. Left/right-handed circular polarization states are indicated by red/blue arrows showing the direction of the electric field tip's trajectory at a given position in the transverse (x, y) plane.

The interest of the Jones representation appears in particular when describing polarization state changes as light interacts with an optical system. For instance, considering usual optical elements used in experiments, such as a linear polarizer, a half-waveplate (HWP), or a QWP, one can introduce a so-called Jones matrix. This is a 2×2 matrix that represents the effect of an optical element on the polarization state of an incident light beam. When the Jones matrix $\hat{\mathbf{M}}$ is applied to an input Jones vector $\mathbf{J}_{\text{in}}$, it gives the Jones vector of the output field, $\mathbf{J}_{\text{out}}$, as

$$\mathbf{J}_{\text{out}} = \hat{\mathbf{M}}\mathbf{J}_{\text{in}} \,. \tag{1.12}$$

If an optical system consists of N optical elements placed in series with Jones matrices $\hat{\mathbf{M}}_i$ and where the ith optical element is the ith to be traversed by light, the total Jones matrix of the whole system is

$$\hat{\mathbf{M}}_{\text{tot}} = \hat{\mathbf{M}}_{\text{N}}\hat{\mathbf{M}}_{\text{N}-1}...\hat{\mathbf{M}}_1 \,. \tag{1.13}$$

Some examples of Jones matrices are presented in Table 1.2, and the polarization state transformations are illustrated in a simple manner in Fig. 1.4 when light passes through a QWP and a HWP.

x-polarizer	y-polarizer	Half-waveplate	Quarter-waveplate	Anisotropic slab
$\begin{pmatrix} 1 & 0 \\ 0 & 0 \end{pmatrix}$	$\begin{pmatrix} 0 & 0 \\ 0 & 1 \end{pmatrix}$	$\begin{pmatrix} 1 & 0 \\ 0 & -1 \end{pmatrix}$	$\begin{pmatrix} 1 & 0 \\ 0 & i \end{pmatrix}$	$\begin{pmatrix} e^{\Phi_{\text{slow}}} & 0 \\ 0 & e^{\Phi_{\text{fast}}} \end{pmatrix}$

Table 1.2 The most common Jones matrices. The slow axis is oriented along the x axis in the case of optical retarders. $\Phi_{\text{slow,fast}}$ are the phase delays along the slow and fast axis of the retarder, respectively. The half- and quarter-waveplate cases are particular situations of the anisotropic slab where $\Phi_{\text{slow}} - \Phi_{\text{fast}} = \pi$ and $\Phi_{\text{slow}} - \Phi_{\text{fast}} = \pi/2$, respectively.

From this, it is useful for what follows to establish the expression of the Jones matrix of an arbitrary waveplate. Let us consider a slab of an anisotropic uniaxial medium with thickness L and slow axis orientation given by the angle Ψ counted trigonometrically from the x axis, see Fig. 1.5, and an incident polarization state given by the Jones vector $\mathbf{e}_{\text{in}}$. As the corresponding light field passes through the anisotropic slab, whose input facet is located at $z = 0$ plane, the output polarization state at $z = L$ in the (x, y) frame is expressed as

$$\mathbf{e}_{\text{out}} = \hat{\mathbf{R}}_z(\Psi) \begin{pmatrix} e^{ik_0 n_\parallel L} & 0 \\ 0 & e^{ik_0 n_\perp L} \end{pmatrix} \hat{\mathbf{R}}_z(-\Psi) \mathbf{e}_{\text{in}} \tag{1.14}$$

where $\hat{\mathbf{R}}_z(\Psi)$ is a 2D rotation matrix that operates when the (x, y) frame is rotated by Ψ around z axis,

$$\hat{\mathbf{R}}_z(\Psi) \begin{pmatrix} \cos\Psi & -\sin\Psi \\ \sin\Psi & \cos\Psi \end{pmatrix} \tag{1.15}$$

and $n_{\parallel,\perp}$ are the refractive indices experienced by linearly polarized light oriented along a direction parallel and perpendicular to the slow axis of the slab, respectively.

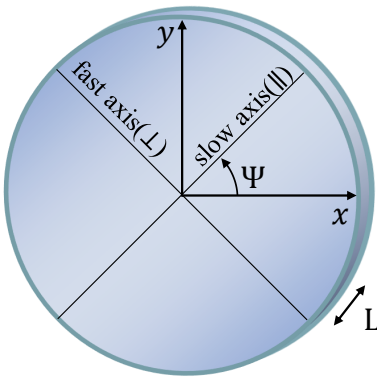

Figure 1.5 Uniaxial slab of thickness L in (x, y) frame, whose slow axis is oriented at an angle Ψ with respect to the x axis.

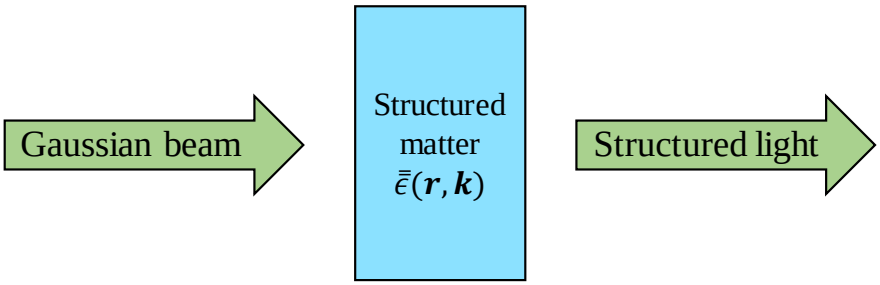

Figure 1.6 Simplistic scheme describing the position of the present manuscript, which deals with light shaping owing to the use of anisotropic structured optical element, depicted as a dielectric tensor $\bar{\bar{\epsilon}}$, placed in the course of Gaussian beam.

Now that we have briefly overviewed the main properties of the beam that we aim at structuring throughout this thesis using structured anisotropic optical materials, whose dielectric properties depend on space ($\mathbf{r}$) and incident beam wavevector ($\mathbf{k}$), see Fig. 1.6, we will present some of the main aspects of structured light field on which relies our work.

1.2 Scalar structured light

The description of an arbitrary paraxial light field with a given polarization state can be made exactly owing to the analytical solution of the paraxial scalar Helmholtz equation, which is expressed, after having defined the field as $\mathbf{E}(x,y,z,t) = u(x,y,z,)\exp i(k_0 z - \omega t)\mathbf{e}$, as

$$\frac{\partial^2 u}{\partial x^2} + \frac{\partial^2 u}{\partial y^2} + 2ik\frac{\partial u}{\partial z} = 0. \tag{1.16}$$

The general solution of this equation can be expanded into series of orthogonal functions, optical modes, each of them propagating independently without topological structural changes. There are many kinds of infinite dimensional complete orthogonal basis that are exact solutions of paraxial Helmholtz equation, such as Hermite-Gaussian (HG), Laguerre-Gaussian (LG), and Ince-Gaussian (IG) in Cartesian, cylindrical and elliptical coordinate system, respectively [7]. In this thesis, we mainly focus on LG beams, which we describe in the next section.

1.2.1 Laguerre-Gaussian beams

Fully polarized Laguerre-Gaussian modes propagating along the z axis towards $z > 0$, are uniquely characterized by two indices $l \in \mathbb{Z}$ and $p \in \mathbb{N}$, which are respectively associated with azimuthal and radial features. Namely, the corresponding complex electric field of mode (l, p) with power $\mathcal{P}$ in the cylindrical coordinate system (r, ϕ, z) is expressed as $\mathbf{E}_{l,p} = E_{l,p}\mathbf{e}$ with

$$E_{l,p}(r,\phi,z) = \sqrt{\frac{p!}{(p+|l|)!}\frac{2\mathcal{P}}{\pi\epsilon_0 c}}\frac{1}{w(z)}\left[\frac{r\sqrt{2}}{w(z)}\right]^{|l|} L_p^{|l|}\left(\frac{2r^2}{w(z)^2}\right)\exp\left[i(k_0 z - \omega t)\right] \times \exp\left[-\frac{r^2}{w(z)^2}\right]\exp\left\{i\left[\frac{k_0 r^2}{2R(z)} + l\phi - (2p+|l|+1)G(z)\right]\right\}, \tag{1.17}$$

where $L_p^{|l|}(x) = \sum_{m=0}^{p} \frac{(|l|+p)!}{(|l|+m)!(p-m)!m!}(-x)^m$ with $x = 2r^2/w(z)^2$ is the generalized Laguerre polynomial, $w(z)$, $R(z)$ and $G(z)$ are the underlying Gaussian waist radius, radius of curvature and Gouy phase, respectively. As one can check, the mode $(l, p) = (0, 0)$ is the fundamental Gaussian beam as Eq. (1.17) reduces to Eq. (1.1). The transverse intensity profiles of LG modes are axisymmetric, with the radial index p determining the number of rings, and the azimuthal index l defining the number of intertwined helical wavefronts. Typical transverse intensity and phase profiles of a few LG beams are illustrated in Fig. 1.7.

An arbitrary field $\mathbf{E} = E\mathbf{e}$ is thus described by a specific coherent superposition of modes according to

$$E(r,\phi,z) = \sum_{l,p} c_{l,p} E_{l,p}(r,\phi,z;w_0)\,, \tag{1.18}$$

where $c_{l,p}$ are complex weighting coefficients. In Eq. (1.18) we deliberately highlighted the dependence on the scaling spatial parameter w_0, which implies that there is an infinite set of superpositions for a given field since w_0 can be arbitrarily chosen. Moreover, $c_{l,p}$ have a clear physical meaning on experimental grounds. Indeed, the total power carried by the field E is

$$\mathcal{P} = \frac{1}{2}\epsilon_0 c \iint EE^* r dr d\phi = \sum_{l,p} |c_{l,p}|^2 \mathcal{P}. \tag{1.19}$$

Therefore, $|c_{l,p}|^2$ corresponds to the power fraction of the mode (l, p) that constitutes the total field.

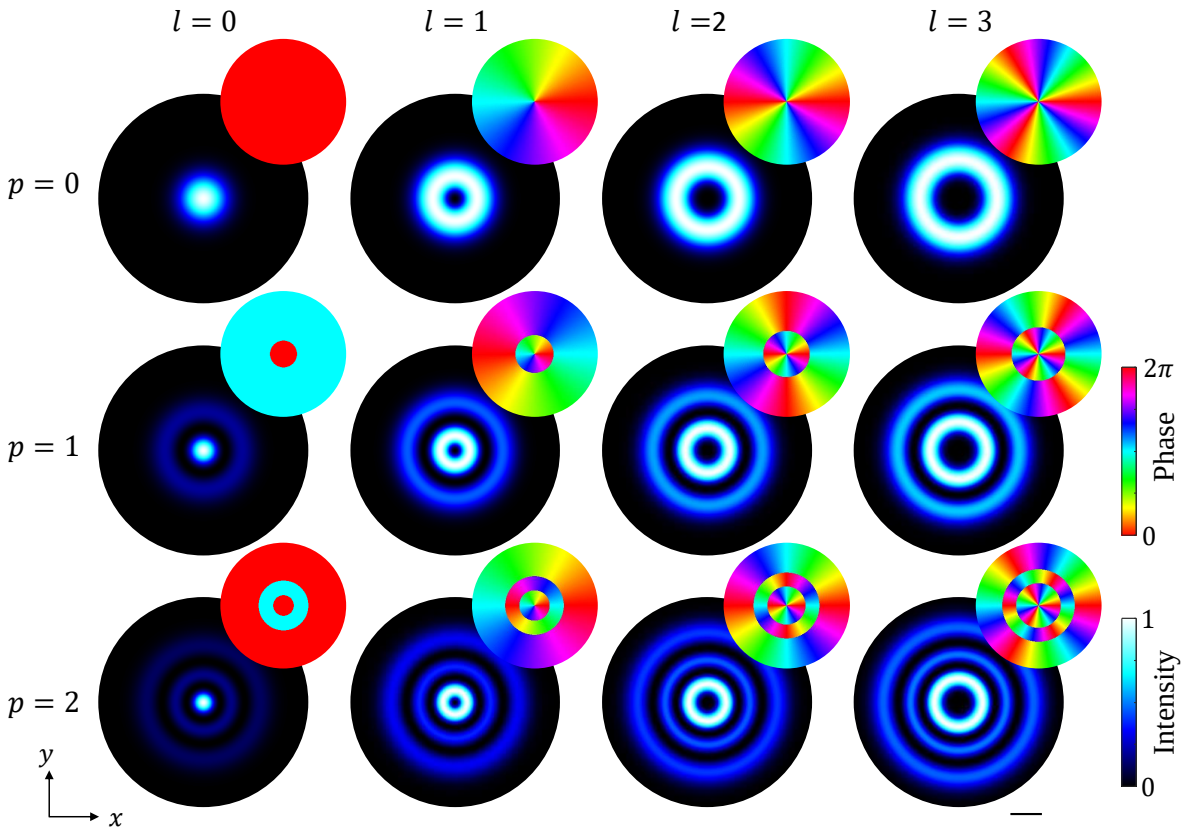

Figure 1.7 Typical intensity and phase (inset) transverse profiles of a few LG modes characterized by l and p indices, at $z = 0$. The scale bar is w_0.

1.3 Vectorial structured light

Following the discussion on scalar LG beams, this section introduces vector beams, which can be formed by the orthogonal superposition of scalar LG beams with orthogonal polarization states. We can illustrate it by restricting to LG beam of fundamental radial order, as

$$\mathbf{E}(\mathbf{r}) = E_{l_1,0}(\mathbf{r})\mathbf{e}_1 + E_{l_2,0}(\mathbf{r})\mathbf{e}_2 \tag{1.20}$$

where $l_1 \neq l_2$ and $\mathbf{e}_1 \cdot \mathbf{e}_2^* = 0$ indicate the orthogonality of the modes and polarization states, respectively.

When $l_1 + l_2 = 0$, such a superposition results in an inhomogeneous distribution of linear polarization states described by $\chi = 0$ and $\psi = \psi(\phi)$, see Fig. 1.8(b). The distinction between scalar and vector beams in terms of polarization state content is highlighted when performing polarization projections [8]. Indeed, since scalar beams exhibit homogeneous polarization distribution (see Fig. 1.8(a)), the intensity distribution profile remains unchanged regardless of the polarization projection, up to a multiplica-

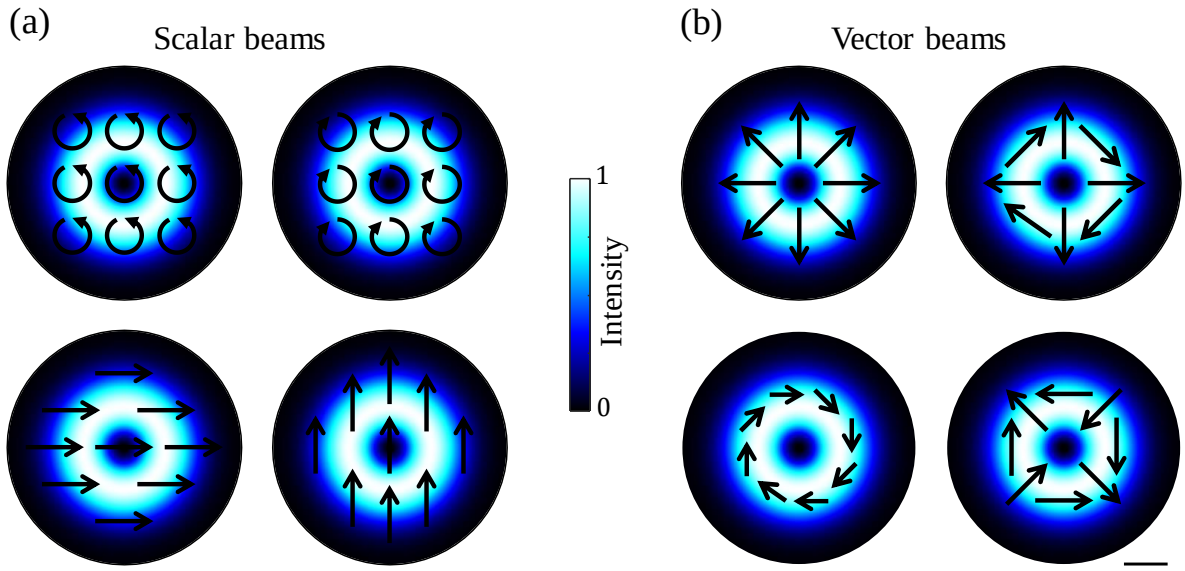

Figure 1.8 (a) Scalar and (b) vector beams. Scalar beams exhibit a homogeneous polarization distribution, shown here with left/right-handed circular and horizontal/vertical linear polarization states. Vector beams exhibit an inhomogeneous polarization distribution, shown here with linear polarization states. The scale bar is w_0.

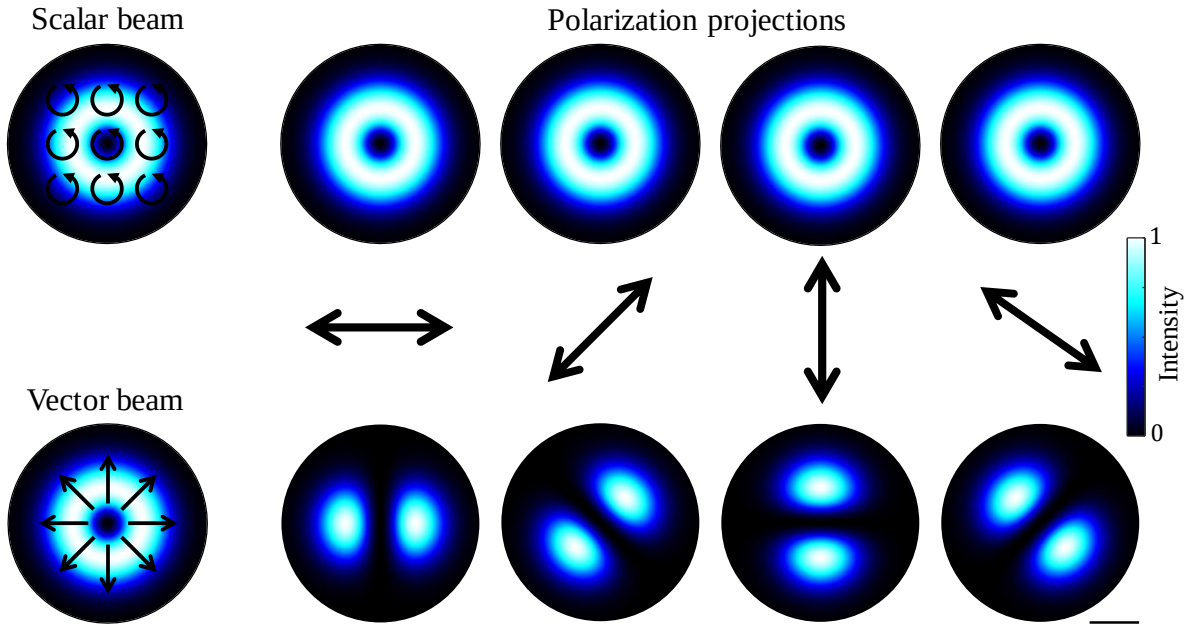

Figure 1.9 Top: the intensity distribution across the beam is unaffected regardless of the polarization projection for scalar beams, except for a possible change in magnitude. Bottom: The intensity pattern changes with the choice of polarization projection in vector beams. The scale bar is w_0.

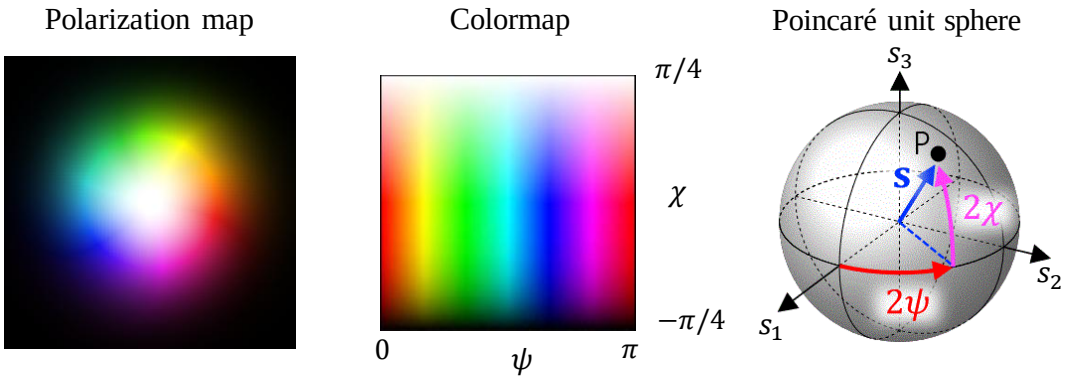

Figure 1.10 Representation of a vector beam (left) that contains all polarization states and corresponding colormap (middle), where the polarization state is defined by colorful coding according to its ψ and χ values. The Poincaré sphere is shown on the right side, on which the corresponding polarization state can be represented.

tive change in amplitude. In contrast, the intensity pattern in vector beams changes according to the chosen polarization projection as illustrated in Fig. 1.9. Moreover, the inhomogeneous distribution of polarization states is not restricted to homogeneous ellipticity. Indeed, both ellipticity and azimuth can vary. This is illustrated by considering $l_1 + l_2 \neq 0$, as illustrated in Fig. 1.10, where the chosen example $(l_1, l_2) = (1, 0)$ exhibits all possible polarization states. The visual rendering of how such an inhomogeneous polarization state distribution covers the Poincaré sphere is illustrated in the colormap of Fig. 1.10, where the white/black color corresponds to left/right-handed circular polarization states, respectively, whereas linear and elliptical states are defined by colorful coding according to ψ and χ values.

1.4 Structured light shaping strategies

Over the last 30 years, numerous studies have been conducted on structured light shaping, exploiting different principles of optics. Existing techniques can be broadly categorized into two groups: the scalar approach and the vectorial approach.

The scalar approach focuses on modifying the intensity and phase of light without altering its polarization state. In contrast, the vectorial approach accounts for the vector nature of light, hence its polarization state. This is particularly important when dealing with optical systems or media that induce changes in the polarization state as in the case of optically anisotropic materials.

In the following two sections, we will describe some of the beam shaping techniques based on scalar and vectorial approaches, respectively

1.4.1 Scalar approach

Among the various optical elements used to shape laser beams, computer-generated holograms (CGHs) [9] stand out as one of the most versatile tools for light beam shaping in laboratories. These holograms, when displayed on programmable spatial light modulators (SLMs), provide access to the creation of any arbitrary light field, making them useful for precise beam control.

A particular kind of SLM consists of an array of birefringent liquid crystal (LC) pixels, each individually controlled by an applied voltage. This voltage alters the orientation of the LC molecules while preserving the slow axis orientation that is uniform over the whole device. In turn, this changes the optical path length of the light passing through the pixels [10]. By modulating the phase of an incident light field polarized along the slow axis of the LC, SLMs operate within the scalar regime of light shaping.

In addition to phase control, SLMs can also shape the amplitude of light. By encoding a diffraction grating onto the device, the amplitude in the first diffraction order can be adjusted locally by adapting the grating depth, thereby allowing for fine control over the intensity distribution [11].

While liquid crystal SLMs have extensively been used to produce arbitrary light fields, the cheaper and faster alternative is the digital micro-mirror device (DMD) [12–14]. A DMD is an amplitude-only spatial light modulator. It is composed of an array of micro-mirrors that can be controlled in a binary manner by tilting every mirror to an angle $\pm\alpha$ (typically of the order of 10 degrees) [15]. This mechanism enables the creation of binary gratings that can be rapidly switched on demand using an external digital signal, allowing for high-speed modulation [16] of not only the amplitude but

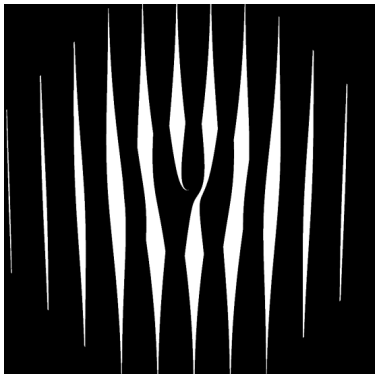

Figure 1.11 DMD binary hologram to generate LG mode with (l, p)=$(1, 0)$ from an incident Gaussian beam.

also the phase [17]. An image of a binary hologram used to produce LG mode with (l, p)=$(1, 0)$ from an incident Gaussian beam is shown in Fig. 1.11, as an example.

As already mentioned, vector beams can be generated by a superposition of orthogonal scalar fields with orthogonal polarisation states. Therefore, SLM and DMD can be used to generate vector beams, which is a common strategy in practice. The technique involves using an interferometer to superimpose two orthogonally polarized fields, which are individually shaped before being recombined. Following this approach, first reported by Neil *et al.* [18], many works have been done to generate vector beams by SLMs [19–23] or DMDs [24, 25]. Other techniques were also proposed to overcome the inefficiencies associated with diffraction [26] or to explore non-interferometric methods [27].

1.4.2 Vectorial approach: spin-orbit interaction of light

In this section, we present the vectorial approach of structured beam shaping which includes the use of spatially varying structured optical anisotropy. We will focus on vectorial beam shaping from the spin-orbit interaction of light, which refers to the coupling between the polarization state of light (spin angular momentum) and its spatial degrees of freedom (orbital angular momentum) [28]. This coupling occurs in the presence of either optical anisotropy or optical inhomogeneity (or both) of the optical element [29].

A prototypical example of an optical element that is both optically inhomogeneous and anisotropic is the so-called q-plate [30, 31]. It features a uniform birefringent phase retardation of π in the transverse plane, while the optical axis orientation varies linearly as a function of the azimuthal angle ϕ according to

$$\Psi(\phi) = q\phi + \Psi_0 \tag{1.21}$$

where q is the topological charge associated with the singularity of the material optical axis located at $r = 0$ that is usually an integer or a half-integer, and Ψ_0 is a constant. Said differently, we deal with a structured HWP.

Noting that the circular polarization basis is well suited to describe q-plates as we shall see, we consider a circularly polarized incident field. Using Jones calculus described in Sec. 1.1.2, the field transformation after the q-plate with birefringent phase retardation Δ can be expressed, up to an unimportant phase factor, as

$$\mathbf{e}_\sigma \Longrightarrow \cos\frac{\Delta}{2}\mathbf{e}_\sigma + i\sin\frac{\Delta}{2}e^{2\sigma i\Psi}\mathbf{e}_{-\sigma} \tag{1.22}$$

where $\mathbf{e}_\sigma = (\mathbf{x} + i\sigma\mathbf{y})/\sqrt{2}$ refers to the circular polarization Jones vector in the Cartesian coordinate system and $\sigma = \pm 1$ refers to the field helicity. Indeed, when $\Delta = \pi$ (as

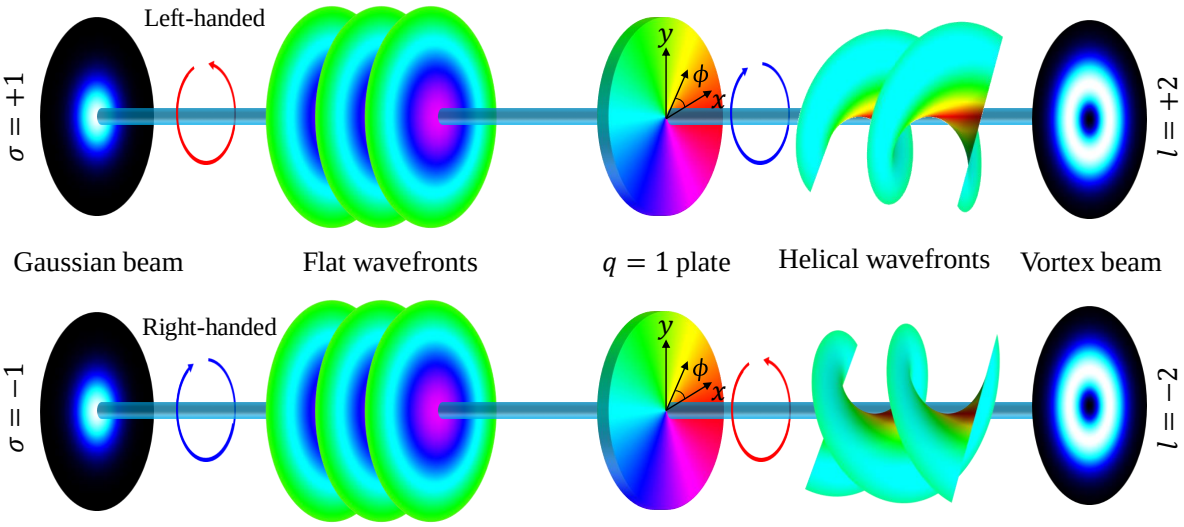

Figure 1.12 The demonstration of spin-orbit interaction of light using $q = 1$ plate. The incident left/right-handed circular polarization state ($\sigma = \pm 1$) controls the sign of the generated optical phase singularity while the polarization state is flipped.

the usual case for q-plate), the output field emerging from a q-plate can be expressed, considering $\mathbf{E}_{\text{in}} = E_{\text{in}}\mathbf{e}_{\sigma}$, as

$$\mathbf{E}_{\text{out}} = E_{\text{in}} e^{i2\sigma\Psi}\, \mathbf{e}_{-\sigma} \tag{1.23}$$

where a constant phase factor is omitted. As the previous equation suspects, a q-plate is used to generate optical vortex beams with topological charge $l = 2\sigma q$, i.e., light beams carrying on-axis optical phase singularity, whose polarization handedness is flipped (HWP behavior, see Fig. 1.4). This is illustrated in Fig. 1.12 for left- and right-handed circularly polarized incident Gaussian beam and $q = 1$ plate. Notably, the input polarization of the light controls the sign of the helicity of the output helical wavefront.

In this case, the output beam is scalar, exhibiting a homogeneous right- or left-handed circular polarization distribution. Still, a q-plate can also generate vector beams. This can be achieved by using a linearly polarized incident beam, which leads to a superposition of vortex beams with $l = \pm 2q$ topological charges, resulting in an inhomogeneous linear polarization distribution, as shown in Fig. 1.8(b). Moreover, one can achieve a vector beam containing all possible polarization states when $\Delta \neq \pi$, as illustrated in Fig. 1.10 for $\Delta = \pi/2$ case. This kind of vector beams will be presented in more detail in Chapter 3.

1.5 Outlook of the thesis

Now that we have introduced the basic concept of structured beam shaping, we can present the main objectives of this thesis that are addressed in distinct chapters, each of them focusing on specific aspects of beam shaping. The goals of the chapters are summarized hereafter, outlining the key contributions.

In Chaper 2 we introduce spin-orbit inhomogeneous and anisotropic waveplates to generate pure LG modes from an incident Gaussian beam. The generic concept based on the spin-orbit interaction of light is presented in Sec. 2.1, followed by previous experimental attempts towards modal beam shaping. Then, we introduce the design, characterization, and beam shaping capabilities of the developed structured waveplates. These waveplates with three options being obtained from nanostructured glass and two types of metasurfaces (operating in the visible and infrared domains) are presented in Sec. 2.3, Sec. 2.4, and Sec. 2.5, respectively.

In Chapter 3 we introduce compact, robust, and unitary anisotropic and inhomogeneous waveplates to generate vector beams from an incident Gaussian beam. The approach is generic and is based on the generation of superpositions of orthogonally polarized LG modes, as introduced in Sec. 1.3. With appropriate control over anisotropic and inhomogeneous features of the waveplates, we can achieve a type of vector beams that contains all possible polarization states and paves the Poincaré sphere in a specific manner, known as skyrmionic beams. This concept, along with the underlying principles is explored in Sec. 3.2 and Sec. 3.3. In Sec. 3.4 we extend the possible use of the waveplates by cascading them. The concluding insights and the overall impact of the work covered in this chapter are presented in Sec. 3.5.

In Chapter 4 we address polychromatic light beam shaping from a single optical element. We introduce a structured liquid crystal tunable optical element enable to control spectral and spatial distribution of light field in Sec. 4.1. This feature is exploited in the framework of 3D topological shaping of ultrashort optical pulses as well as on-demand control over the spatial distribution of two distinct incident wavelengths, respectively in Sec. 4.2 and Sec. 4.3.

CHAPTER 2

Spin-orbit Laguerre-Gaussian modal beam shaping

The manipulation of spatially coherent light in the spatial domain involves controlling its amplitude, phase, and polarization. Recent advances in structured light offer various technological solutions for custom tailoring light, which are already being applied in both industrial and everyday applications [32–36]. A key area of interest is the controlled generation and detection of families of orthogonal optical modes, particularly in the field of optical information, regardless of the chosen basis set [37]. Starting with a given field, the idea is to transform its amplitude and phase to satisfy the conditions required for the desired mode. Considering the usual fundamental Gaussian beam as the field to be transformed into a distinct mode, this process implies using a device that imparts the required mode-specific field changes. SLMs facilitate this transformation digitally, using pixel-based control that can be either amplitude-only [38] or phase-only [39]. In addition, by using appropriate modulation techniques, SLMs can be programmed to shape the light in both phase and amplitude [10, 11]. Notably, these scalar diffractive approaches rely on selecting one of the diffraction orders as a drop port to modulate the amplitude.

In this chapter, we are interested in another approach that consists of operating in the zeroth-order only. This is done by using the polarization channel as a complex-amplitude drop port, by exploiting the spin-orbit interaction of light, that has been introduced in Sec. 1.3. Namely, according to Eq. (1.22), a waveplate having birefringent phase retardation Δ and slow axis orientation angle Ψ in the plane transverse to the propagation axis z allows independent control of the amplitude and the phase of the output circularly polarized component that is orthogonal to the input one.

Such a spin-orbit shaping strategy was introduced in the context of LG beam shaping in 2017 [40] and applies to any kind of designed complex amplitude transverse spatial distribution. Its principle is introduced in Sec. 2.1, followed by an overview of the state of the art in Sec. 2.2. Then we present our results using different implementation

frameworks, using silica optical elements operating in the visible domain in Sec. 2.3, and dielectric metasurfaces for the visible and infrared domains in Sec. 2.4 and Sec. 2.5, respectively.

2.1 Principle

In this section, we summarize the basic knowledge related to the definition of the optical characteristics of a spin-orbit modal beam shaper operating in the circular polarization basis and aiming at producing a given Laguerre-Gaussian beam from a normally incident circularly polarized fundamental Gaussian beam [40].

We start by recalling the expression of the complex amplitude of the electric field of paraxial Laguerre-Gaussian beams of azimuthal order $l \in \mathbb{Z}$ and radial order $p \in \mathbb{N}$ in the cylindrical coordinate system (r, ϕ, z), at $z = 0$, where the beam shaping device will be placed. Namely [7]

$$E_{l,p}(r, \phi, 0; w_0) \propto \Big[\frac{r}{w_0}\Big]^{|l|} L_p^{|l|}\Big(\frac{2r^2}{w_0^2}\Big) \exp\Big[-\frac{r^2}{w_0^2}\Big] \exp\big[il\phi\big] \tag{2.1}$$

where the unimportant time oscillating factor $\exp(-i\omega t)$ is omitted.

Then we recall how the electric field of an incident circularly polarized paraxial Gaussian beam is transformed by passing through an arbitrary inhomogeneous slab of optically uniaxial medium lying in the (x, y) plane. The slab is defined as having its slow axis oriented at an angle Ψ counted from the x axis and is associated with phase delays Φ_{slow} and Φ_{fast} for linearly polarized light along the slow and fast axes, respectively. Taking a circularly polarized incident field $\mathbf{E}_{\text{in}} = E_{\text{in}}\mathbf{e}_\sigma$ and neglecting diffraction through the slab, the optical transformation is described by generalizing the situation presented in Sec. 1.1.2 and Sec. 1.4.2, to arbitrary distribution for the space-variant phase retardation and slow axis orientation, $\Delta = \Delta(r, \phi)$ and $\Psi = \Psi(r, \phi)$. This gives

$$\mathbf{E}_{\text{out}} = E_{\text{in}}\, e^{i\Phi_{\text{dyn}}(r,\phi)} \Big[\cos(\Delta(r,\phi)/2)\, \mathbf{e}_\sigma + i \sin(\Delta(r,\phi)/2)\, e^{i\Phi_{\text{geo}}(r,\phi)}\, \mathbf{e}_{-\sigma}\Big] \tag{2.2}$$

where

$$\Delta(r, \phi) = \Phi_{\text{slow}}(r, \phi) - \Phi_{\text{fast}}(r, \phi) \tag{2.3}$$

refers to the net birefringent phase delay experienced by light,

$$\Phi_{\text{dyn}}(r, \phi) = [\Phi_{\text{slow}}(r, \phi) + \Phi_{\text{fast}}(r, \phi)]/2 \tag{2.4}$$

refers to the helicity-independent *dynamic* phase, and

$$\Phi_{\text{geo}}(r,\phi) = 2\sigma\Psi(r,\phi) \tag{2.5}$$

refers to the helicity-dependent *geometric* phase. Therefore, the contra-circularly polarized ($\mathbf{e}_{-\sigma}$) output component can be used to impart an arbitrary complex amplitude modulation to an incident beam provided appropriately designed spatial distributions of $\Delta(r,\phi)$ and $\Psi(r,\phi)$.

In the framework of Laguerre-Gauss beam shaping, we aim to transform an incident fundamental Gaussian beam with waist radius w_{in}, $\mathbf{E}_{\text{in}} = E_0 \exp\left(-r^2/w_{\text{in}}^2\right)\mathbf{e}_\sigma$ at $z = 0$, into a Laguerre-Gauss beam of order (l,p). The determination of the optical characteristics of the inhomogeneous and anisotropic medium is made according to the requirement $E_{\text{out}} \propto E_{l,p}(r,\phi,0;w_{\text{out}})$. Namely,

$$E_{\text{in}}\,\sin(\Delta/2)\,e^{i(\Phi_{\text{dyn}}+\Phi_{\text{geo}})} \propto E_{l,p}(r,\phi,0;w_{\text{out}})\,, \tag{2.6}$$

which is satisfied by choosing

$$\Delta_{l,p}(r) = 2\arcsin\left\{\frac{|E_{l,p}(r,0,0;w_{\text{out}})|e^{r^2/{w_{\text{in}}}^2}}{\max[|E_{l,p}(r,0,0;w_{\text{out}})|e^{r^2/{w_{\text{in}}}^2}]}\right\} \tag{2.7}$$

provided that $w_{\text{out}} < w_{\text{in}}$, where w_{out} is the output beam waist of $E_{l,p}$ mode at $z = 0$, and

$$\Psi_{l,p}(r,\phi) = \frac{\sigma l\phi}{2} \pm \frac{\sigma}{2}\Phi_{\text{dyn}}(r) - \frac{\pi}{4}\left\{1-\text{sign}\left[L_p^{|l|}\left(\tfrac{2r^2}{{w_{\text{out}}}^2}\right)\right]\right\}. \tag{2.8}$$

2.2 State of the art

Since 2017, several implementations of spin-orbit modal beam shaping have been realized in the context of LG modes. These implementations can be categorized into two types associated with the use of bulk- or surface-structured substrates. The former one refers to attempts based on nano-structured silica glass [41,42] and the latter one to metallic [43] or dielectric [44–46] metasurfaces.

More precisely, the first experimental implementation was carried out in 2017 adopting a quasi-modal approach, which implies simplification to the original design in the limit of small birefringent phase retardation [41]. This asymptotic approach preserves the spin-controlled management of the topological charge of the generated mode at the expense of low modal conversion efficiency. Also, at that time, the laser nanostructuring technology was not able to provide small values of retardance in a controlled manner, and the obtained optical elements exhibited substantial optical scattering for operating

wavelengths in the visible domain. A few years later, in 2021, metallic metasurfaces were proposed to generate multiple LG modes, each of them being generated at different angles from the metasurface using a normally incident Gaussian beam [43]. Despite the reported advances, such metallic metasurfaces exhibited modal conversion efficiency limitations, which is a general feature of using metallic instead of dielectric metasurfaces. Also, the achieved design only operates for a given incident circular polarization state. Moreover, the reported experimental results did not assess either the modal purity or the beam propagation behavior, which left open the qualitative assessment of modal beam shaping. At the same time, another group discussed the theoretical extension of the original proposal derived in the circular polarization basis to the linear polarization basis, in the context of dielectric metasurfaces [44].

Experimental demonstration using dielectric metasurfaces came soon after [45–47] with efforts devoted to the quantitative assessment of achieved modal purity. Still, the capability to produce pure modes with both incident spin states remained a challenge when the present thesis work started. In that time, another attempt to achieve LG beam shapers from silica optical elements was reported [42] owing to the development of laser nanostructuring technology. However, the chosen design suffered limitations associated with unwanted dynamic phase modulation. This was preventing to achieve optimal modality even for the lowest l, p orders, with increasing deviations as the order l or p increases, especially the index p.

Here we are addressing all the reported limitations (mode purity, quantitative assessment, high-order azimuthal and radial modes, spin symmetry behavior) as well as discussing the role of wavelength detuning. This is done in the context of technological advances both for the silica optics approach and the dielectric metasurface approach. Specifically, the issue related to the spatially varying birefringence phase delay within the silica optics framework, which requires additional modulation of dynamic phase, is reported in Sec. 2.3 in the visible domain. Then, we address in Sec. 2.4 the spin symmetry issue that allows us to fully take advantage of the key spin-orbit feature (i.e., the fact that l can be controlled by σ) with silicon nitride metasurfaces operating in the visible domain. Finally, we extend this spin symmetric approach to the infrared domain as well as explore the production of high-order radial modes in Sec. 2.5 using silicon-based metasurfaces, which opens up opportunities for telecommunication.

2.3 Spin-orbit modal beam shaping from silica optics

This section deals with a work performed in collaboration with the group of P. Kazansky from Southampton University, UK, for the fabrication part, and with the group of A. Forbes from Wits University, South Africa, for the modal assessment part.

2.3.1 Modal plates design

As previously mentioned in all previous attempts [40, 42] of modal beam shaping from nanostructured silica glass the detrimental consequence radial modulation of the dynamic phase associated with radially varying retardance has been left unsolved. Indeed, the laser-induced modifications of the optical anisotropy are not achieved at a constant mean refractive index, as revealed in [42]. In the case of a non-constant dynamic phase, phase compensation strategy is possible by modifying Ψ profile, and the $\pm$ sign affects the way one can obtain a mode with $l = 2\sigma q$, as described by Eq. (2.8).

In this work, we choose a design with the minus sign for Eq. (2.8), for which we obtain $l = 2q$ for $\sigma = +1$ while the use of $\sigma = -1$ implies to flip the modal plate upside down with respect to the z axis in order to obtain a mode associated with $l = -2q$. Also, we present modal results by using $\sigma = +1$, restricting our experimental demonstration to the fundamental radial order $p = 0$. From Eqs. (2.7) and (2.8), this leads to the following spatial profiles for the anisotropic features of the modal plates,

$$\Delta_{l,0}(r) = 2\arcsin\left\{\left(\frac{r\sqrt{2}}{w_{\text{design}}}\right)^{|l|}\exp\left[|l|\left(\frac{1}{2}-\frac{r^2}{{w_{\text{design}}}^2}\right)\right]\right\}, \tag{2.9}$$

and

$$\Psi_{l,0}(r,\phi) = \frac{1}{2}\left[l\phi - \Phi_{\text{dyn}}(r)\right], \tag{2.10}$$

where the characteristic length w_{design} entering in Eq. (2.9) defines the incident beam waist radius maximizing the modal output power fraction up to the value $\eta_{l,0} = |l|!\, e^{|l|}/(1+|l|)^{1+|l|}$ [40]. In addition, taking care of choosing $w_{\text{in}} = w_{\text{design}}$ leads to an output waist radius for the modal beam $w_{\text{out}} = w_{\text{design}}/\sqrt{1+|l|}$ [40]. Still, as previously noted [45], the pure modal nature is not altered when $w_{\text{in}} \neq w_{\text{design}}$, at least for $p = 0$, but is associated with another waist value given by

$$w_{\text{out}} = \frac{w_{\text{design}}}{\sqrt{|l| + {w_{\text{design}}}^2/{w_{\text{in}}}^2}}. \tag{2.11}$$

Here, the first task is to experimentally determine the relationship between $\Phi_{\text{slow}} - \Phi_{\text{fast}}$ and $\Phi_{\text{slow}} + \Phi_{\text{fast}}$ in order to benchmark spatially varying dynamic phase before

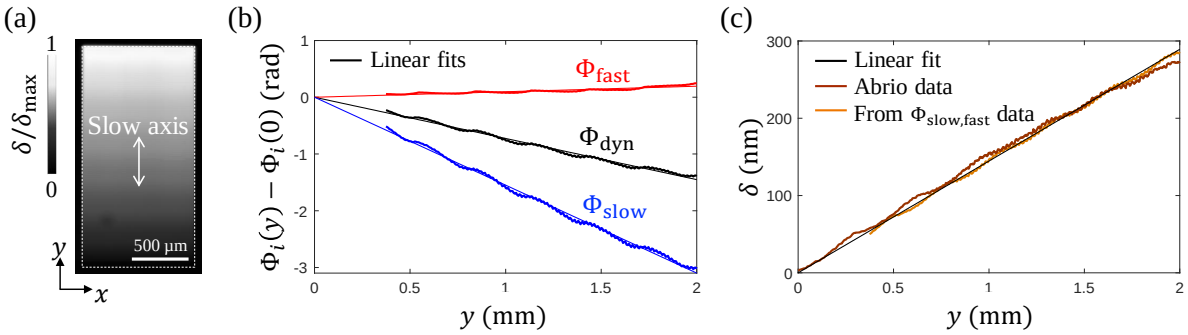

Figure 2.1 (a) Normalized anisotropic retardance of the calibration sample retrieved from Abrio imaging system. (b) Measured fast phase Φ_{fast} (red curve), slow phase Φ_{slow} (blue curve) and the associated dynamic phase $\Phi_{\text{dyn}} = (\Phi_{\text{slow}} + \Phi_{\text{fast}})/2$ (black curve) along the y direction of the sample. (c) Anisotropic retardance δ along the y direction of the sample measured from Abrio imaging system (brown curve) and from wavefront sensor phase measurements as $\delta = (\Phi_{\text{slow}} - \Phi_{\text{fast}})/k_0$ (orange curve). For all plots: lines refer to linear fit, curves refer to the mean value evaluated over the 1 mm wide side of the sample along the x direction and light color areas refer to ± standard deviation around the mean value.

addressing its compensation by design. This is ascertained from the characterization of a 1 mm × 2 mm rectangular calibration sample exhibiting a linearly varying anisotropic retardance $\delta = (\Phi_{\text{slow}} - \Phi_{\text{fast}})/k_0$ along one direction, taken as the y axis, see Fig. 2.1(a). Using a wavefront sensor operating at 550 nm wavelength (SID4-HR, Phasics) we measure the slow and fast phase retardation changes with respect to untreated silica, $\Phi_{\text{slow,fast}}(y) - \Phi_{\text{slow,fast}}(0)$, which is done by using a linearly polarized incident probe beam oriented either along the slow or the fast axis, respectively, see Fig. 2.1(b). This allows evaluating both the dynamic phase Φ_{dyn} (Fig. 2.1(b)) and the retardance δ (Fig. 2.1(c)). A complementary measurement is made using Abrio polarimetric imaging system (CRi, Inc.) operating at 546 nm wavelength, which quantitatively agrees with the phase measurements, see Fig. 2.1(c).

Using the two sets of data acquired from the analysis of the calibration sample, we experimentally demonstrate a linear relationship between the retardance and the dynamic phase with $\epsilon = 0.46$ coefficient.

$$\Phi_{\text{dyn}} \simeq -\epsilon k_0 \delta = -\epsilon \Delta \,. \tag{2.12}$$

2.3.2 Modal plates fabrication

The space-variant anisotropic optical elements were fabricated by the group of P. Kazansky using femtosecond laser structuring [48] of 3 mm thick synthetic silica glass substrates. This technology allows on-demand birefringent material modifications as a result of light-matter interaction. This is carried out with a mode-locked regeneratively ampli-

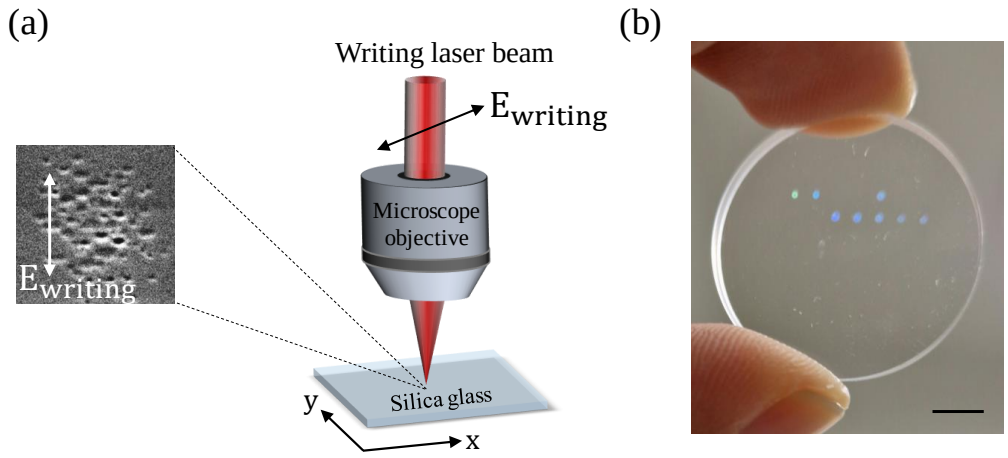

Figure 2.2 (a) Sketch of the ultrafast laser writing inside a slab of silica glass, where the double arrow refers to the orientation of the linearly polarized writing beam described by the electric field $\mathbf{E}_{\text{writing}}$. Inset: scanning electron microscope (SEM) image of nanopores made by ultrafast laser writing technology adapted from [49]. (b) Picture of the fabricated modal plates with 1mm diameter disk-shaped footprint observed in ambient illumination conditions. Scale bar: 5 mm.

fied femtosecond laser system (PHAROS, Light Conversion Ltd.), which delivers optical pulses with 600 fs duration at 1030 nm wavelength, with a repetition rate of 200 kHz. Laser pulses are focused beneath the surface of the substrate using an aspheric lens with numerical aperture $NA = 0.16$, while the substrate was fixed on a three-axis air-bearing translation stage. This enables the controlled generation of anisotropic nanopores assemblies, see Fig. 2.2(a) inset, which impart form birefringence to the initially optically isotropic medium with low scattering losses [49, 50].

All of the fabricated devices reported in the present work have been manufactured according to this approach, which provides optical elements having a damage threshold of about 1.6 J/cm^2 for a 1030 nm, 300 fs incident laser beam, which is comparable to the pristine silica glass, as reported in Ref. 51. The direction of the laser-induced slow axis is perpendicular to the polarization direction of the writing beam, which is controlled by a combination of a polarizer, a Pockels cell, and a quarter-waveplate. Moreover, the magnitude of the induced birefringence is controlled by adjusting the pulse energy from 650 nJ to 850 nJ, which allows continuous and monotonous control of the optical path difference (or anisotropic retardance) from 1 nm to 40 nm for the chosen operating wavelength $\lambda_0 = 532$ nm. The needed maximal retardance of 266 nm corresponding to $\Delta = \pi$ phase retardation was achieved by piling up several layers of laser-induced modifications. A simple schematic representation of the femtosecond laser writing technique is illustrated in Fig. 2.2(a).

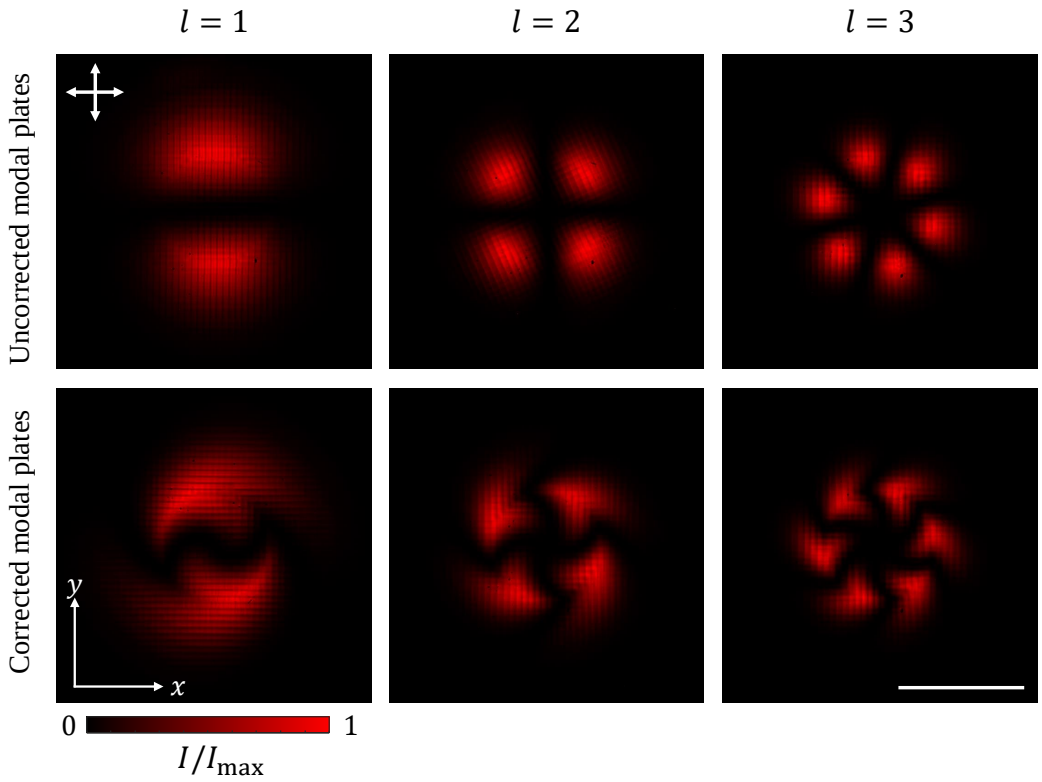

Figure 2.3 Experimental XPol images of modal plates for $l = (1, 2, 3)$ under 633 nm light illumination. Top row: uncorrected modal plates. Bottom row: Corrected modal plates. The arrowed cross refers to the linear polarizer and the analyzer. Scale bar: 400 μm

Laguerre-Gaussian modal plates with $l = (1, 2, 3)$, and 127 DPI (dots per inch) resolution were manufactured according to Eqs. (2.9) and (2.10), using $w_{\text{design}} = 250$ μm and disk-shaped structured area with diameter $2R = 1$ mm, see Fig. 2.2 (b). A second set of optical elements, not taking into account the dynamic phase correction in Eq. (2.10), have also been fabricated to quantitatively appreciate the need of taking the unwanted dynamic phase modulation into account. The two sets of three plates observed between crossed linear polarizers (XPol) and under 633 nm light illumination are shown in Fig. 2.3. The pixelation with individual 20 μm × 20 μm pixels is clearly visible from these images. The optical elements with dynamic phase correction are designated as "corrected", while the others are designated as "uncorrected".

2.3.3 Modal plate characterization

The fidelity of the fabricated optical elements with respect to the prescribed design is assessed by polarimetric imaging using the setup sketched in Fig. 2.4(a). The principle of this technique consists of determining the output Stokes parameters [52] over

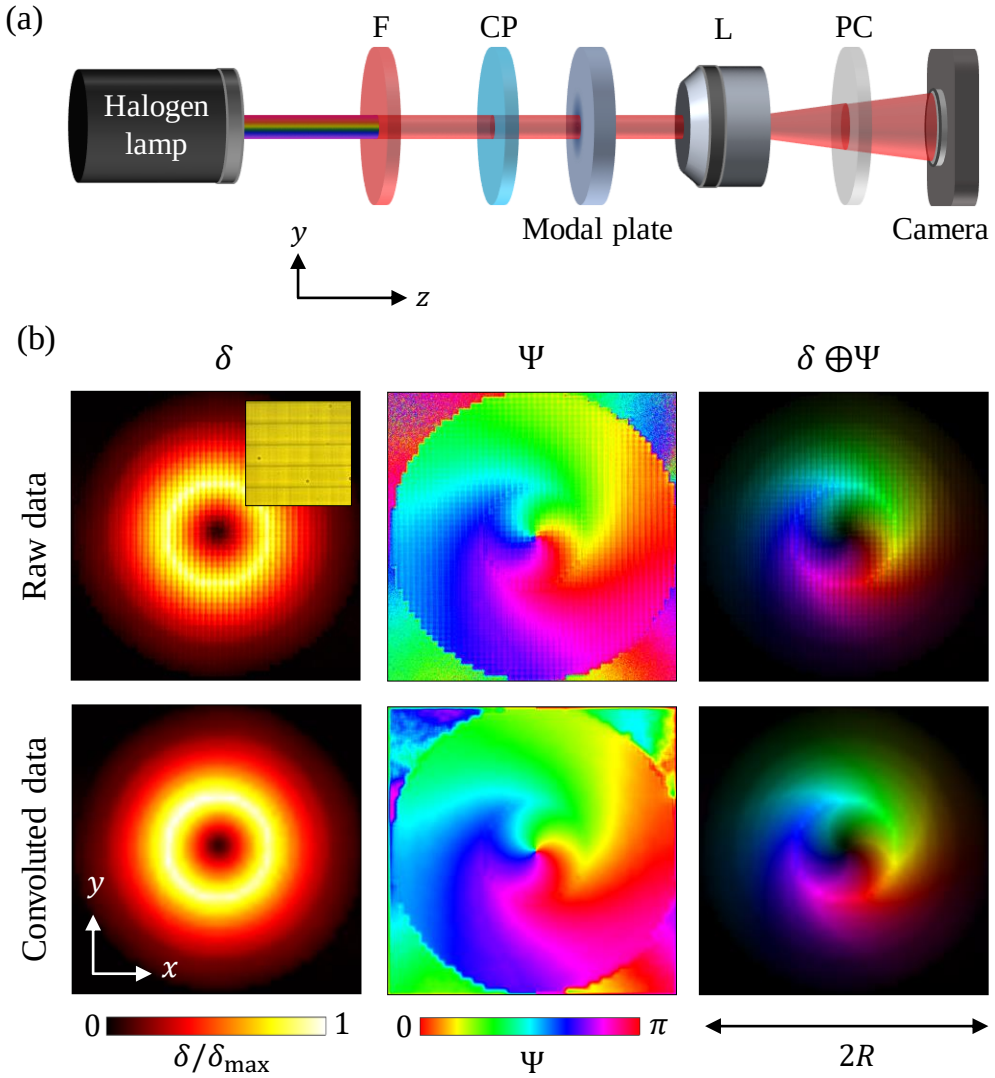

Figure 2.4 (a) Experimental setup for full Stokes polarimetric analysis of the modal plates at 633 nm wavelength. F: spectral filter for 633 nm wavelength; CP: circular polarizer; L: 4× microscope objective lens with numerical aperture NA = 0.1; PC: polarization controller allowing to record with the CCD camera the intensity distribution of the output field projected on an arbitrary polarization state. (b) Maps of the anisotropic optical features in the (x, y) plane for the corrected modal plate with $l = 1$. Left column: retardance (δ). Middle column: slow axis orientation angle (Ψ). Right column: combination of retardance and slow axis orientation (labeled as $\delta \oplus \Psi$) for which the brightness refers to $\delta/\delta_{\max}$ and the hue colormap refers to Ψ. Top row: raw data of the pixelated plate where the inset refers to the bright field image of a 5×5 pixels area, each pixel having 20 μm $\times$ 20 μm area. Bottom row: convolution smoothing of raw data over one pixel.

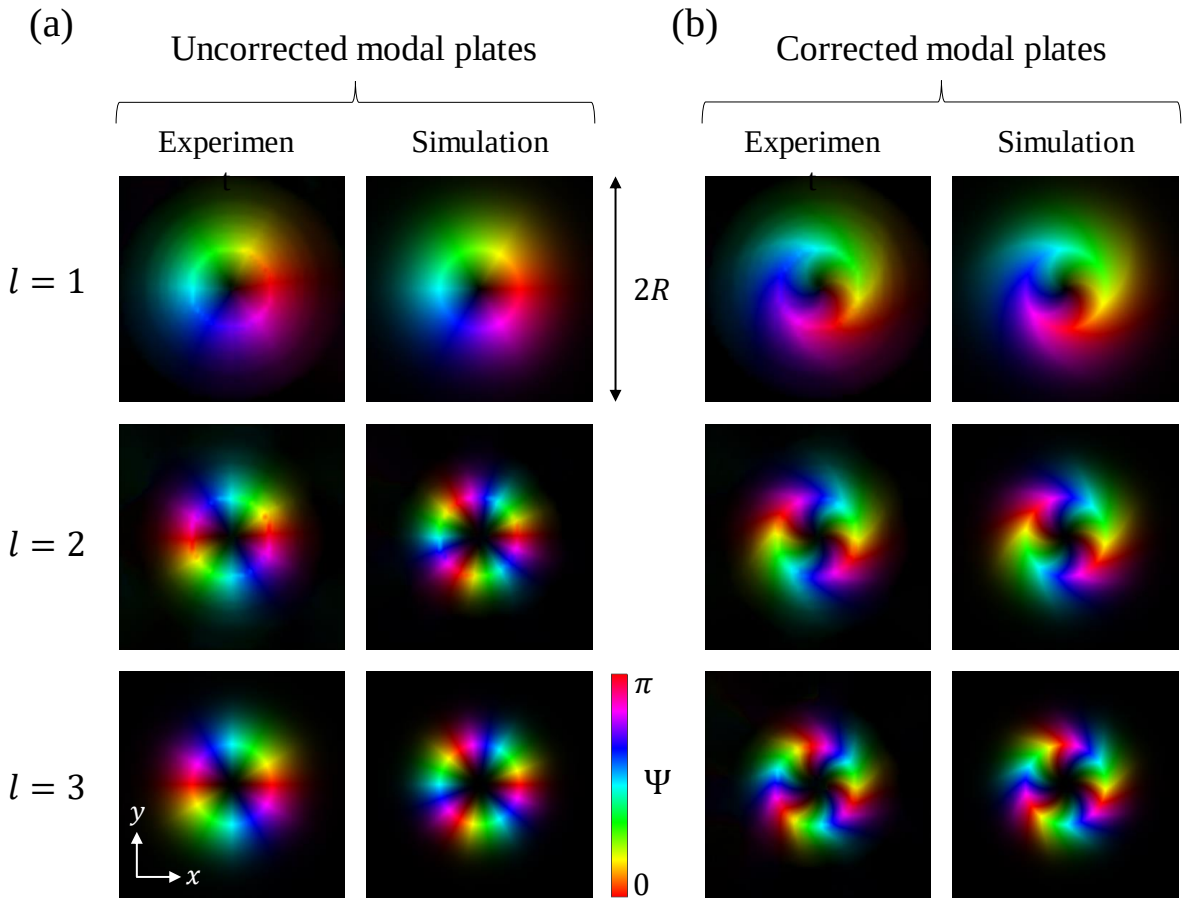

Figure 2.5 Structural maps in the (x, y) plane combining retardance (brightness) and optical axis orientation (color) for uncorrected (a) and corrected (b) modal plates with $l = (1, 2, 3)$. Left column: experimental convoluted data. Right column: simulations.

the entire surface of the optical elements. Stokes parameters measurement is done by reimaging the sample on a camera and recording six intensity images obtained from the projection of the output field $\mathbf{E}_{\text{out}}$ on H, D, V, A, L, and R polarization states, using a polarization controller (quarter-waveplate and polarizer), as presented in 1.1.2. For the Stokes polarimetry, we use $\lambda_{\text{probe}} = 633$ nm as the wavelength of the circularly polarized probe light having helicity $\sigma_{\text{probe}} = 1$. This prevents a phase wrapping ambiguity since the maximal birefringent phase delay is π at 532 nm, hence it is less at 633 nm. The retardance δ and the slow axis orientation angle Ψ are obtained from the measured reduced Stokes vector $\mathbf{s} = (s_1, s_2, s_3)$ according to

$$\delta = \frac{\lambda_{\text{probe}}}{2\pi} \arccos(\sigma_{\text{probe}} s_3) \,, \tag{2.13}$$

which implies on the assumption of negligible dispersion of the optical anisotropy, and

$$\Psi = \frac{1}{2} \arctan(s_2/s_1) - \sigma_{\text{probe}} \frac{\pi}{4} \,. \tag{2.14}$$

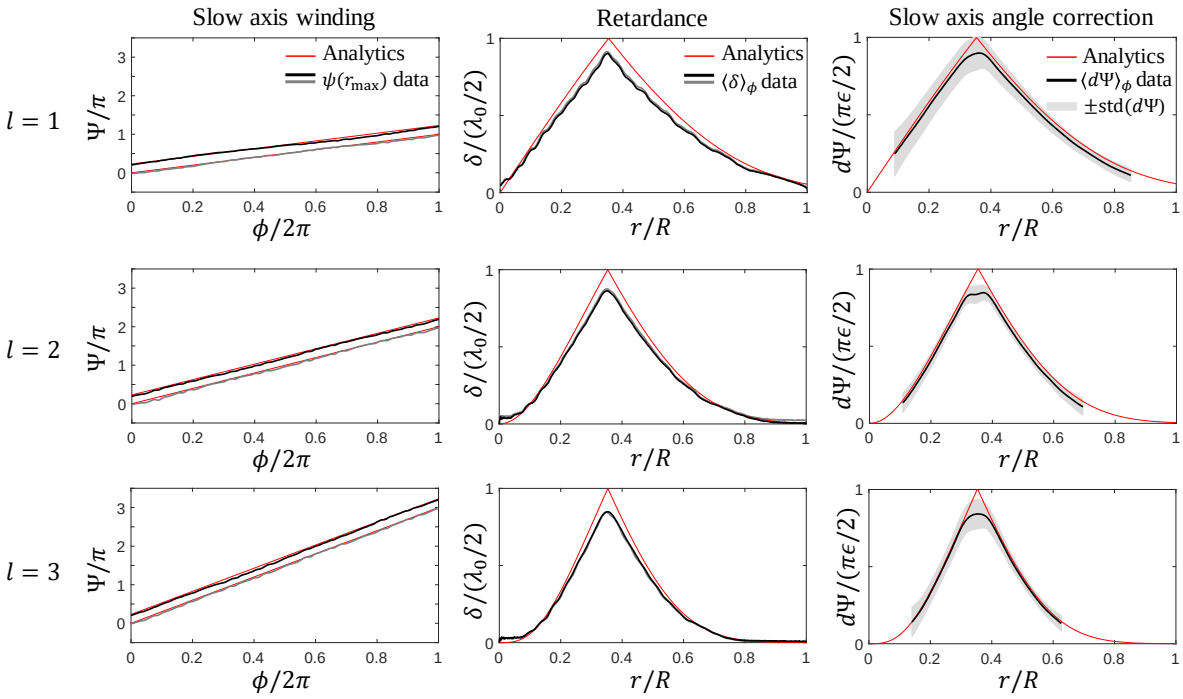

Figure 2.6 Theoretical and experimental profiles of the azimuthal dependence of the slow axis orientation angle evaluated at $r_{\max}$ defined as $\delta(r_{\max}) = \max_r[\delta(r)]$ (left column), the azimuth-averaged radial profile of the retardance $\langle\delta\rangle_\phi$ (middle column) for both uncorrected and corrected modal plates and the azimuth-averaged radial profile of the slow axis orientation angle correction $\langle d\Psi\rangle_\phi$ for the corrected modal plates (right column) for $l = (1, 2, 3)$. The retardance and slow axis orientation angle correction profiles are normalized to their maximal theoretical value $\lambda/2$ and $\pi\epsilon/2$, respectively. Thin red curves: analytics. Thick gray/black curves: experimental data from uncorrected/corrected modal plates.

The results are shown in Fig. 2.4(b) where the displayed raw data allows perceiving the pixelated nature of the optical elements, here presented for the corrected modal plate with $l = 1$, as an example. This figure also shows a smoothed version of the experimental maps that will further facilitate the visual comparison between experimental and simulated data, the latter being made using a continuous design. A summary of the polarimetric analysis for the two sets of three plates is shown in Fig. 2.5, from which we can conclude that, overall, the manufacturing protocol is satisfactory at a qualitative level. Moreover, Stokes polarimetric analysis also allows us to get a quantitative assessment of fabricated plates, which we report in Fig. 2.6. There, the experimental azimuthal profile of the slow axis orientation angle (left column) and the radial profile of the retardance (middle column) extracted from the reconstructed maps presented in Fig. 2.5 are shown and compared with the expected behavior (red curves) for both uncorrected and corrected modal plates. The radial profile of the slow axis orientation angle correction $d\Psi = \Psi - l\phi/2$ for the corrected modal plates is also shown (right column).

These results demonstrate a good level of fidelity in the laser writing technology. Still, we note an apparent difficulty in reproducing the cusp profile associated with both the retardance and the dynamic phase correction via geometric phase management. In fact this is due more to the pixelation chosen for fabrication and the azimuth-average assessment than to any inherent limitation of the laser nano-structuring process. Now that the structure of the modal plates is validated, we address their beam shaping capabilities and modal characteristics in the next sections.

2.3.4 Assessing modality: qualitative approach

A well-known characteristic pertaining to Laguerre-Gaussian modes is that their shape is unaltered, up to a spatial stretching factor, as they propagate through a linear and homogeneous medium. Indeed, as explicited analytically by Eq. (1.17), the transverse intensity profile is scaled by the z-dependent beam waist radius $w(z)$. Experimentally, this can be retrieved by recording the transverse intensity distribution as the beam propagates. The experiment is made by preparing an incident circularly polarized Gaussian laser beam with $w_{\text{in}} = w_{\text{design}}$ and imaging the contra-circularly polarized spatial intensity distribution of the beam at a distance z from the sample with 5 mm steps and choosing 1:1 imaging condition. This is realized by translating an objective lens together with a camera (in front of which is placed a circular polarizer to extract only the contra-circularly polarized component) while keeping fixed the distance between them, as is shown in Fig. 2.7(a). Then, azimuth-averaged radial intensity profiles are calculated from the recorded images, which allows reconstructing a meridional intensity cross-section.

The results are shown in Fig. 2.7(b) for $l = 1$ and three types of optical elements as we also show results obtained from a standard spin-orbit vortex plate, which refers to a q-plate design with $q = 1/2$ (see Sec. 1.4.2) that corresponds to $\Delta = \pi$ and $\Psi = \phi/2$ and has been fabricated using the same laser nano-structuring technique as the other plates. For the latter plate, we obtain the well-known ringing intensity profile [53], which is associated with the presence of a distribution of radial modes with $p \neq 0$ [54]. As expected, the invariance of the beam shape upon propagation is visually optimized for the corrected modal plate whereas the result for uncorrected modal plates highlights aspheric focusing associated with the spatial modulation of the dynamic phase.

The corresponding simulation results, illustrated in Fig. 2.7(c), are performed by using the Fourier beam propagation method, which involves a few steps. First, we

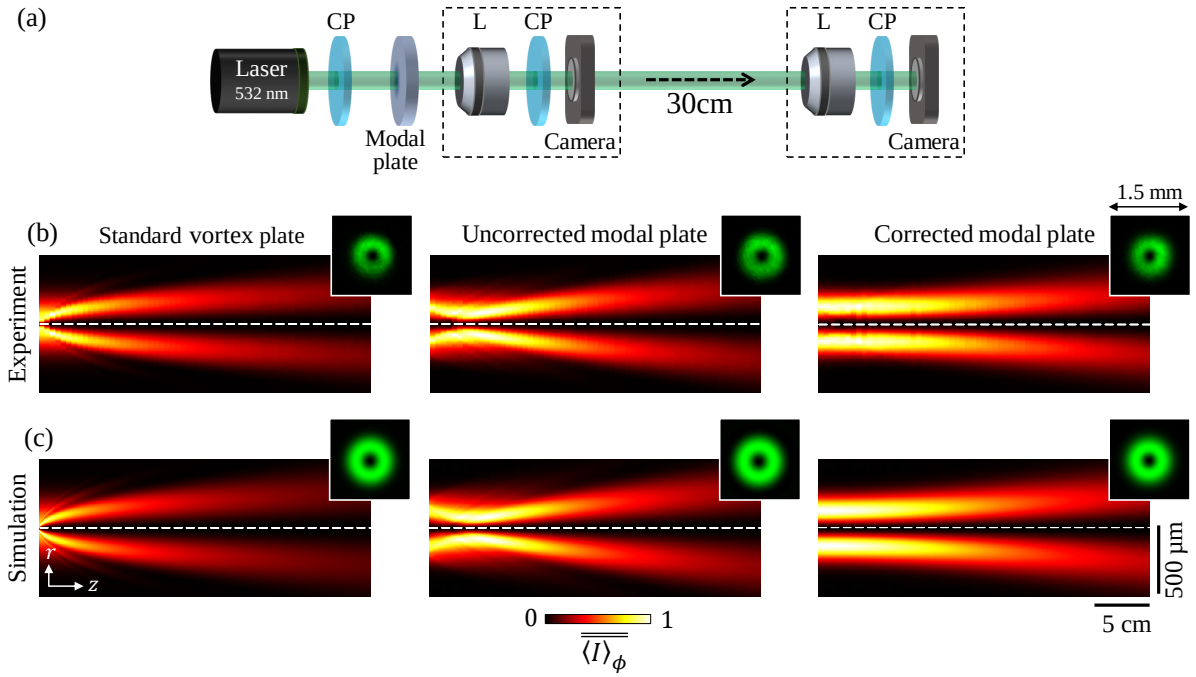

Figure 2.7 (a) The experimental setup to record the contra-circularly polarized spatial intensity distribution of the beam at a distance z from the sample up to 30 cm. CP: circular polarizer for 532 nm; L: 4× microscope objective lens with numerical aperture NA = 0.1. Experimental (b) and simulated (c) normalized azimuth-average intensity distribution in the (z, r) plane for standard vortex plate (left column), uncorrected (middle column), and corrected (right column) modal plates for $l = 1$, where $\bar{\bar{I}} = \langle I \rangle_\phi / \max_{r,z}[\langle I \rangle_\phi]$. The experimental data is recorded by moving an imaging module of "L+CP+Camera", along the z (white dashed line) axis by steps of 5 mm over a distance of 30 cm. Insets: transverse intensity distribution recorded at $z = 30$ cm. The simulation is made using the Fourier beam propagation method.

compute the Fourier transform of the field at $z = 0$, which gives the field in momentum (or spatial frequency) space. Next, we multiply the field by the propagation factor $\exp(ik_z z)$, where $k_z = \sqrt{k_0^2 - k_x^2 - k_y^2}$ with k_x and k_y being the wavevector components in the x and y directions, respectively, and z is the propagation distance. Finally, performing an inverse Fourier transform of this field yields the propagated field at distance z in real space.

More quantitatively we make use of the L_2-norm to define a mean-square distance d between two real functions $f(x)$ and $g(x)$ in the range $x \in [a, b]$ as

$$d(f, g) = \sqrt{\int_a^b [f(x) - g(x)]^2 \, dx}. \tag{2.15}$$

We thus define the dimensionless quantity

$$\varepsilon_{l,p}(z) = \sqrt{\frac{\int_0^{R_{\max}} \left[I_{\text{plate}}(r, z) - I_{E_{l,p}}(r, z) \right]^2 dr}{\int_0^{R_{\max}} I_{E_{l,p}}(r, z)^2 dr}} \tag{2.16}$$

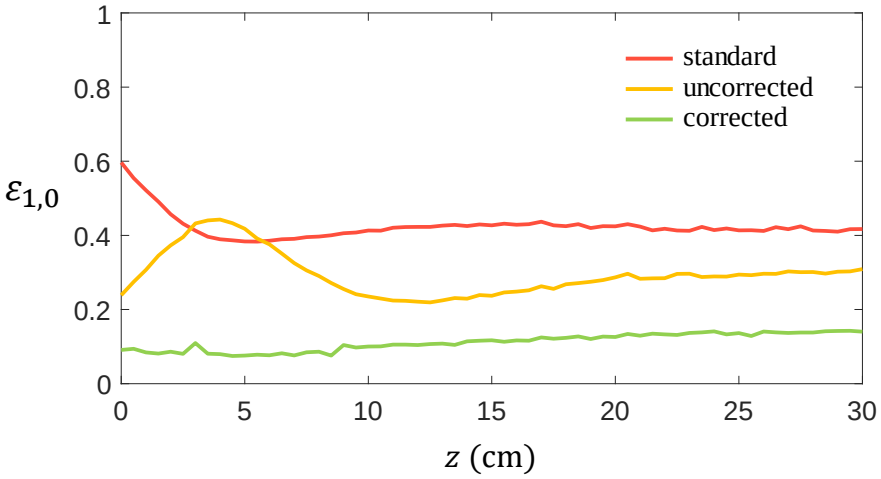

Figure 2.8 Experimental L_2-norm relative mean square distance between the measured radial intensity profiles for standard, uncorrected, and corrected vortex plates with $l = 1$ and $E_{1,0}$ mode vs the propagation distance z where $z = 0$ refers to the plane of the plate.

as an estimate of the relative overall deviation with respect to a pure LG mode with orders (l, p), where $R_{\max} = 500$ μm is the maximal distance from the z axis from which the intensity profile is measured. The results are shown in Fig. 2.8 for $(l, p) = (1, 0)$, which demonstrates that the corrected plates outperform with respect to the previous experimental realizations [41, 42].

2.3.5 Assessing modality: quantitative approach

The detailed determination of the modal performances of the fabricated silica optical elements is done by assessing the modal content of the generated field at the output of the modal plates. The approach relies on the fact that, in general, the output beam can be decomposed on a $E_{l,p}$ basis with a given transverse spatial "ruler" w_{out} according to (see Sec. 1.2.1)

$$\widetilde{E}_{\text{out}}(r, \phi, 0) = \sum_{l,p} c_{l,p} \widetilde{E}_{l,p}(r, \phi, 0; w_{\text{out}}) \,, \tag{2.17}$$

where tilde symbol refers to normalized fields that satisfy $\iint |\widetilde{E}|^2 r dr d\phi = 1$, w_{out} is the targeted Laguerre-Gauss waist radius given by Eq. (2.11) and the complex coefficients $c_{l,p}$ tell about the modal content of the field. In particular, noting that $\sum_{l,p} |c_{l,p}|^2 = 1$, we recall that $|c_{l,p}|^2$ represents the power fraction carried by the basis element with indices (l, p) as mentioned in Sec. 1.2.1.

Experimentally, we determine the modal content using a well-established modal decomposition approach based on the use of spatial light modulator [55]. Accordingly, we

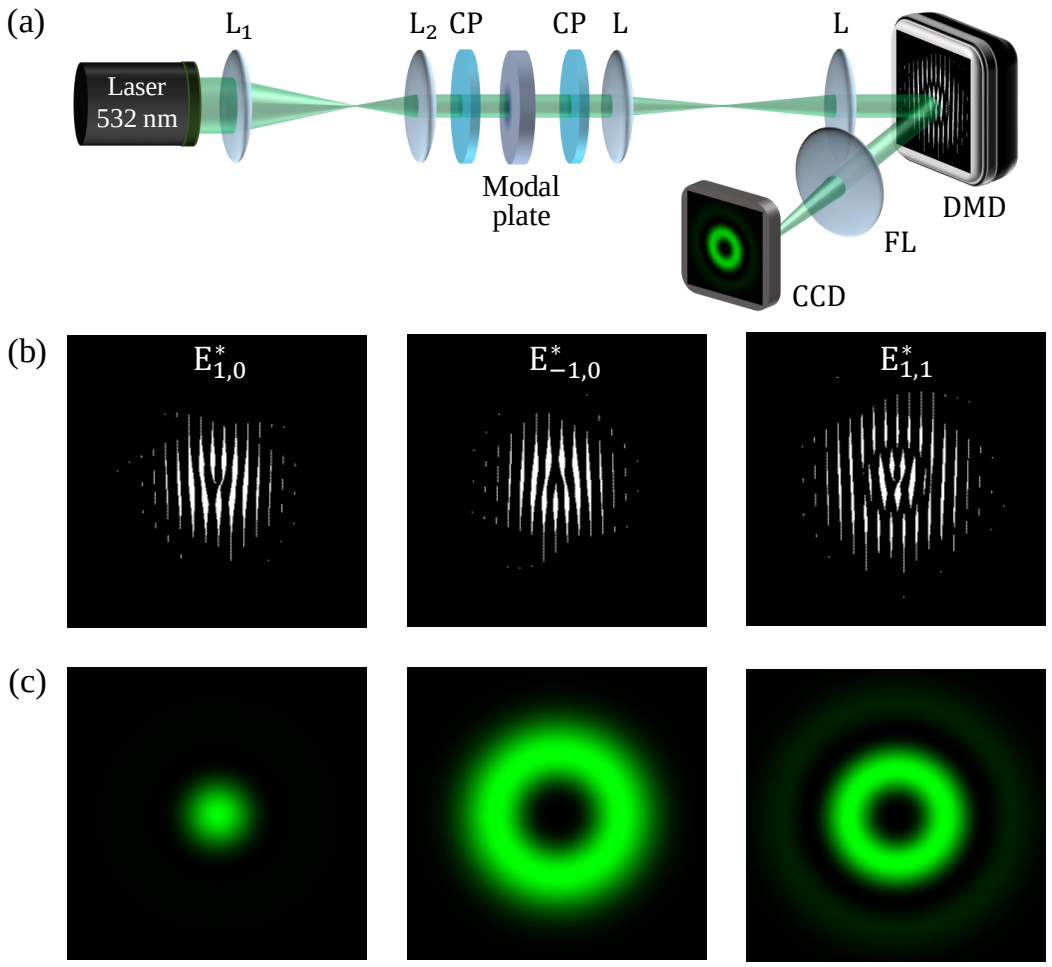

Figure 2.9 (a) Experimental arrangement used to perform modal decomposition. L_1 and L_2: pair of lenses with focal lenses 275 mm and 100 mm to reduce the beam waist radius down to 250 μm; CP: circular polarizer; L: pair of lenses with focal length 150 mm used in $4f$ configuration; DMD: digital micromirror device (1080×1920 pixels, each 7.6 μm × 7.6 μm in size); FL: Fourier lens with focal length 500 mm; CCD: intensity recording device (1288×924 pixels, each 3.75 μm × 3.75 μm in size). (b) Examples of binary amplitude masks encoded on the DMD screen. (c) Transverse intensity profiles detected on CCD for $E_{1,0}$ input beam.

use the setup depicted in Fig. 2.9(a), preparing an incident circularly polarized Gaussian laser beam with $w_{\text{in}} = w_{\text{design}}$. The output field $\widetilde{E}_{\text{out}}$ is then imaged on a DMD using a $4f$ imaging system. The DMD is encoded with a binary amplitude hologram of the form [17]

$$H(\mathbf{r}) = \frac{1}{2} + \frac{1}{2}\text{sign}\Big[\cos\big[2\pi G(\mathbf{r}) + \arg[\widetilde{E}^*_{l,p}(\mathbf{r})]\big] - \cos[\arcsin(|\widetilde{E}^*_{l,p}(\mathbf{r})|)]\Big] \tag{2.18}$$

where $G(\mathbf{r}) = g_x x + g_y y$ defines a grating with frequencies g_x and g_y in the Cartesian pixel coordinates x and y, respectively. The amplitude hologram encoded by DMD makes the field of the first diffraction order proportional to $\widetilde{E}_{\text{out}}\widetilde{E}^*_{l,p}$. Some hologram examples

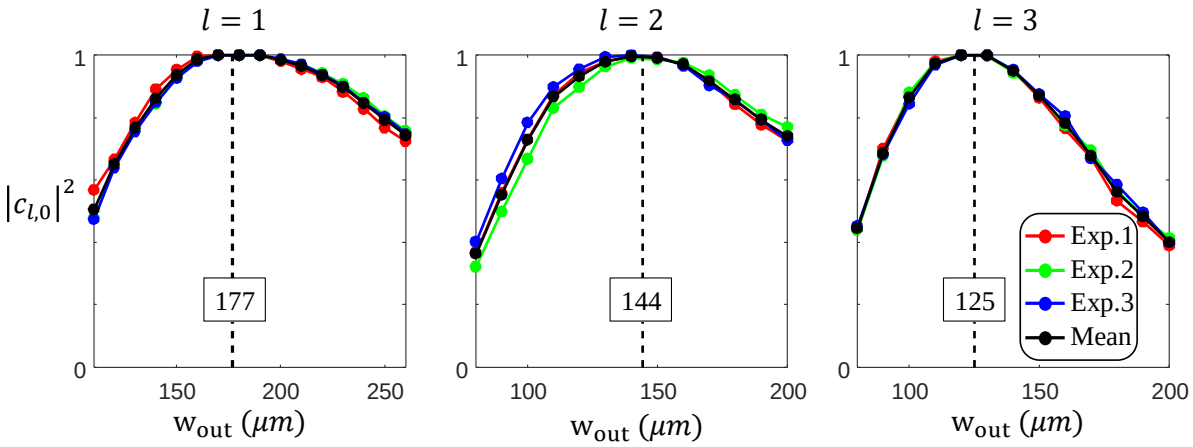

Figure 2.10 Experimentally measured modal power fractions $|c_{l,0}|^2$ of $l = (1,2,3)$ corrected modal plates to determine the optimal output beam waist for modal decomposition. The numbers in the box correspond to the theoretical output waist values in microns.

($E^*_{1,0}$, $E^*_{-1,0}$ and $E^*_{1,1}$) are shown in Fig. 2.9(b). Then we operate an optical Fourier transform for the first diffraction order by using a lens and placing the camera at the Fourier plane, where the intensity distribution reads

$$I_{\text{Fourier plane}}(\boldsymbol{\kappa}) \propto \left| \iint \widetilde{E}_{\text{out}} \widetilde{E}^*_{l,p} \exp(i\,\boldsymbol{\kappa}\cdot\mathbf{r}) r dr d\phi \right|^2, \tag{2.19}$$

where $\boldsymbol{\kappa}$ refers to the spatial frequencies wavevector in the Fourier plane. The transverse intensity profiles in the Fourier plane of $E_{1,0}$ input beam are shown in Fig. 2.9(c), which correspond to the holograms in Fig. 2.9(b). Therefore, accounting from the orthonormal nature of the LG basis $\{\widetilde{E}_{l,p}\}$, we get for the on-axis intensity in the Fourier plane

$$I_{\text{Fourier plane}}(\mathbf{0}) \propto |c_{l,p}|^2 . \tag{2.20}$$

We choose a square region of 3×3 pixels centered on-axis to evaluate $I_{\text{Fourier plane}}(\mathbf{0})$, and record the outcome via a power measurement, taking care to select the optimal output beam waist for the modal decomposition [56], that is $w_{\text{out}} = w_{\text{design}}/\sqrt{1+|l|}$ when using $w_{\text{in}} = w_{\text{design}}$, see Eq. (2.11). To validate this expression, we experimentally select multiple beam waists for decomposition and find the optimal waist value maximizing $|c_{l,0}|^2$ for $l = (1,2,3)$ corrected modal plates. For each case, three independent measurements are carried out and together with the corresponding mean values are shown in Fig. 2.10. This experimentally demonstrates that, indeed, the output beam waist maximizing a monomodal behavior equals the theoretical expected values. Further experimental analysis is therefore made according to such values.

	Standard		Uncorrected		Corrected	
	$\{0 \le p \le 5\}$	$\{0 \le p \le 200\}$	$\{0 \le p \le 5\}$	$\{0 \le p \le 200\}$	$\{0 \le p \le 5\}$	$\{0 \le p \le 200\}$
$l = 1$	95.0	93.2	93.9	93.6	100	100
$l = 2$	88.7	84.5	92.7	92.2	100	100
$l = 3$	83.6	77.5	92.3	91.6	100	100

Table 2.1 The result of simulated modal power fractions $|c_{l,0}|^2$ of standard, uncorrected and corrected plates with $l = (1, 2, 3)$ for $\{0 \le p \le 5\}$ and $\{0 \le p \le 200\}$ ranges for decomposition. For all cases $\{-10 \le l \le 10\}$.

The hologram is then iteratively refreshed to achieve all-optical projection of the output field over a range of Laguerre-Gaussian modes given $\{l, p\} = \{-5 \le l \le 5,\ 0 \le p \le 5\}$ and the measured modal powers are eventually normalized to satisfy the completeness condition $\sum_{l,p} |c_{l,p}|^2 = 1$.

To validate the selected range $\{l, p\}$ for the modal decomposition, which remains of finite dimension in practice, we evaluate the power fraction $|c_{l,0}|^2$ of the desired mode from simulations using various ranges for l and p. At first, we find that expanding the l range from $[-5, 5]$ to $[-10, 10]$ does not alter much the power fraction of the desired mode. Subsequently, we examine the impact of the p range on the decomposition. The

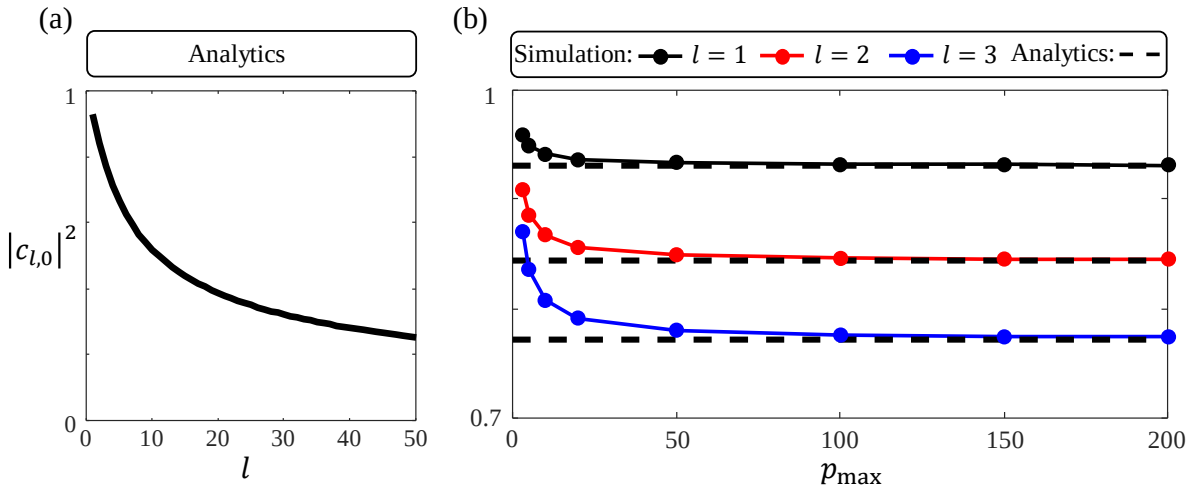

Figure 2.11 (a) Analytical modal power fraction $|c_{l,0}|^2$ as a function of l according to the Eq. (2.21) for standard plates. (b) Simulated modal power fractions of the three $l = (1, 2, 3)$ standard vortex plates as a function of p range for decomposition, $\{-10 \le l \le 10\}$. The data points correspond to p ranges p_0 value for which $\{0 \le p \le p_{\max}\}$ and solid curves are only guides for eyes. Black dashed lines indicate the analytical power fraction for each l value, see Eq. (2.21).

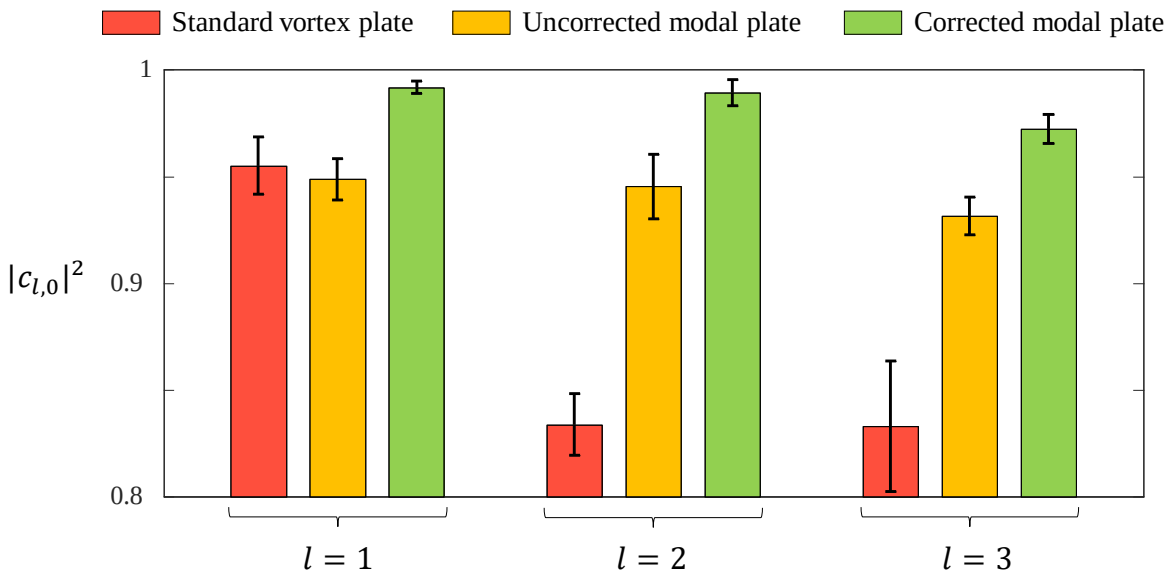

Figure 2.12 Experimentally measured modal power fractions $|c_{l,0}|^2$ of the three kinds of beam shapers studied in this work for $l = (1, 2, 3)$, using the appropriate input spin state for the corrected modal plates.

decomposition ranges of $\{0 \leq p \leq 5\}$ and $\{0 \leq p \leq 200\}$ at fixed $\{0 \leq l \leq 10\}$ are compared in Table. 2.1 for all nine plates. Our findings indicate that the power fraction of the desired mode is constant and maximal for the corrected plate, is almost unchanged for the uncorrected plate, and is close to the analytical value

$$|c_{l,0}|^2 = \frac{2^{|l|}|l|^2}{1+|l|}\left(\frac{1+|l|}{2+|l|}\right)^{2+|l|}\frac{\Gamma^2(|l|/2)}{\Gamma(1+|l|)}, \tag{2.21}$$

for the standard plate (see Fig. 2.11(a)), as the p range increases, see Fig. 2.11(b), that highlights the fact that the amount of power carried by high-order p modes increases with l. Also, note that these features are unchanged if one deals with negative values of l instead of the present situation where l is positive.

The experimental results of modal decomposition are summarized in Fig. 2.12, where the shown mean values and standard deviations refer to 6 [12] independent measurements (3 [6] for each value of $\sigma = \pm 1$) for standard [uncorrected] plates. Indeed, we recall that these designs are equally functional whatever the incident spin state provided that the contra-circular polarization state is selected for the uncorrected plates. In addition, the data refer to 6 independent measurements for $\sigma = 1$ for the corrected plates. This quantitatively ascertains the enhanced modal performances of the corrected modal plates compared to the other designs. Still, since both amplitude and phase are controlled

in the corrected case one would expect 100% purity whatever l, up to a decrease in efficiency with increasing $|l|$. However, we recall that the modal purity is ideally 100% for continuous devices only. Dealing with experiments and pixelated devices, it is not surprising that the performances do not reach that of ideal continuous patterned devices. As for the observed decrease with the order of the plate, we note that the pixelation (resolution) is fixed regardless of l in practice and that the radial profiles for Δ, hence Ψ, are steeper as $|l|$ increases. Therefore, the effect of pixelation becomes more significant for larger $|l|$, which gives a credible understanding of the observed trend.

2.3.6 Structural losses of the plates

When dealing with structured optical elements, determining the transmission coefficient (T) is important for assessing how efficiently light is transmitted through the system. This is done by calculating the ratio between the output power from the structured area (designated as P_2) and unstructured area (designated as P_1) of the sample by using a simple experimental setup depicted in Fig. 2.13(a). The transmission coefficient is measured both near the sample and at a sufficiently far distance to capture only the on-axis output power. The results of the measurements are summarized in Fig. 2.13(b) for all nine plates, providing a clear comparison of their transmission characteristics. Overall they exhibit approximately 5% structural losses.

(a)

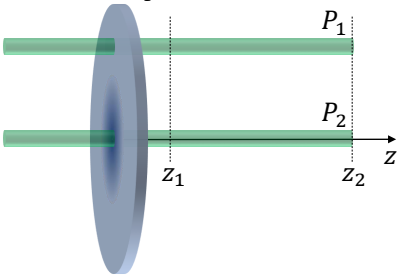

(b)

$$T = \frac{P_2}{P_1} \times 100\%$$

	Standard		Uncorrected		Corrected	
	z_1 = 10cm	z_2 = 50cm	z_1 = 10cm	z_2 = 50cm	z_1 = 10cm	z_2 = 50cm
$l = 1$	95.5	95.5	97.4	95.9	98.1	96.1
$l = 2$	94.8	93.2	98.1	96.1	98.1	96.1
$l = 3$	94.8	92.0	98.1	96.1	97.4	96.0

Figure 2.13 (a) Experimental sketch used to measure the transmission coefficient of the optical elements. The power is measured at distances of 10 cm and 50 cm from the plates, where P_1 corresponds to the output power from the unstructured area and P_2 corresponds to the output power from the structured area. (b) Summary of the transmission coefficient ($T = P_2/P_1$) for all nine plates.

2.3.7 Towards high-order modes

The full exploitation of high-dimensional bases for light in optical information and communication relies on the technological ability to design devices capable of generating high-order modes. Notably, the generation of Laguerre-Gaussian modes with high indices comes with a fabrication challenge due to the increase of spatial frequencies as l and p increase. Still, advances in nano-fabrication make it possible to achieve it from cascaded [57, 58] or single-stage [46] metasurfaces. Regarding laser nano-structured silica optics, although the generation of light beams with high orbital angular momentum (OAM) states ($l \sim 100$) has been reported [59], it remains limited to non-modal standard spin-orbit plates. Here we explore the possible extension of the modal approach to high-order Laguerre-Gaussian modes, by choosing the case study $(l, p) = (10, 0)$. Our results are shown in Fig. 2.14 both for uncorrected and corrected designs, keeping the same parameters as for the demonstration for $l = (1, 2, 3)$, namely $w_{\text{in}} = 250$ μm, $2R = 1$ mm and structured pixel size of 20 μm $\times$ 20 μm as done for low-order modes. Although the intensity distribution is qualitatively satisfactory, the present pixelated design of the modal plates and their limited size do not allow for reaching high values for the measured modal power fractions with our optical system. In addition, while the uniform design

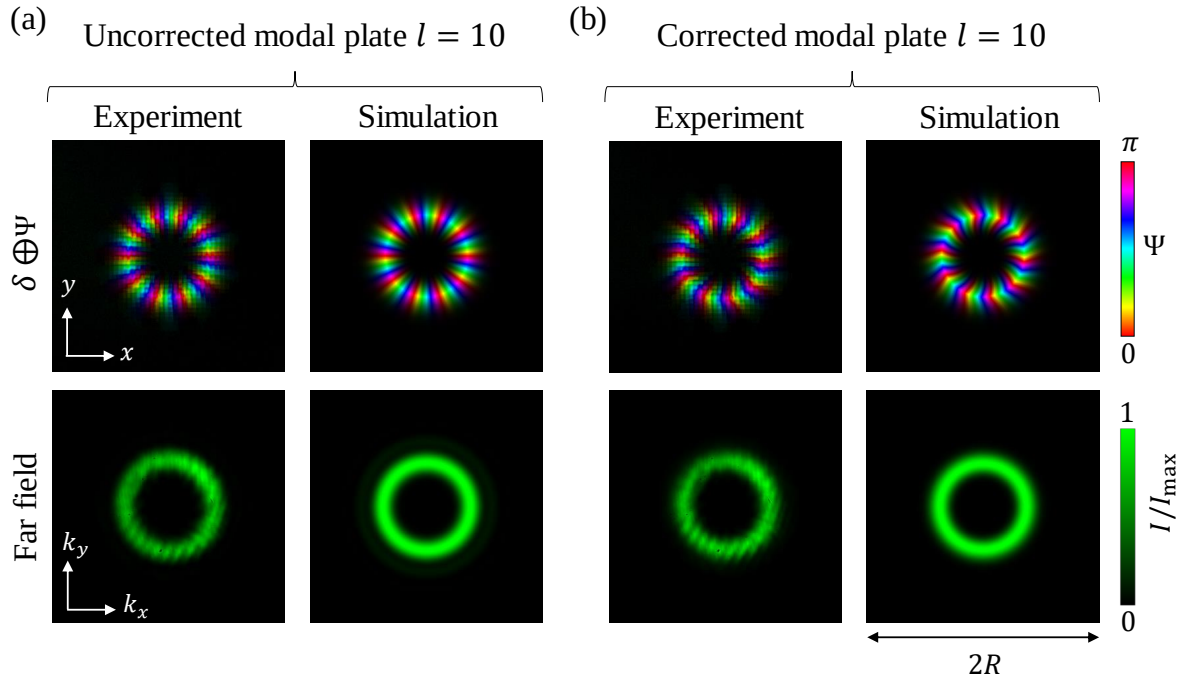

Figure 2.14 Structural maps in the (x, y) plane combining retardance (brightness) and slow axis orientation (color) and far field intensity distribution for uncorrected (a) and corrected (b) modal plates with $l = 10$. Left column: experimental data. Right column: simulation from ideal design.

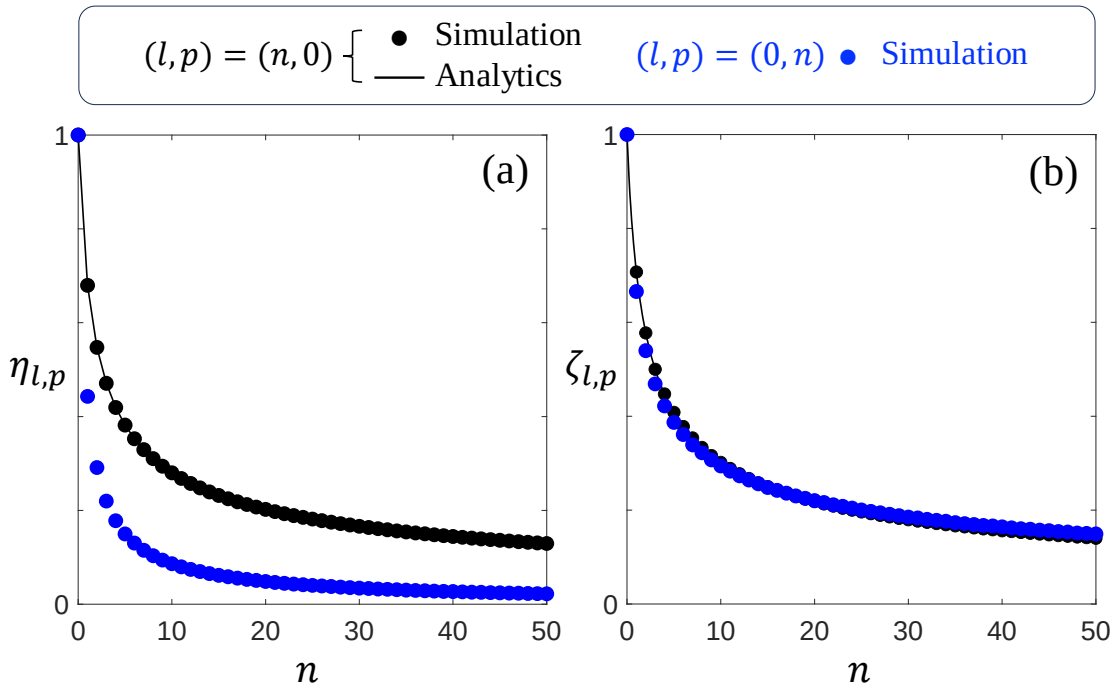

Figure 2.15 Influence of the azimuthal and radial indices on the modal beam shaping characteristics for corrected modal plates by using the appropriate input spin state. (a) Calculated modal conversion efficiency, $\eta_{l,p}$ and (b) the corresponding normalized beam waist for the Laguerre-Gauss modal decomposition, $\zeta_{l,p} = w_{\text{out}}/w_{\text{design}}$. Black color: $0 \le l \le 50$ at $p = 0$. Blue color: $0 \le p \le 50$ at $l = 0$. All data are evaluated at the nominal wavelength and using $w_{\text{in}} = w_{\text{design}}$. Analytical solution exists for $p = 0$, which gives $\eta_{l,0} = |l|!\, e^{|l|}/(1+|l|)^{1+|l|}$ and $\zeta_{l,0} = (1+|l|)^{-1/2}$ [40].

exhibits less than 1% according to previous work [49], the pixelated devices have typical scattering losses of the order of 5%. This invites design improvements when dealing with high-order modal plates.

It is noteworthy that in the framework of a single-stage strategy, the generation of high-order modes faces an issue that remains unsolved even within the limits of ideal spatial resolution. Indeed, the expected output optical power fraction that corresponds to the (l,p) mode,

$$\eta_{l,p} = \frac{4}{{w_{\text{in}}}^2}\int_0^\infty \sin^2[\Delta_{l,p}(r)/2]\exp(-2r^2/{w_{\text{in}}}^2)\, r dr\,, \tag{2.22}$$

does not have an analytical expression when $p \neq 0$ and drastically decreases with the mode order, as shown in Fig. 2.15 for $(l,p) = (n,0)$ or $(0,n)$, up to $n = 50$. In this figure, we also report on the corresponding output beam waist, which recalls the importance of selecting the proper "ruler" when performing modal decomposition analysis, not only for minimizing the number of modes that describe a given light beam. To date, there is no way to remedy this limitation.

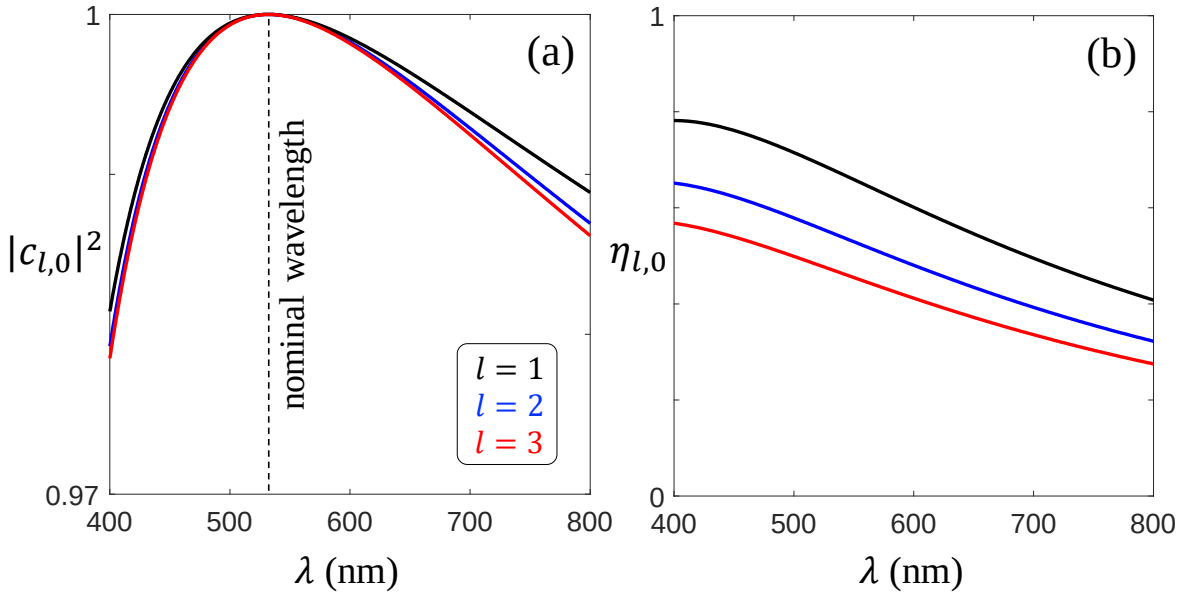

Figure 2.16 Influence of a detuned incident wavelength on the modal performances for corrected modal plates with $l = (1, 2, 3)$ using the appropriate input spin state. (a) Calculated modal power fractions $|c_{l,0}|^2$ and (b) the corresponding modal power conversion efficiencies $\eta_{l,p}$. All data are evaluated using $w_{\text{in}} = w_{\text{design}}$ and $w_{\text{out}} = w_{\text{design}}/\sqrt{1+|l|}$ for the Laguerre-Gauss modal decomposition at the nominal wavelength $\lambda_0 = 532$ nm, for which the plate is monomode.

2.3.8 Robustness to spectral and waist detuning

So far, we have explored modal performance by selecting nominal values for the wavelength and the input beam waist in relation to the chosen design. Here we numerically address the question of the extent to which detuning is detrimental to the modal performance of the fabricated optical element. On the one hand, the consequences of a spectral detuning at the nominal input beam waist in terms of modal purity and modal power conversion efficiency are shown in Fig. 2.16 for $l = (1, 2, 3)$ and $p = 0$. It appears that a modal plate designed for a wavelength of 532 nm exhibits only a slight decrease in performances regarding its purity, which is a typical feature of geometric phase optical elements, with $|c_{l,0}|^2 > 0.98$ over the whole visible range up to the near infrared. In contrast, the amount of processed light typically decreases by a factor of two over the visible domain, which suggests practical limitations whenever the photon flux is an issue. On the other hand, the resilience of modal plate performance with respect to detuning of the incident beam waist is rather good whatever the wavelength detuning, as shown in Figs. 2.17(a) and 2.17(b). In addition, our numerical investigations show that Eq. (2.11), which describes the optimal choice for the output beam waist vs the

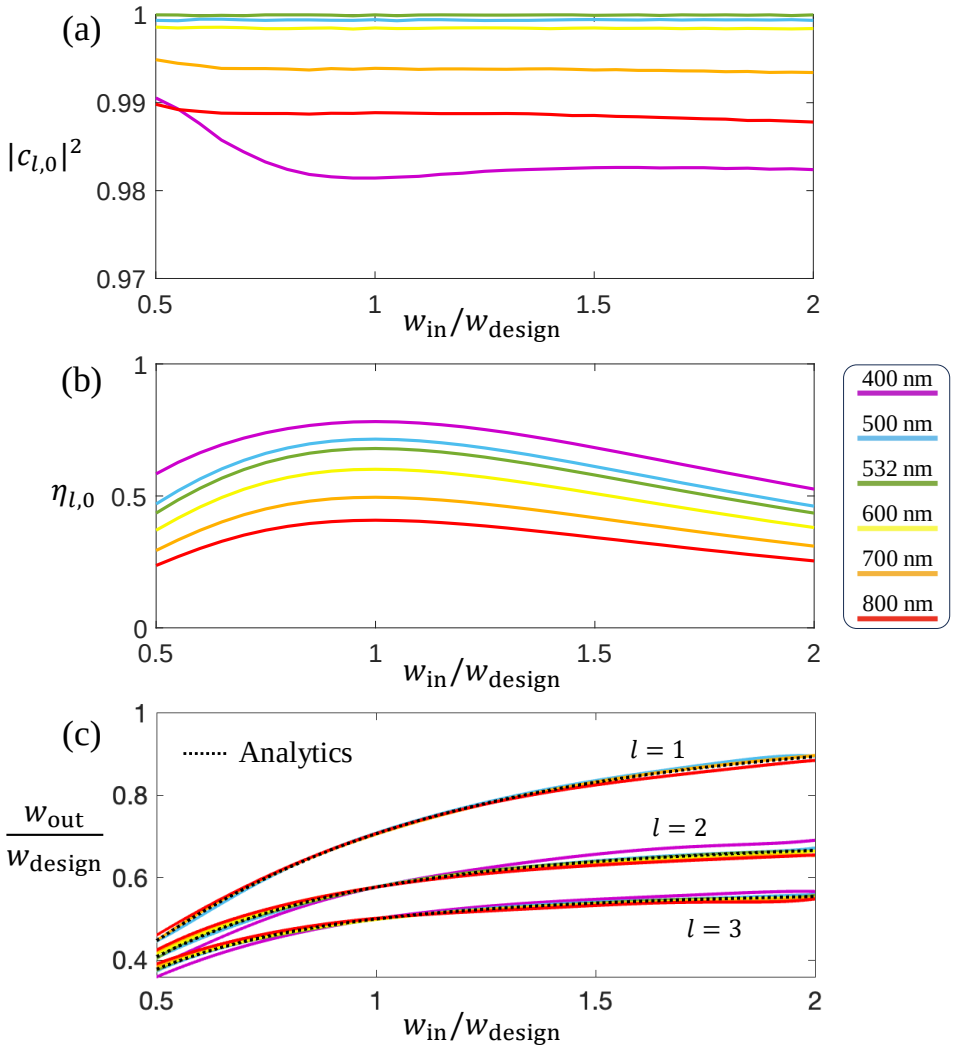

Figure 2.17 Influence of a detuned incident beam waist on the modal performances across the visible domain (color curves) for corrected modal plates using the appropriate input spin state. (a) Calculated modal power fractions $|c_{l,0}|^2$ and (b) the corresponding modal conversion efficiencies $\eta_{l,0}$ for $l = 1$. (c) Calculated normalized output beam waist $w_{\text{out}}/w_{\text{design}}$ that corresponds to panels (a,b) extended to $l = (1, 2, 3)$, where the dotted black curves refer to analytical results (Eq. (2.11)) at the nominal wavelength $\lambda_0 = 532$ nm.

incident one as far as the modal decomposition is concerned, can be used as a rule of thumb over a broad range of wavelength around the nominal one, see dotted analytical curve in Fig. 2.17(c).

These results therefore suggest that broadband spin-orbit modal beam shaping can be achieved, at least at a good approximation. This is qualitatively explored experimentally by using an incident circularly polarized supercontinuum laser beam whose waist variation over the visible domain is no larger than a few percent, see Figs. 2.18(a) and

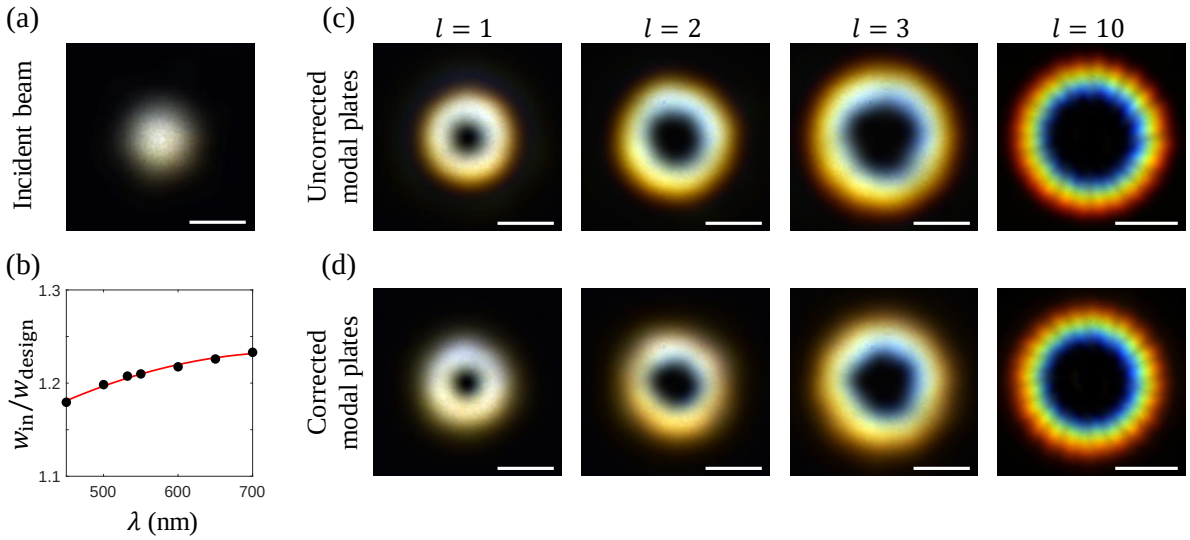

Figure 2.18 Experimental broadband modal beam shaping. (a) Intensity profile of the incident beam. (b) Dependence of the normalized incident beam waist on the wavelength in the visible domain. Markers: experimental data. Solid curve: guide for the eye. The intensity profile of the shaped beam after 20 cm propagation for (c) uncorrected and (d) corrected modal plates, for $l = (1, 2, 3, 10)$ and $p = 0$. Scale bars: 1 mm for $l = 10$, else 400 μm.

2.18(b). The experiments are done for both the uncorrected and the corrected modal plates, see Figs. 2.18(c) and 2.18(d), for which we used achromatic quarter-waveplates and polarizer for achieving circular polarization projections at the input and the output of the optical element. The observed color dispersion along the radial coordinate, which is all the more pronounced as the order of the mode increases, is due to the conjunction of at least two factors:

- the wavelength varies by a typical factor of two in the visible domain, hence leading to substantially larger beam divergence in the red than in the blue parts of the spectrum recalling that the incident beam waist is almost independent of wavelength,

- the relative "thickness" of a doughnut-shaped intensity profile of a vortex beam decreases with the increase of its topological charge l, which reduces the overlap between distinct wavelengths and leads to separation along the radial coordinate.

Present advances in the design and fabrication of spin-orbit modal plates made of laser nano-structured silica glass bring a contribution to the recent efforts devoted to single-stage modal beam shaping strategies [40–46], which might eventually seed the emergence of novel applications where compact solutions for complex amplitude shaping

is needed. In particular, the use of silica optics with macroscopic clear aperture offers valuable robustness to the photon flux that can process high-power laser beam that does not require power amplification, the latter remaining a nontrivial task to date [60]. The relative insensitivity of the modal performances to the input beam characteristics (wavelength, waist radius) is another remarkable asset of the developed optical elements. Importantly, the inherent issue related to the spatial modulation of the dynamic phase prevents fully taking advantage of the key spin-orbit interaction feature that involves spin-controlled wavefront reversal. The right/left symmetry is indeed broken by design, as discussed in Sec. 2.3.1. Although spatially modulated form-birefringence comes with spatial modulation of the dynamic phase, a compensation approach based on bilayer structuring has been suggested [61], though not yet investigated experimentally. Another limitation requiring further work is associated with the substantial decrease in modal power conversion efficiencies as the mode order increases.

2.4 Addressing spin degeneracy issue

This section deals with work performed in collaboration with the group of G. Li from the Southern University of Science and Technology (SusTech), China, for the fabrication part.

In this section, we solve one of the issues related to the spatial modulation of the dynamic phase, which prevents fully taking advantage of the key spin-orbit interaction feature. That is to say, so far we cannot obtain a mode for both incident spin states,

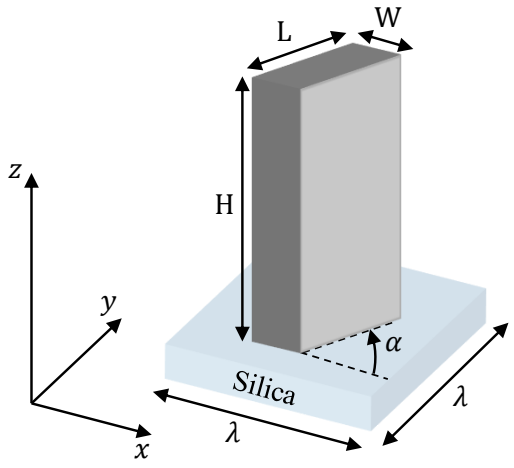

Figure 2.19 Sketch of a meta-atom made of silicon nitride nanopillar of length L, width W, and height H, and having a λ^2 footprint standing on a silica substrate.

which would allow a spin-controlled azimuthal index of $E_{l,p}$ mode at a fixed p imposed by the design. The idea is to spatially modulate the birefringence with a uniform dynamic phase over all the structured area. This is achieved using a set of meta-atoms (see Fig. 2.19) providing a constant dynamic phase and enabling to fully cover the required retardance range.

2.4.1 Design

Here we choose metasurfaces made of silicon nitride nanopillars standing on a silica substrate designed to operate at 532 nm nominal wavelength. Each of them is placed at the center of a unit cell with a typical λ^2 footprint paving annular manner and characterized by their height H, length L, width W, and orientation polar angle α in the (x, y) plane, as shown in Fig. 2.19. Since the nanofabrication requires maintaining a fixed height of nanopillars, the modal design is realized through spatial variation of the other geometrical parameters, including W, L, and α. The geometric parameters of each nanopillar are determined numerically using the Finite-difference time-domain (FDTD) method by evaluating the magnitude and phase of the contra-circular complex electric field transmittance in the (x, y) plane (see Eq. (2.2)),

$$t_{-\sigma} = ie^{i\Phi_{\mathrm{dyn}}} \sin\left(\pi\delta/\lambda\right), \tag{2.23}$$

whose amplitude and phase profiles are shown in Figs. 2.20(a) and 2.20(b), respectively.

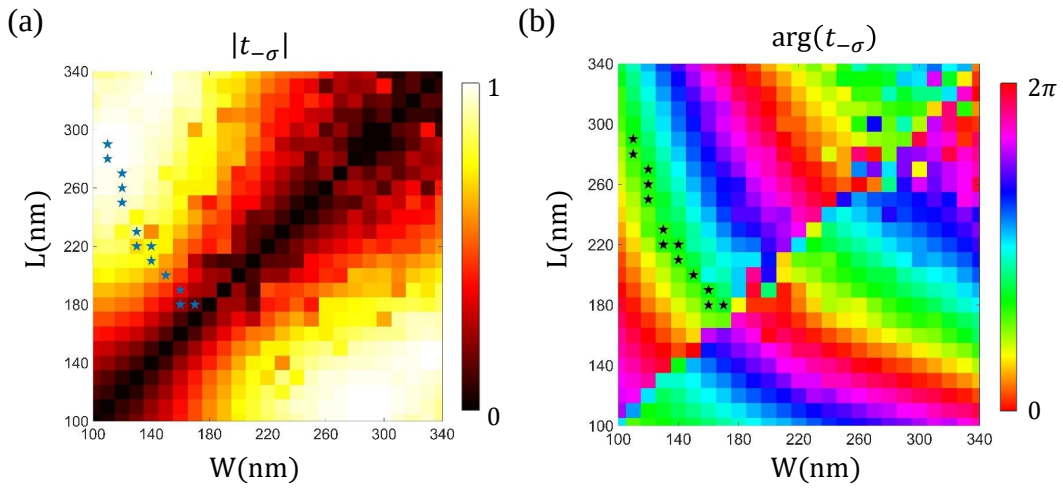

Figure 2.20 Numerical simulations of the amplitude (a) and phase (b) of the complex transmittance $t_{-\sigma}$ associated with the contra-circularly polarized electric field contribution to the output field, for H = 1200 nm, 100 nm ≤ (L, W) ≤ 340 nm and operating wavelength λ = 532 nm. The selected meta-atoms that are used to fabricate the modal beam shapers reported in this work are marked with blue (a) and black (b) star markers. This figure is credited to Q. Ma.

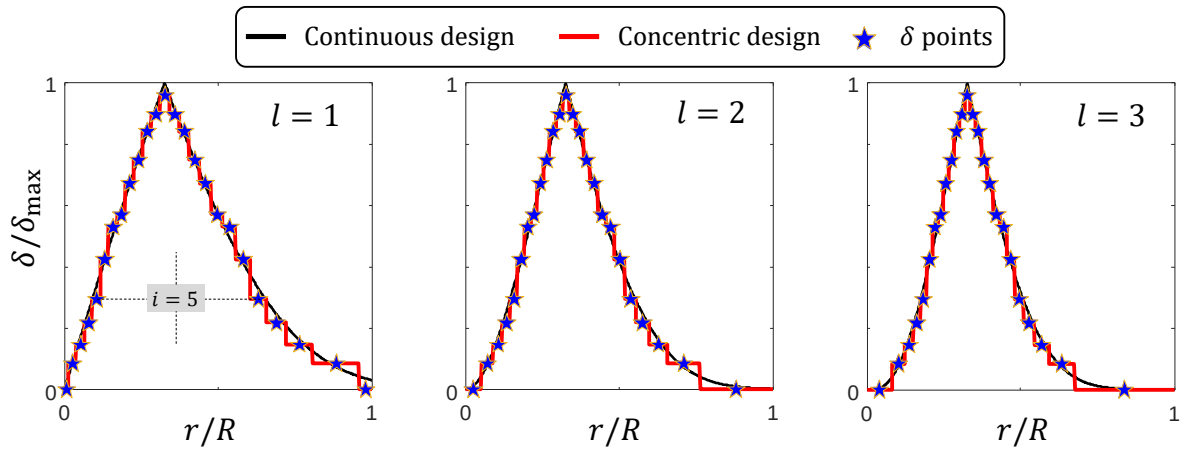

Figure 2.21 Radial profiles of the retardance for $l = 1, 2, 3$ modal plates with radius $R = 540$ μm. Black curve: theoretical profile defined by Eq. (2.7). Red curve: concentric design according to Eq. (2.24). Except for the zone ($i = 13$) associated with $\delta_{\max}$, there are pairs of zones having identical meta-atoms, see the example for $i = 5$ on the leftmost panel. The star markers correspond to the retardance value of each zone.

Thus, the retardance and dynamic phase can be expressed as a function of transmittance according to

$$\delta = \frac{\lambda}{\pi} \arcsin |t_{-\sigma}|, \tag{2.24}$$

$$\Phi_{\text{dyn}} = \arg(t_{-\sigma}) - \pi/2 \tag{2.25}$$

where the constant offset in Eq. (2.25) can be taken as an arbitrary value.

From the FDTD simulations performed with $H = 1200$ nm, 100 nm $\leq$ (L, W) $\leq$ 340 nm by 10 nm steps both for L and W, $N = 13$ meta-atoms are chosen in order to satisfy the requirement Φ_{dyn} = constant, while selecting retardance values as close as $\delta_i = \frac{i-1}{N-1}\frac{\lambda}{2}$ for i integer from 1 to 13, as illustrated in Fig. 2.20 with star markers. This implies a concentric design that consists of 25 radial zones from $R_1 = 0$ to $R_{25} = 540$ μm associated with a discrete set of 13 distinct meta-atoms for $w_{\text{in}} = 250$ μm incident waist value. Accounting from the fact that the footprint of a nanopillar is is λ^2, the number of nanopillars at a distance r from the center of the device is chosen as the closest integer to the value of $2\pi r/\lambda$.

The retardance profiles for $l = 1, 2, 3$ plates with concentric and continuous design are shown in Fig. 2.21, where $\delta_{\max} = \lambda/2$. The star markers indicate the selected retardance values for each radial zone, according to Eq. (2.24). By construction, there are pairs of zones having identical meta-atoms except for the zone associated with $\delta_{\max}$. This is illustrated with a dashed line in the leftmost panel of Fig. 2.21 for $i = 5$ and $i = 21$, as an example.

2.4.2 Fabrication

The modal metasurfaces are fabricated using electron beam lithography. The fabrication process begins with the deposition of a silicon nitride film on a double-polished fused silica substrate using a plasma-enhanced chemical vapor deposition (PECVD) method. A poly-methyl methacrylate (PMMA) electron beam resist layer is then spin-coated onto the substrate, followed by baking. A charge-dissipation layer is applied on top of the PMMA layer, and the sample is exposed to electron beam lithography to define the metasurface patterns. After exposure, the charge-dissipation layer is removed with deionized water, and the PMMA is developed using a solvent mixture. A chromium (Cr) hard mask is then deposited on the patterned PMMA layer via electron beam evaporation, and the Cr patterns are revealed after the lift-off process. The sample is then etched through the silicon nitride film, and the final metasurfaces are obtained by removing the remaining Cr layer with a Cr etchant solution. We refer to Ref. [45] and its supplementary material for a more detailed presentation of the fabrication technology and procedure.

Top and oblique SEM images of the central part of $l = 1, 2, 3$ plates are shown in Fig. 2.22(a). In addition, top view SEM images of each of the 13 individual meta-atoms are shown in Fig. 2.22(b). The bright microscope images are shown in Fig. 2.23 for all three plates, which allows for identifying the concentric design and where different values of retardance qualitatively refer to the brightness.

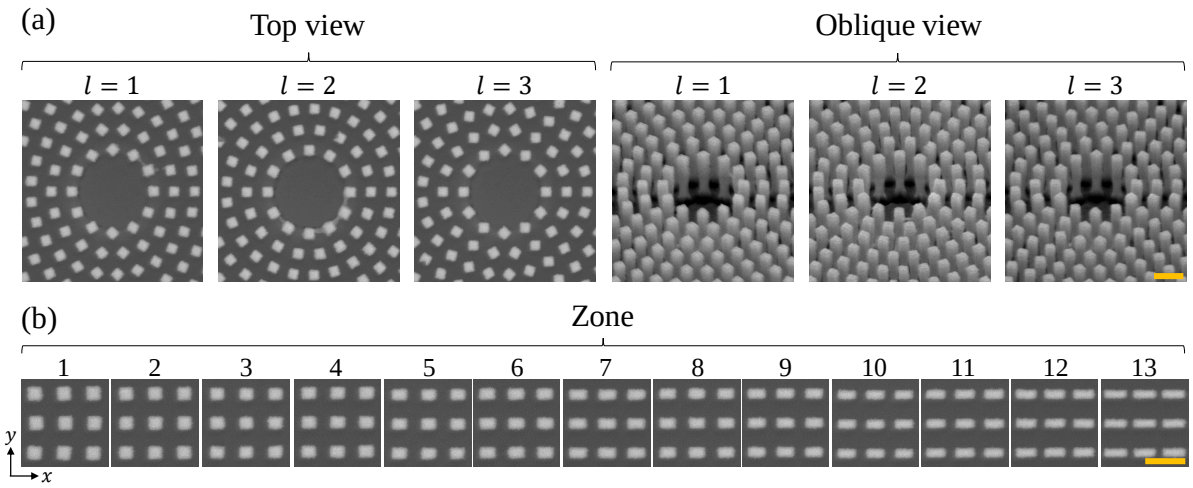

Figure 2.22 (a) SEM images of the central part of the fabricated modal metasurfaces for $l = 1, 2, 3$ in top view and side view. (b) The top view SEM images of the 13 meta-atoms selected from simulations, as detailed in the previous section. Scale bar: 500 nm. The figure is credited to Q. Ma.

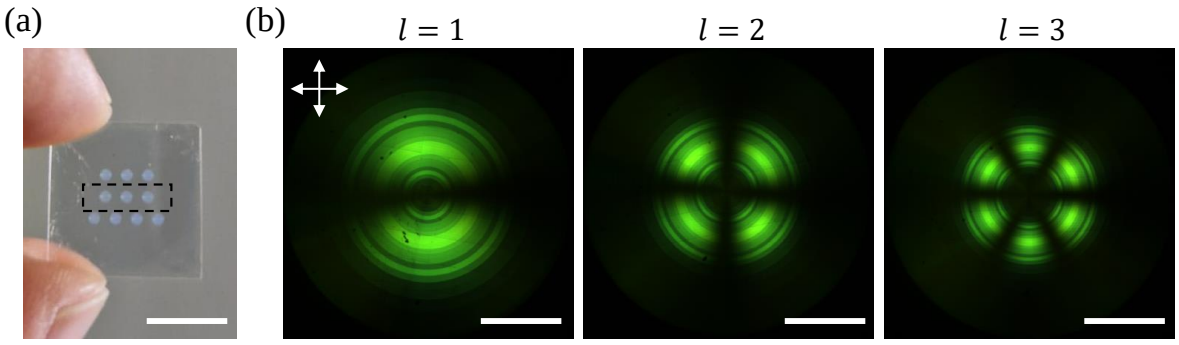

Figure 2.23 (a) Image of the fabricated metasurfaces with 1.08 mm diameter disk-shaped footprint observed in ambient illumination conditions. The three structures in the center (see dashed box) correspond to $l = 1, 2, 3$ modal shapers used in this work. Scale bar: 7 mm. (b) XPol microscope images of the three plates under white light illumination. Scale bar: 300 μm.

2.4.3 Characterization of the plates

Once the quality of the fabricated metasurface is validated by direct structural analysis using SEM imaging, polarimetric characterization of the optical properties of the devices is performed. The method is the same as that we used for the characterization of silica optics modal elements discussed in Sec. 2.3.3. Both retardance and optical

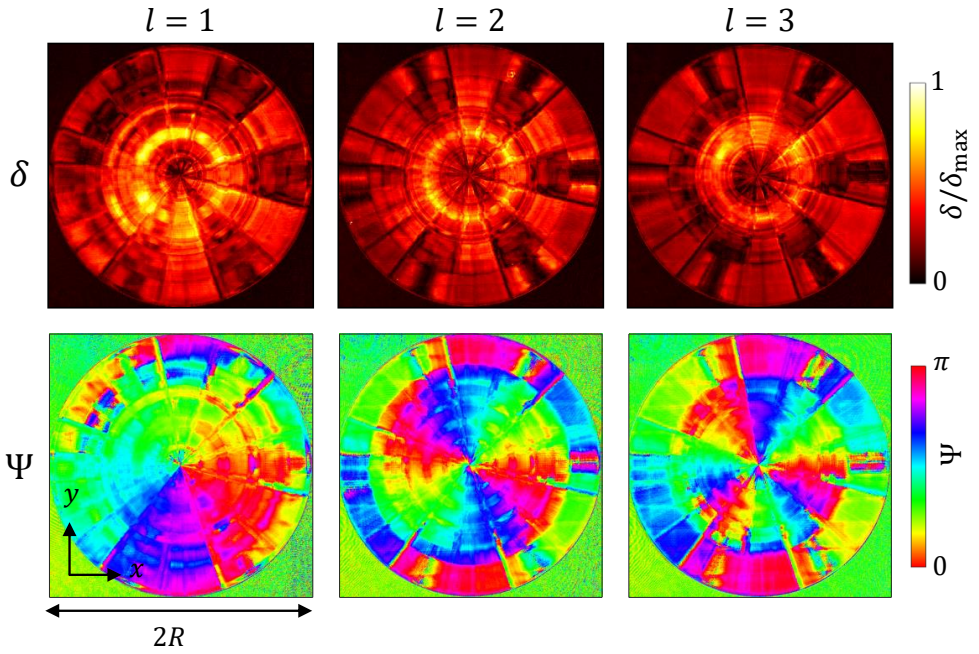

Figure 2.24 Experimental maps of the anisotropic optical features in the (x, y) plane for $l = 1, 2, 3$ modal plates retrieved via polarimetric imaging using left-handed circularly polarized 532 nm laser beam. Top: retardance (δ). Bottom: slow axis orientation angle (Ψ).

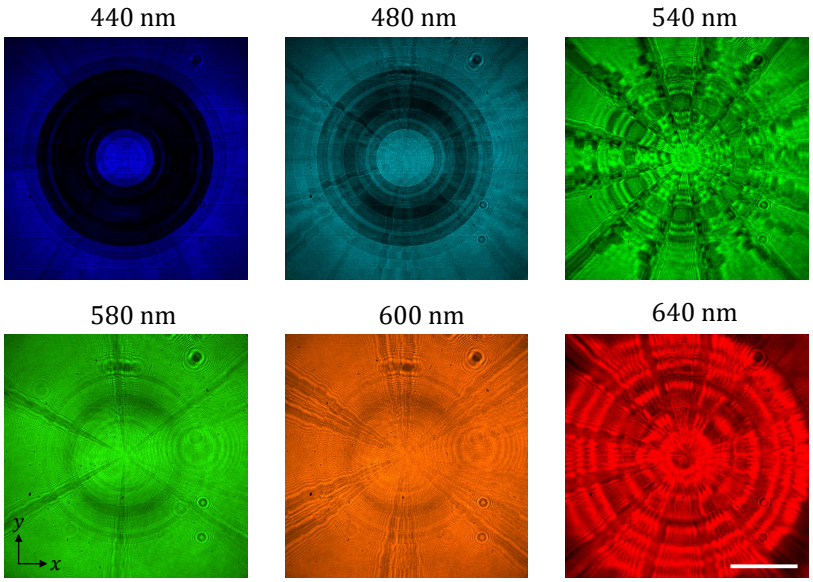

Figure 2.25 Co-circular projection of the output field at the sample plane for a set of wavelengths 440 nm, 480 nm, 540 nm, 580 nm, 600 nm and 640 nm for $l = 2$. Scale bar: 300 μm.

axis orientation profiles of the plates with $l = 1, 2, 3$ are shown in Fig. 2.24 for the nominal 532 nm wavelength using a left-handed circularly polarized incident beam. As such, these observations invalidate the possible use of the fabricated metasurfaces as LG modal plates of good quality. Still, for the sake of getting know-how from the fabricated devices, we agreed with our collaborators to perform further optical and modal characterization before planning a new round of fabrication of the samples. Especially, we mention that the shown metasurfaces are actually the second generation ones. Indeed, we demonstrated that the first generation shows even worse optical performances (not shown here). Therefore, recalling that metasurfaces have wavelength-dependent optical properties, we decided to perform a study at different wavelengths around the nominal one.

This is done by using a supercontinuum laser source, spectral filters, and achromatic QWPs to prepare and project circular polarization states. The results are illustrated in Fig. 2.25, where the co-circular component of the output field at the sample plane is shown for $l = 2$ plate for a right-handed circular incident polarization state, as an example. The sample exhibits strong scattering behavior at certain wavelengths, including close to the nominal wavelength. However, clearer images are obtained at other wavelengths, as demonstrated in Fig. 2.25.

Furthermore, we performed a more detailed spectral assessment to determine the optimal operational wavelength for the fabricated devices. The approach involved ana-

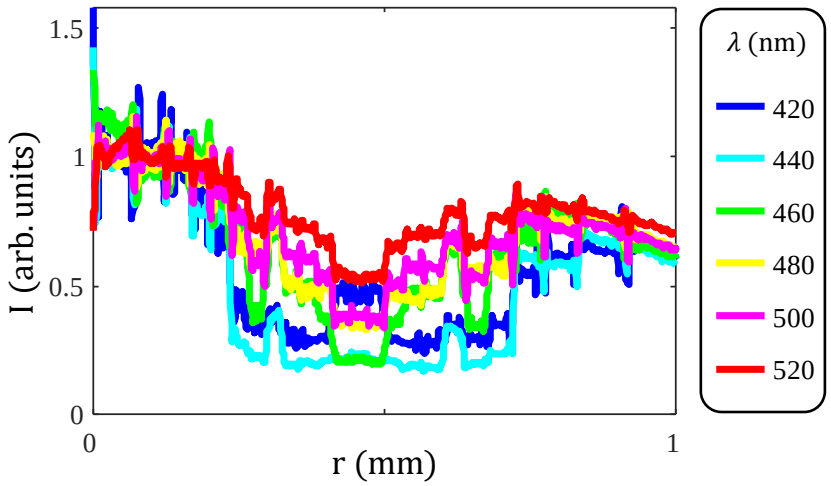

Figure 2.26 Azimuth-averaged intensity profiles of co-circular component of the output field at the sample plane for a set of wavelengths 420 nm, 440 nm, 460 nm, 480 nm, 500 nm and 520 nm for $l = 2$.

lyzing the co-circular output to identify the minimum dip in the radial intensity profile, noting that reaching zero value indicates that the half-wave criterion is fulfilled. Based on this analysis, summarized in Fig. 2.26, we opt for 460 nm as a practical optimal wavelength for an experimental attempt to report spin symmetric modal behavior, even though the half-wave criterion is not clearly validated.

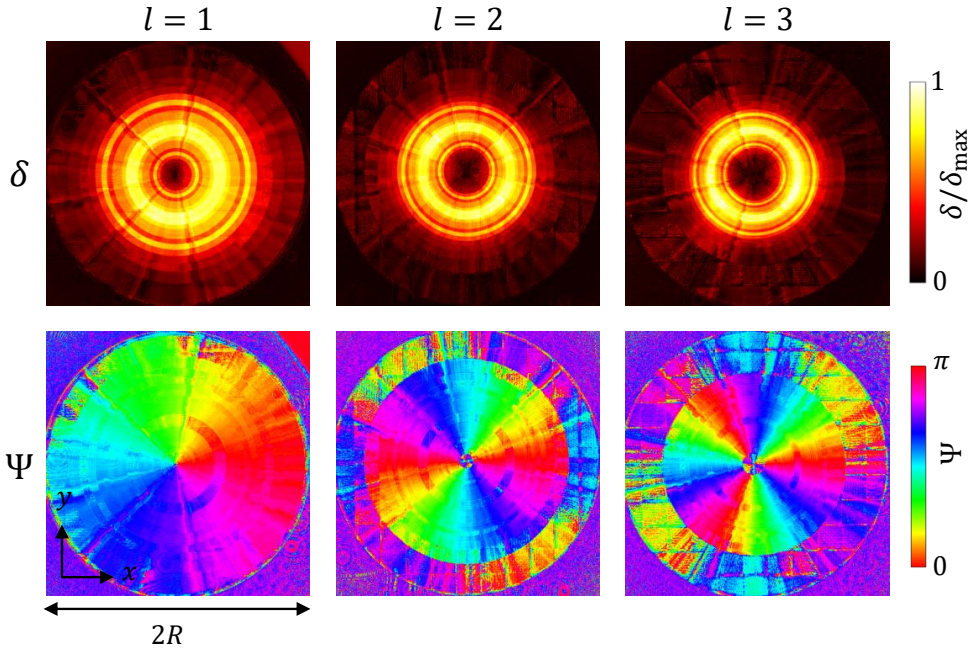

Figure 2.27 Experimental maps of the anisotropic optical features in the (x, y) plane for $l = 1, 2, 3$ modal plates retrieved via polarimetric imaging at 460 nm laser beam. Top: retardance (δ). Bottom: slow axis orientation angle (Ψ).

Moreover, the polarimetric analysis at a wavelength of 460 nm, as shown in Fig. 2.27, still reveals some fabrication issues, indicating inaccuracies in the fabrication of some annular zones. However, the results are qualitatively better than those obtained at a nominal wavelength of 532 nm (compare Fig. 2.24 and Fig. 2.27). This motivates us to study beam propagation with the aim of revealing, at least qualitatively, the sought-after spin symmetric modal behavior.

2.4.4 Assessing modality via beam propagation

As done in Sec. 2.3.4 in the context of silica optics modal shapers we used an incident circularly polarized Gaussian laser beam with $w_{\text{in}} = w_{\text{design}}$, and the contra-circularly polarized spatial intensity distribution of the beam at a distance z from the sample up to 40 cm is imaged on a camera with 5 mm step. The experimental setup is shown in Fig. 2.28(a). From the recorded images, the azimuth-averaged radial intensity profiles are calculated from which we reconstruct meridional intensity cross-sections shown in Fig. 2.28(b) for left- and right-handed circularly polarized incident beam and for the plate with $l = 2$. The experimental results are compared with simulated expecta-

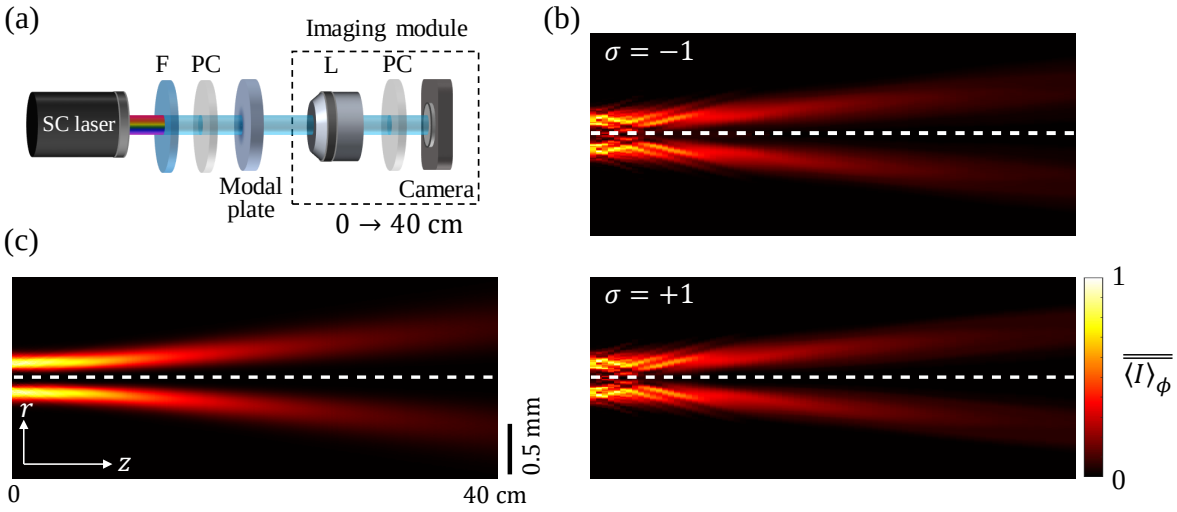

Figure 2.28 (a) The experimental setup to record the contra-circularly polarized spatial intensity distribution of the beam at a distance z from the sample up to 40 cm. F: 460 nm spectral filter. PC: Polarization controller made of a linear polarizer and an achromatic quarter-waveplate. L: 4× microscope objective lens with numerical aperture NA = 0.1. (b) Experimental normalized azimuth-average intensity distribution in the (z, r) plane for $l = 2$ modal plate in both circularly polarized incident cases. (c) Simulated azimuth-average intensity distribution for $l = 2$ modal plate. The experimental data is recorded by moving an imaging module of "L + PC + Camera" along the z axis by steps of 5 mm over a distance of 40 cm. The simulation is made using the Fourier beam propagation method.

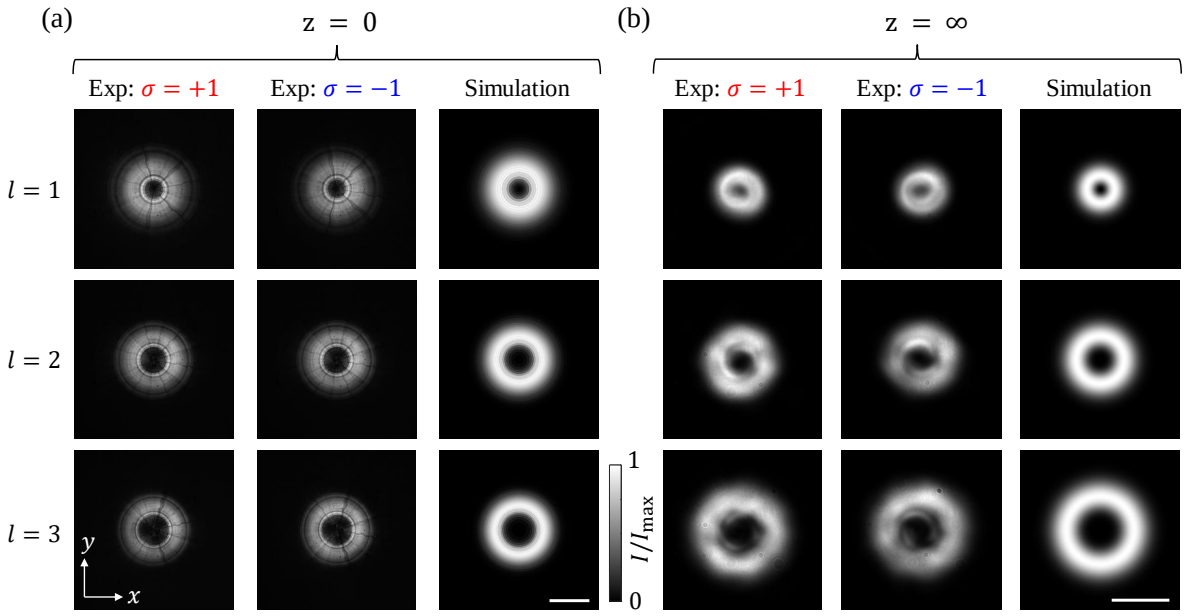

Figure 2.29 Experimental intensity profiles of the beam (a) at the sample plane ($z = 0$) and (b) in the far field ($z = \infty$) for $l = 1, 2, 3$ modal plates using left- and right-handed circularly polarized 460 nm incident laser beam. The simulated profiles are shown in the right column. Scale bar: 0.5 mm.

tions, presented in Fig. 2.28(c). Although spin symmetry is achieved, the fabrication imperfections of these plates clearly lack a pure mode behavior. Nevertheless, achieved results set a new standard with respect to previous work where the spin symmetry was crippling [45].

A short summary of the propagation behavior of the set of three modal metasurfaces is provided in Fig. 2.29. There, intensity profiles at ($z = 0$) and ($z = \infty$) are shown in both cases of $\sigma = \pm 1$ for the experiment, while the simulation results are identical for both $\sigma = \pm 1$ states. From the azimuth-averaged radial intensity profiles in the far

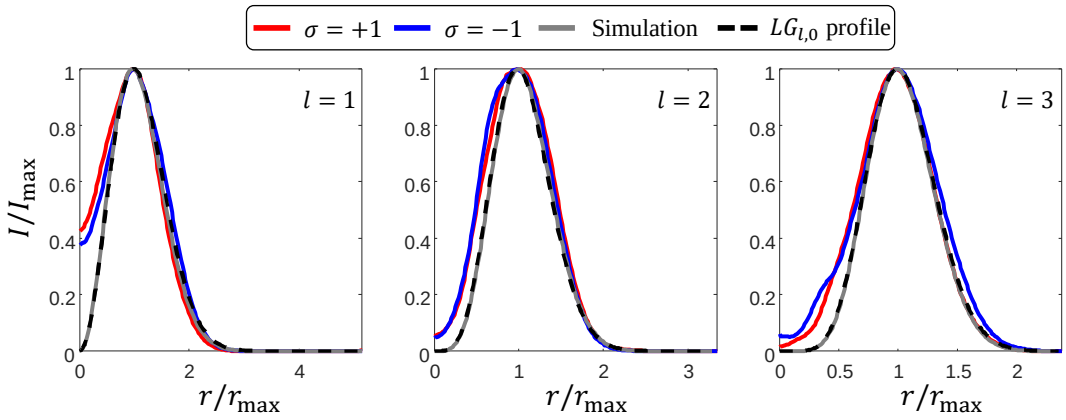

Figure 2.30 Azimuth-averaged radial intensity profiles in far field for $l = 1, 2, 3$ modal plates using 460 nm laser beam. Blue: left-handed circular incident. Red: right-handed circular incident. Gray: Simulation. Dashed black: Theoretical LG profile. $r_{\max}$ is defined as $I(r_{\max}) = \max_r[I(r)]$.

field, illustrated in Fig. 2.30, we note that the right/left symmetry is indeed preserved (blue and red curves), however, the discrete design still does not give exact LG profile as a slight deviation between simulated curves (gray curve) and theoretical LG profiles (dashed black curve) is observed.

In summary, we have presented the first experimental attempt to achieve spin symmetric modal plates in the framework of optical metasurfaces. Achieving precise fabrication, however, remains challenging with the chosen approach, which leaves room for further work with our collaborators.

2.5 Addressing high-order radial modes from metasurfaces

In Sec. 2.3 and Sec. 2.4 we have discussed only the fundamental case with $p = 0$. In this section, we extend the spin symmetric modal beam shaping approach to generate modes with nonzero radial indices in the infrared domain using silicon-based metasurfaces, hence changing the fabrication approach with respect to the attempt presented in the previous section. These metasurfaces have been fabricated by the group of F. Romanato from Padova University, Italy, in a collaborative framework.

2.5.1 Design and fabrication

As already described in Sec. 2.4, the meta-atoms here are also selected from a simulation study to provide a constant dynamic phase and enable to fully cover a retardance range from 0 to $\lambda/2$. Following Eq. (2.7) we define the anisotropic properties of the optical material (retardance δ and slow axis orientation Ψ) that now depend both on l and p according to

$$\delta_{l,p}(r) = \frac{\lambda}{\pi} \arcsin\left(\frac{|L_p^{|l|}(2r^2/{w_{\text{out}}}^2) r^{|l|}| \exp\left[\frac{-r^2(1-\zeta_{l,p}^2)}{{w_{\text{in}}}^2 \zeta_{l,p}^2}\right]}{\max\left(|L_p^{|l|}(2r^2/{w_{\text{out}}}^2) r^{|l|}| \exp\left[\frac{-r^2(1-\zeta_{l,p}^2)}{{w_{\text{in}}}^2 \zeta_{l,p}^2}\right]\right)} \right) \tag{2.26}$$

and

$$\Psi_{l,p}(r,\phi) = \frac{\sigma}{2} l\phi - \frac{\pi}{4}[1 - \text{sign}(L_p^{|l|}(2r^2/{w_{\text{out}}}^2)] \tag{2.27}$$

where the coefficient $\zeta_{l,p}$ is chosen to maximize the modal power conversion efficiency $\eta_{l,p}$ defined by Eq. (2.22). For the sake of illustration, we focus on three plates characterized by $l = 1$ and $p = 0, 1, 2$. The metasurface devices are designed to operate at $\lambda = 1310$ nm incident wavelength and $w_{\text{in}} = 175$ μm. The corresponding maps combining

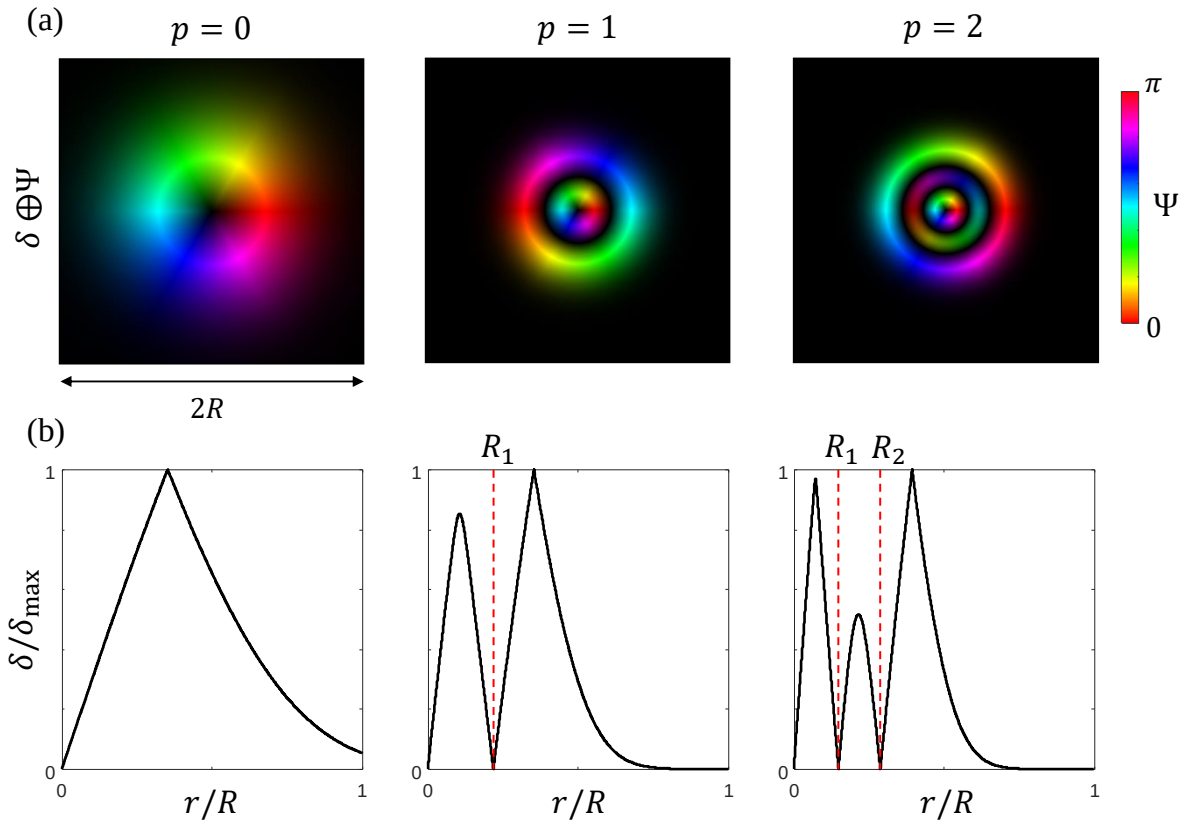

Figure 2.31 The design of modal plates. (a) combination of retardance and optical axis orientation ($\delta \oplus \Psi$) of $l = 1$, $p = 0, 1, 2$ plates, where the brightness refers to $\delta/\delta_{\max}$ and the hue colormap refers to Ψ. (b) Radial profile of retardance of three plates where the red dashed lines show the radial positions corresponding to sign changes of the phase factor in Eq. (2.27).

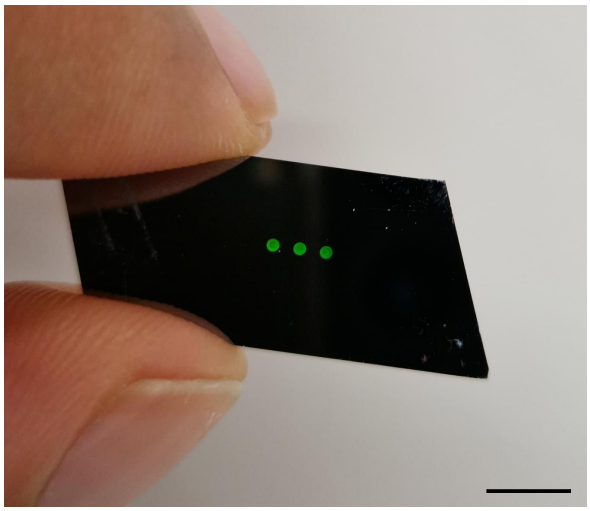

Figure 2.32 Image of the three fabricated metasurfaces with 0.7 mm diameter disk-shaped footprint observed in ambient illumination conditions. Scale bar: 5 mm.

the retardance and the slow axis orientation are shown in Fig. 2.31(a). In addition, the radial profile of retardance is shown in Fig. 2.31(b) where the dashed lines indicate the radial positions corresponding to the sign changes of the phase factor in Eq. (2.27).

The direct image of the three fabricated devices having $2R$ = 0.7 mm disk-shaped structured area is shown in Fig. 2.32.

2.5.2 Characterization

The polarimetric characterization of the optical properties of the devices is performed as for previous modal shapers presented in this chapter. Figure 2.33 summarizes the results for the three metasurfaces at the nominal wavelength 1310 nm. The left, middle, and right columns represent the retardance, slow axis orientation, and azimuth-averaged re-

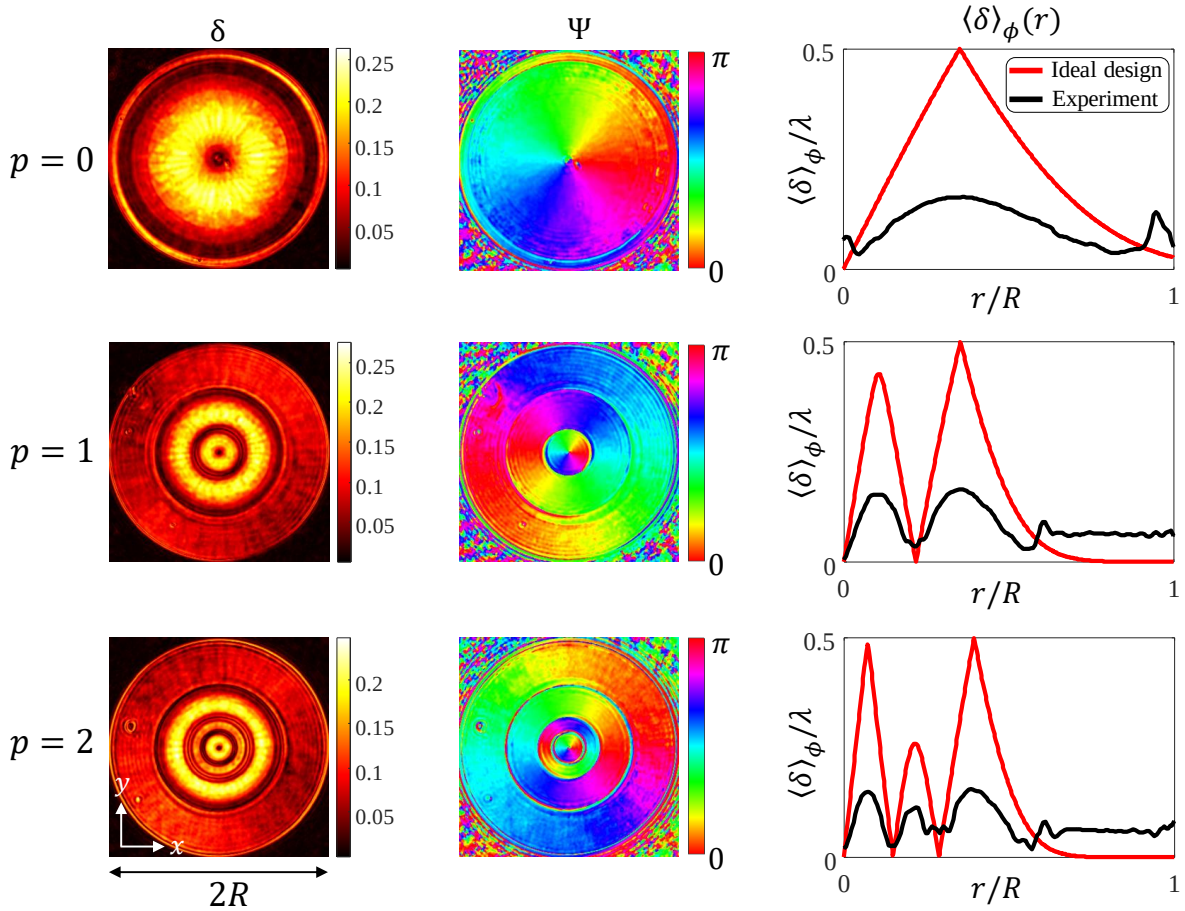

Figure 2.33 Experimental maps of the anisotropic optical features in the (x, y) plane for the three plates with l = 1, p = 0, 1, 2 retrieved via polarimetric imaging using λ = 1310 nm laser beam. Left column: retardance (δ), where colormap shows the value of retardance in microns. Middle column: slow axis orientation angle (Ψ). Right column: azimuth-averaged radial profile of retardance, where red curves refer to the Eq. (2.26), and black curves show the experimental results.

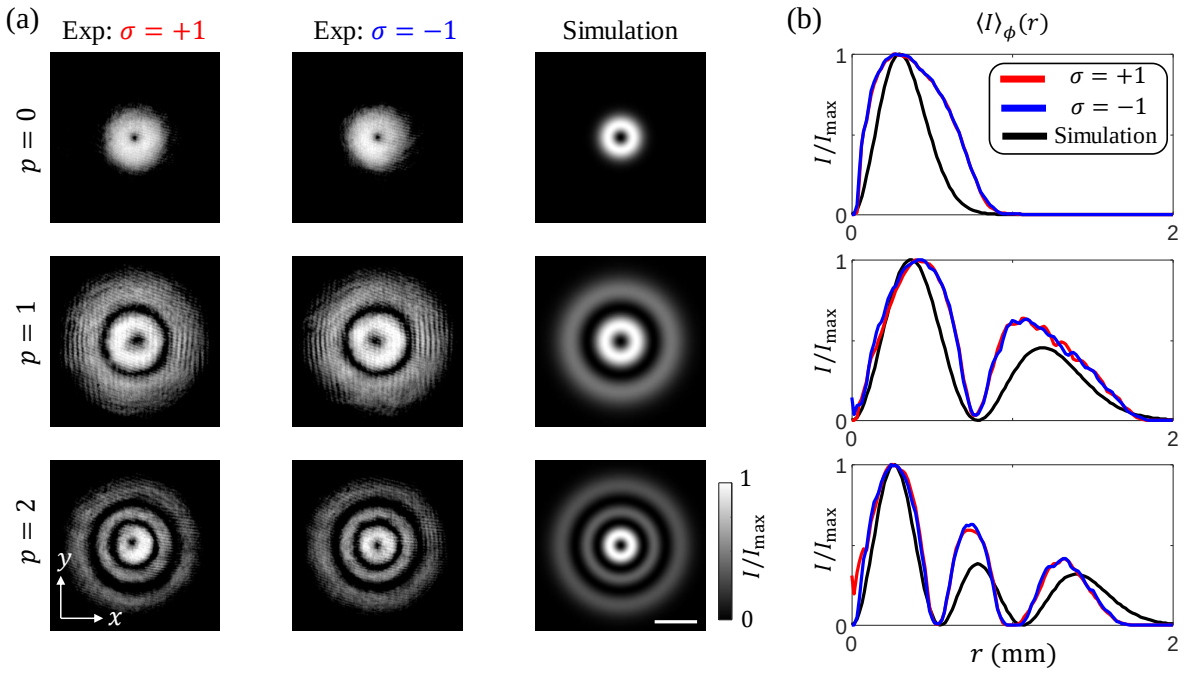

Figure 2.34 (a) Experimental and simulated transverse intensity profiles of the beam in the propagating far field for the plates with $l = 1$ and $p = 0, 1, 2$ using left- and right-handed circularly polarized 1310 nm incident laser beam. Scale bar: 0.5 mm. (b) Corresponding azimuth-averaged radial intensity profiles for both circular polarization states. Black curves correspond to the theoretical LG profiles. Data acquisition credited to A. Vogliardi.

tardance profile, respectively. Azimuth-averaged retardance profiles exhibit a systematic lowering of the retardance with respect to the profiles expected from the design. Additionally, a nonzero background is observed in regions where the retardance is expected to vanish. This tells that either the design has been improperly coded at the fabrication, or the fabrication itself suffered from unexpected issues. We eventually realized that both explanations apply in the present case and another fabrication run has been prepared as the writing of the present manuscript is ending. The new set of samples was received at the beginning of October 2024, whose exploitation is thus left for the very near future.

Nevertheless, we performed a qualitative modal assessment by looking at the beam profiles in the propagating far field, and corresponding azimuth-averaged radial intensity profiles, as illustrated in Fig. 2.34, which shows that the spin symmetric modal behavior is obtained. Of course, further qualitative analysis is not particularly relevant due to the understood issues related to the presented metasurfaces. Therefore, we are leaving it for the next experimental campaign.

CHAPTER 3

Vectorial beam shaping

3.1 Vector field topological structures: skyrmions

A wide range of physical quantities manifest as vector fields, which can adopt complex configurations leading to the formation of stable, topologically protected structures, known as skyrmions that are characterized by a topological invariant.

Since their introduction in particle physics [62], skyrmions have been endorsed as valuable universal candidates to transport, process, and store information owing to their topological stability and robustness. The existence of skyrmionic fields extends to waves of various nature such as acoustic [63, 64], water [65] and optical [66] waves as well. In optics, skyrmion textures have been found for the electric field vector [67], the spin vector [68] and the Poynting vector [69]. Indeed, many kinds of skyrmionic optical vector fields have been studied and experimentally observed [70–76].

In this chapter, we will focus on the generation and manipulation of only one type of optical skyrmions, 2D Stokes skyrmions, that are constructed as topological vector field structures from the 3D reduced Stokes vector,

$$\mathbf{s} = \frac{(|E_x|^2 - |E_y|^2, 2\,\mathrm{Re}(E_x^* E_y), 2\,\mathrm{Im}(E_x^* E_y))}{|E_x|^2 + |E_y|^2}\,, \tag{3.1}$$

which describes the polarization state of fully polarized paraxial light field propagating along the z axis with complex electric field $\mathbf{E} = E_x\,\mathbf{x} + E_y\,\mathbf{y}$ [52]. This kind of vector field has been introduced in the end of Chapter 1. It is noteworthy that the structure of beams having spatially varying polarization state is easily accessible experimentally from a finite set of intensity-only measurements using standard polarization optics, which makes them attractive for the advent of optical information networks [77, 78].

One of the attributes of skyrmions is the so-called Skyrme number, which counts how many times the vector field (in our case, the reduced Stokes vector $\mathbf{s}$) wraps the unit sphere (in our case the Poincaré sphere). It can be calculated in the transverse plane from a surface integral

$$N = \iint_A \Sigma(x, y)\, dxdy\,. \tag{3.2}$$

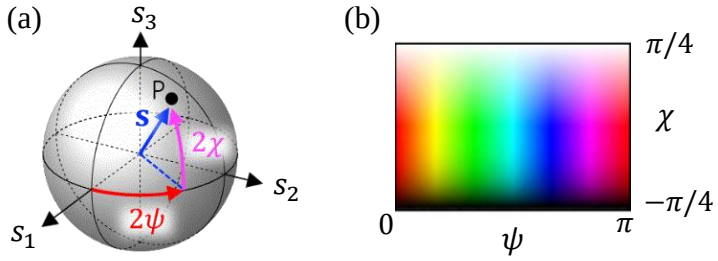

Figure 3.1 (a) Representation of the Poincaré sphere, where any point P is described by Stokes vector **s**, polarization ellipse azimuth ψ, and ellipticity χ. (b) Colormap used for Stokes vector and texture coloring, where each point on the Poincaré sphere is represented by a hue indicating the ψ angle, and brightness referring to the ellipticity χ.

where A is the surface of the integration and $\Sigma(x,y)$ is the Skyrme density

$$\Sigma(x,y) = \frac{1}{4\pi}\mathbf{s}\cdot\left(\frac{\partial \mathbf{s}}{\partial x}\times\frac{\partial \mathbf{s}}{\partial y}\right). \tag{3.3}$$

The basic expression of the Stokes skyrmionic beams can be given, up to an important phase factor, by the superposition of orthogonally polarized LG modes $E_{l,p}$ presented in Chapter 1, see Eq. (1.17), according to

$$\mathbf{E}(\mathbf{r}) = a_1 E_{l_1,p_1}(\mathbf{r})\,\mathbf{e} + a_2 e^{i\theta} E_{l_2,p_2}(\mathbf{r})\,\mathbf{e}_\perp\,, \tag{3.4}$$

where $a_1 > 0$ and $a_2 > 0$ are weighting coefficients, θ is the intermodal phase, and $\mathbf{e}\cdot\mathbf{e}_\perp = 0$.

For the sake of visual rendering, we introduce a color code that uniquely connects **s** to given values of hue and brightness, as shown in Fig. 3.1. A set of representative skyrmionic textures for the Stokes vector **s** is shown in Fig. 3.2 and Fig. 3.3 for a few combinations of LG beams, at $z = 0$ setting $a_1 = a_2 = 1$ and choosing different options for the pair of orthogonal polarization states $(\mathbf{e},\mathbf{e}_\perp)$. Fundamental skyrmions, which contain all possible Stokes vectors $\mathbf{s} = (s_1,s_2,s_3)$ once, are described for instance by $(l_1,p_1) = (0,0)$ and $(l_2,p_2) = (\pm1,0)$ and are respectively characterized by a Skyrme number $N = \pm1$ whatever θ. In this particular case, choosing $(\mathbf{e},\mathbf{e}_\perp)$=$(\mathbf{e}_+,\mathbf{e}_-)$, where $\mathbf{e}_\pm$ refers to left- and right-handed circular polarization states, the intermodal phase θ controls the helicity of the skyrmion, said to be of the Néel type for $\theta = (0,\pi)$ and of the Bloch-type for $\theta = \pm\pi/2$, see Figs. 3.2(a,b). For $(l_1,p_1) = (0,0)$ and $(l_2,p_2) = (-1,0)$, the phase θ only rotates the texture around the z axis, see Figs. 3.2(c,d). Moreover, switching from the basis $(\mathbf{e}_+,\mathbf{e}_-)$ to the basis $(\mathbf{e}_-,\mathbf{e}_+)$ flips the polarity (on-axis vector direction) of the skyrmion (i.e., $s_3(r=0) = +1 \rightarrow s_3(r=0) = -1$) and the vorticity of the transverse field $\mathbf{s}_\perp = (s_1,s_2)$, while N is unchanged, as shown in Figs. 3.2(e−h). In addition, using

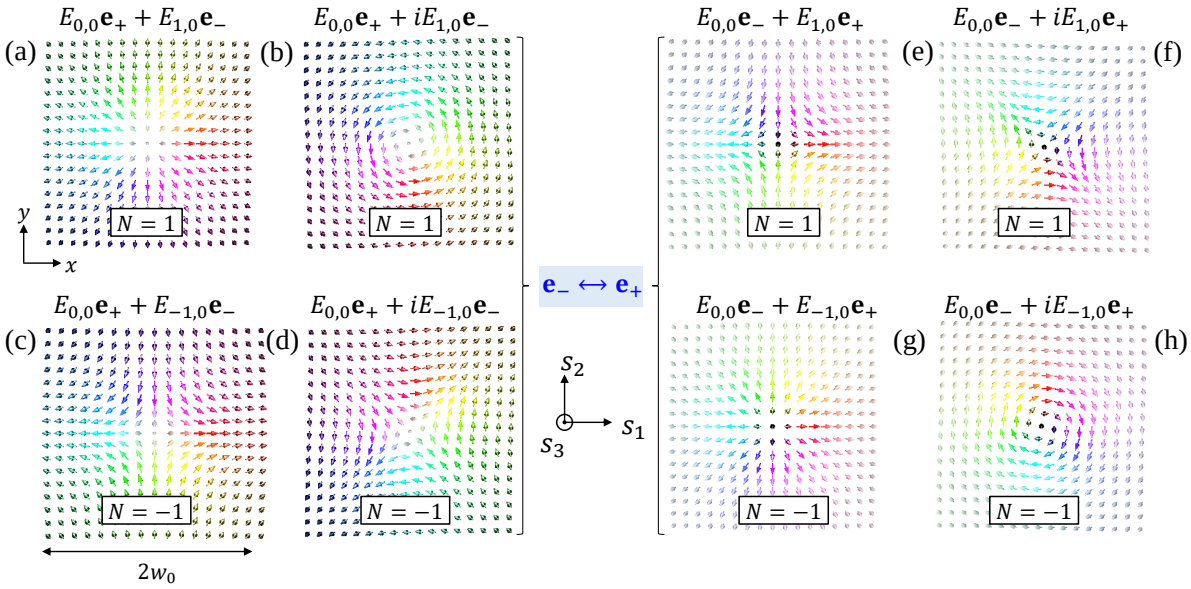

Figure 3.2 Representative set of Stokes vector fields in the plane (x, y) that correspond to fundamental skyrmions with $N = \pm 1$, where $w_0 = w(0)$. The Stokes vector fields are colored according to the bijective relationship illustrated in Fig. 3.1, which associates every point on the Poincaré sphere to a given point of a colormap.

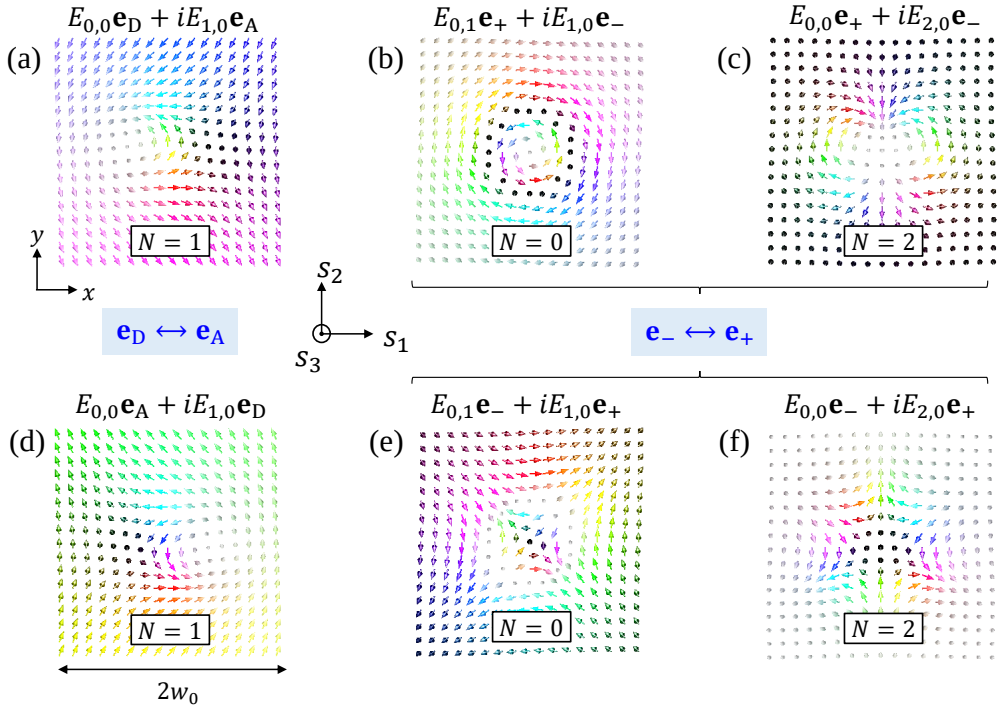

Figure 3.3 Representative set of Stokes vector fields in the plane (x, y) that correspond to bimerons [panels (a) and (d)], skyrmioniums [panels (b) and (e)] and second-order skyrmions [panels (c) and (f)].

another basis than circular ones for the Laguerre-Gaussian superposition transforms the skyrmion at fixed N, as shown in Figs. 3.3(a,d) which correspond to bimerons [79].

The skyrmion textures can also be confined in a finite region when constructed from modes with nonzero radial indices p_1 or p_2, as shown in Figs. 3.3(b,e) for $(l_1, p_1) = (0, 1)$ and $(l_2, p_2) = (1, 0)$ in the circular basis and which correspond to skyrmionium associated with $N = 0$. Finally, higher-order skyrmions are obtained by increasing $|l_1 - l_2|$, as shown in Figs. 3.3(c,f) for $(l_1, p_1) = (0, 0)$ and $(l_2, p_2) = (2, 0)$ in the circular basis and which correspond to second-order skyrmion with $N = 2$.

3.2 From modal plates to skyrmionic plates

Having developed plates that generate pure LG modes in Chapter 2, a rather natural question is whether the spin-orbit modal waveplates could provide a way to generate skyrmionic beams, which we explore in the present section. A straightforward option is to use two distinct LG modal plates and superimpose the resulting beams to form skyrmions. Instead, here we are addressing the question of whether a proper modal superposition can be achieved using just a single modal plate. As outlined in Sec. 2.1, the field emerging from the modal plates consists of two orthogonally polarized components, one of which (the contra-circularly polarized component) is associated with a pure LG mode. Does the superposition of co-circular and contra-circular components generate a skyrmionic beam? This question has motivated the following work presented in this section, carried out in collaboration with Y. Shen from Nanyang Technological University, Singapore.

3.2.1 Principle of skyrmionic waveplates

Here we propose using optical structured waveplates made of two-dimensional anisotropic materials as described in Sec. 1.1.2 and implemented in Chapter 2 in the context of modal beam shaping from circularly-polarized incident Gaussian beam. By extending it to an arbitrary incident polarization state, one gets the following unitary polarization transformation scheme [80],

$$\sum_{\sigma=\pm1} \alpha_\sigma \, \mathbf{e}_\sigma \xrightarrow[\Psi]{\Delta} \sum_{\sigma=\pm1} \alpha_\sigma \big(\cos \tfrac{\Delta}{2} \, \mathbf{e}_\sigma + i \sin \tfrac{\Delta}{2} \, e^{i2\sigma\Psi} \mathbf{e}_{-\sigma} \big), \tag{3.5}$$

where the complex weighting coefficients satisfy $|\alpha_-|^2 + |\alpha_+|^2 = 1$. To introduce the prin-

ciple of skyrmionic waveplates, here we propose doubly inhomogeneous spin-orbit waveplates that are associated with radially varying phase retardation $\Delta(r)$ and azimuthally varying slow axis orientation $\Psi(\phi)$ described by

$$\Delta(r) = 2\arcsin\left\{\left(r\sqrt{2}/w_{\text{design}}\right)^{n}\exp\left[n\left(1/2 - r^2/w_{\text{design}}^2\right)\right]\right\} \tag{3.6}$$

$$\Psi(\phi) = n\phi/2 \tag{3.7}$$

where r and ϕ are the polar coordinates, and n is an integer. This corresponds to an uncorrected modal plate for $(l,p) = (\sigma n, 0)$, see Chapter 2. Such a waveplate thus operates the following transformation,

$$E_{0,0}\sum_{\sigma=\pm1}\alpha_\sigma\,\mathbf{e}_\sigma \xrightarrow[\Psi(\phi)]{\Delta(r)} \sum_{\sigma=\pm1}\alpha_\sigma\left(\sum_p \beta_{0,p}E_{0,p}\,\mathbf{e}_\sigma + \gamma_{l,0}E_{l,0}\mathbf{e}_{-\sigma}\right), \tag{3.8}$$

where $\beta_{0,p}$ and $\gamma_{l,0}$ are weighting coefficients. The corresponding modal decomposition is evaluated numerically and is illustrated in Fig. 3.4 for $n = 1, 2, 3$ and left-handed circular incident polarization state.

From Fig. 3.4, ideal modal plates for $p = 0$ as given by Eqs. (3.6) and (3.7) are not providing the simple superposition between two contra-circularly polarized LG modes due to a non-monomodal p-spectrum for the co-circular component. Therefore, we expect to generate imperfect skyrmionic texture, a priori associated with degraded topological stability as the field propagates. This is qualitatively assessed numerically from the

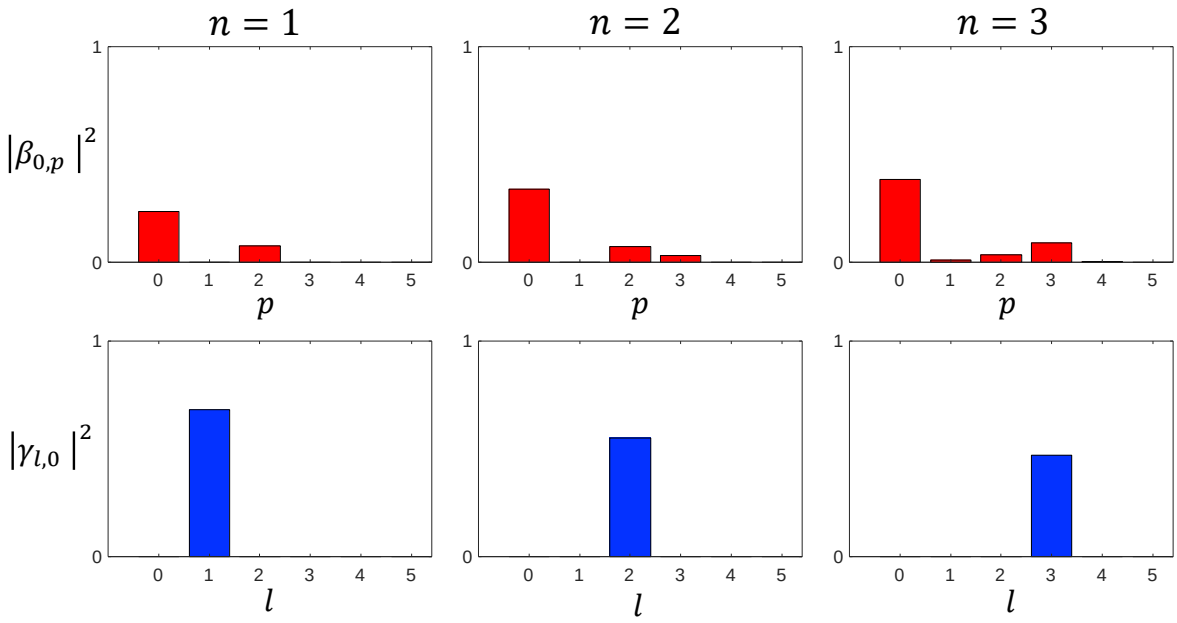

Figure 3.4 The power fraction of each $E_{l,p}$ mode in the superposition according to Eq. (3.8) for $n = 1, 2, 3$ and left-handed circular incident polarization state. Top panel: modal decomposition for the co-circular component. Bottom panel: modal decomposition for the contra-circular component.

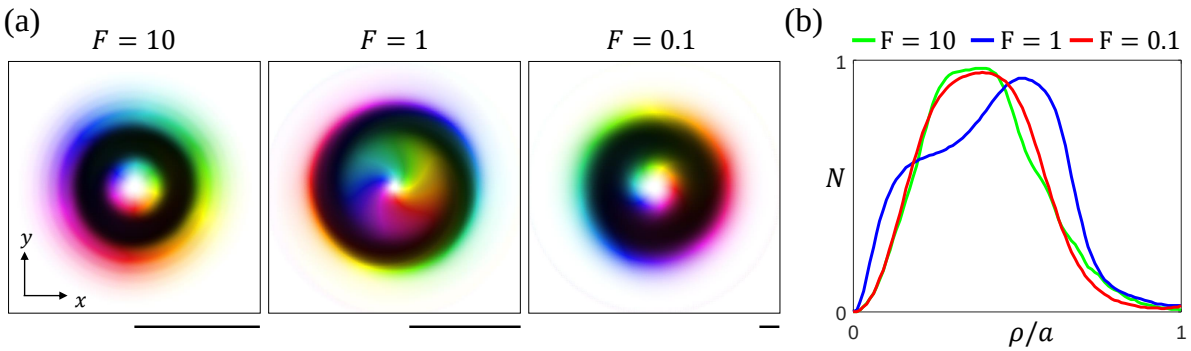

Figure 3.5 (a) Numerical simulations of the Stokes textures $\{\mathbf{s}\}$ vs propagation by considering typical values for the Fresnel number F associated with near ($F \gg 1$), intermediate ($F \sim 1$) and far field ($F \ll 1$) regions. See Fig. 3.1 for the colormap. (b) Corresponding Skyrme number over a disk of radius ρ where a refers to half of the panel size for each case. Simulation parameters: incident left-handed circular polarization state, $w = 1$ mm, $\lambda = 500$ nm, and $F = (10, 1, 0.1)$. Scale bar: 2mm.

analysis of skyrmionic texture in the near, intermediate, and far field regions that are typically associated with a Fresnel number $F = w^2/(\lambda z)$ larger than, of the order of, and smaller than unity, respectively, where $w = w_{\text{design}}$ is the incident beam waist located at the sample plane that defines $z = 0$ and λ is the wavelength. The simulation results are shown in Fig. 3.5 and qualitatively highlight a quasi-first-order skyrmion embedded in the central part of the field whatever the propagation distance, though noting that the whole beam itself is not a skyrmionium. More quantitatively, the corresponding Skyrme number over a disk of radius ρ is illustrated in Fig. 3.5(b) according to this equation

$$N(\rho) = \iint_{\sqrt{x^2+y^2}<\rho} \Sigma(x, y)\, dxdy\,. \tag{3.9}$$

We note that the relative variation of the maximum value of Skyrme number (N_{max}) over the three values of F (namely, $\text{std}(N_{\text{max}})/\overline{N}_{\text{max}}$), is 2.1 %. Based on these results, we thus have explored experimentally such a situation, which is addressed in the following sections.

3.2.2 Optical characterization of skyrmionic waveplates

As skyrmionic waveplates here we use Laguerre-Gauss modal waveplates made from nanostructured silica glass and designed for $p = 0$, $l = \sigma n$ with $n = (1, 2, 3)$ and 532 nm, as in Ref. 42. This choice may appear as nonideal because we know that such waveplates suffer from uncorrected dynamic phase modulation, as discussed in Chapter 2. However, the actual chronology of the experimental developments during this thesis work led us to this choice. We note that, once we have obtained optimal spin symmetric modal plates,

some of the results presented hereafter might deserve to be revisited, which however goes beyond the present PhD study.

The plates from Ref. 42 are actually associated with doubly inhomogeneous structure both in retardation Δ and optical axis orientation Ψ described by Eqs. (3.6) and (3.7), respectively. The optical characterization of the waveplates is summarized in Fig. 3.6, where the images of the plates between crossed linear polarizers and under white light illumination are shown in panel (a), while the doubly inhomogeneous structure is highlighted in panel (b) by using previously introduced polarimetric analysis.

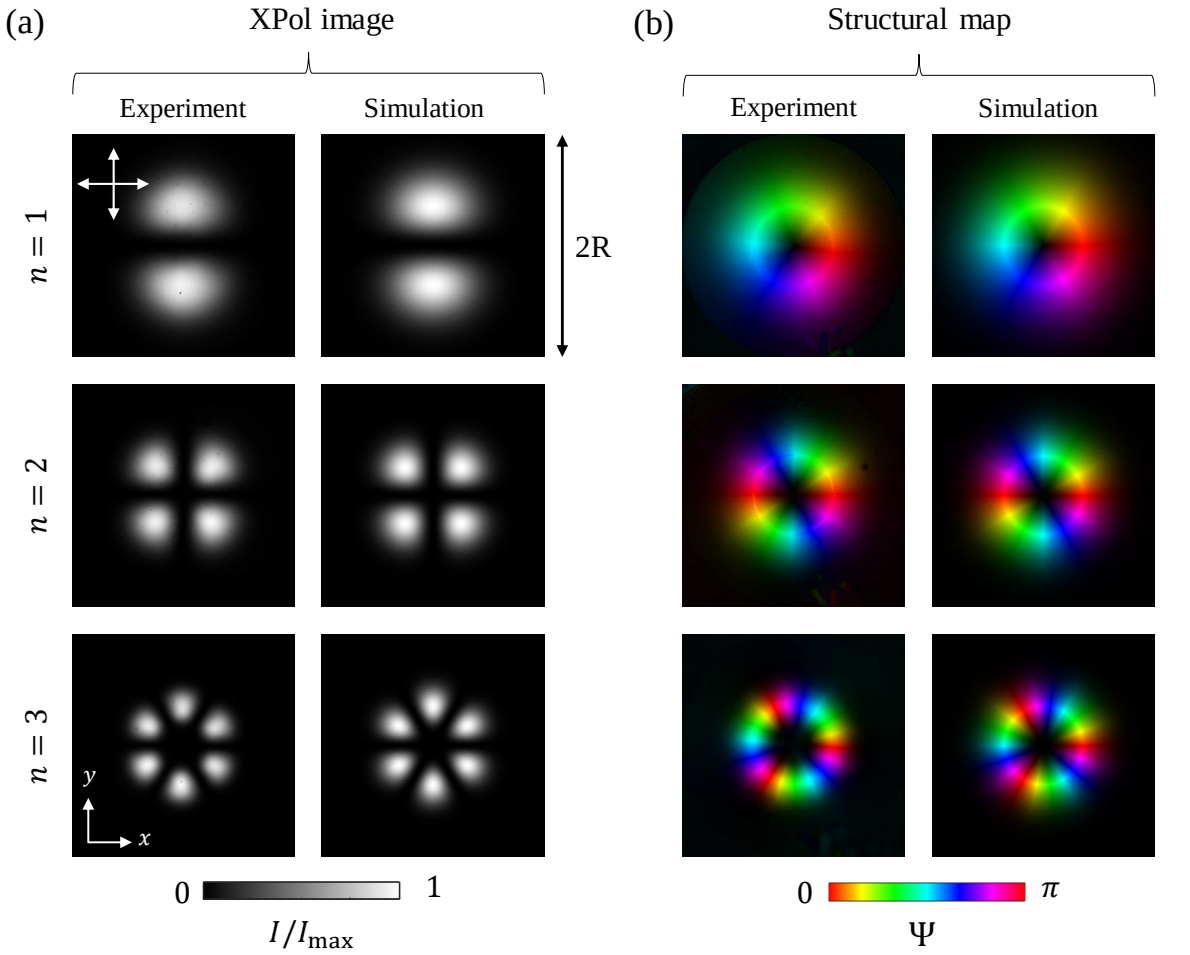

Figure 3.6 Optical characterization of the spin-orbit skyrmionic waveplates of order $n = (1, 2, 3)$ designed according to Eqs. (3.6) and (3.7) with $w_{\text{design}} = 1.5$ mm and whose structural footprint corresponds to a disk of radius $R = 3$ mm. (a) White light image of the waveplates between crossed linear polarizers. (b) The combined maps of birefringent phase retardation and optical axis orientation, where the brightness refers to Δ/π and the hue colormap refers to Ψ. The polarimetric data is obtained using a circularly polarized supercontinuum laser beam spectrally filtered at 633 nm with beam waist radius 3.6 mm at the sample plane.

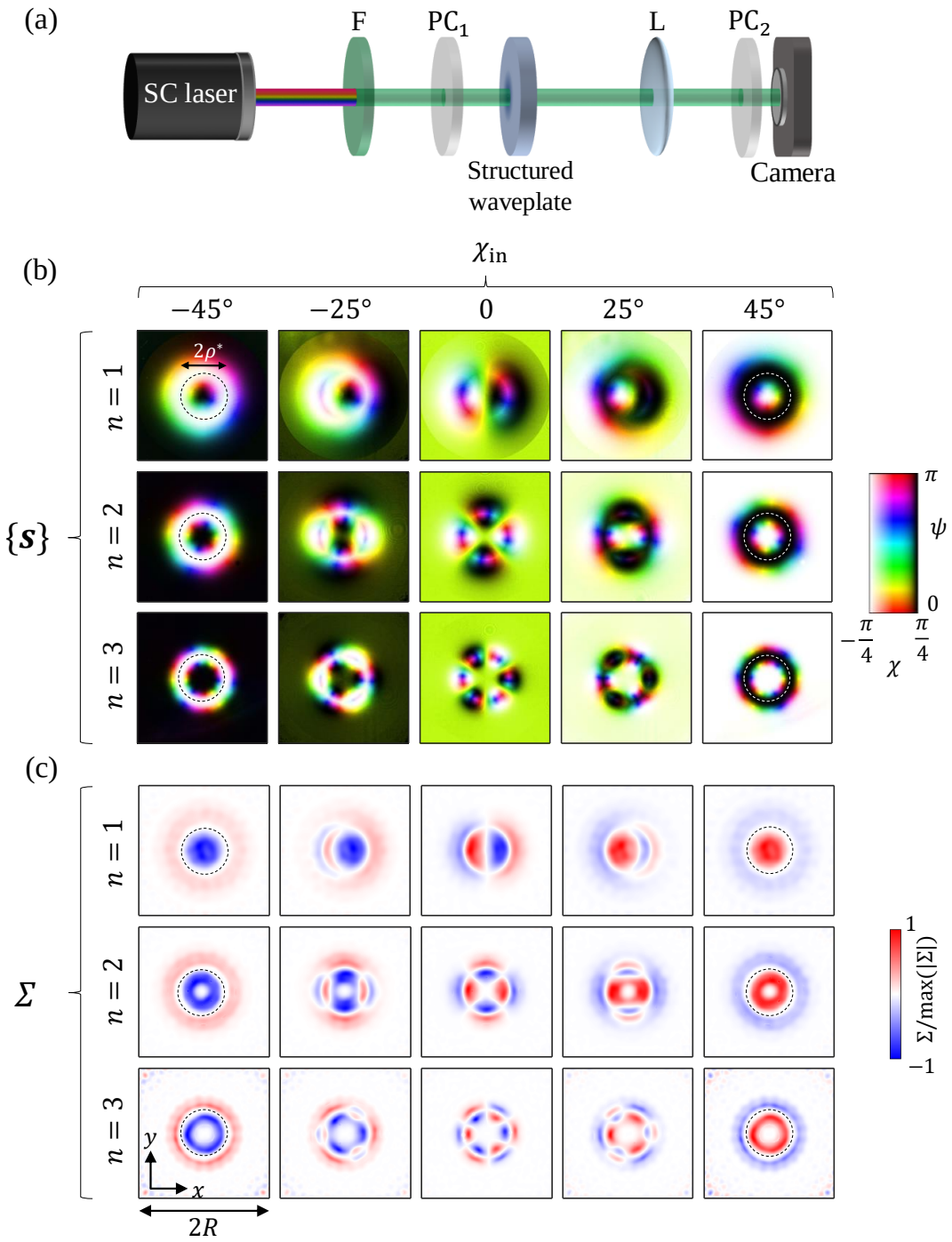

Figure 3.7 (a) Experimental setup for full Stokes polarimetric analysis of the skyrmionic waveplates at 532 nm wavelength. F: spectral filter for 532 nm wavelength. PC_1: polarization controller made of a linear polarizer, QWP, and HWP to achieve an arbitrary incident polarization state. L: imaging lens with 150 mm focal length. PC_2: polarization controller allowing to record with the camera the intensity distribution of the output field projected on H, V, D, A, L, and R polarization states. Experimental (b) Stokes texture $\{\mathbf{s}\}$ and (c) Skyrme density Σ at the output of the skyrmionic waveplate with $n = 1, 2, 3$ for $\chi_{\text{in}} = 0, \pm 25°, \pm 45°$ and fixed $\psi_{\text{in}} = 45°$ incident polarization states. The dashed circles refer to the disk of radius ρ^* that defines a nth-order skyrmion of charge $N^* = \sigma n$ for an incident helicity σ.

3.2.3 Skyrmionic texture emerging from the sample

The experimental demonstration of skyrmionic texture is carried out in the visible domain at λ = 532 nm wavelength using a collimated supercontinuum laser beam with 3.6 mm beam waist radius and spectrally filtered at 532 nm, see the experimental setup shown in Fig. 3.7(a). The experimental results of Stokes texture at the output of skyrmionic waveplate with $n = 1, 2, 3$ are illustrated in Fig. 3.7(b) for five arbitrary incident polarization states ($\psi_{\text{in}} = 45°$, $\chi_{\text{in}} = 0, \pm 25°, \pm 45°$), including left-handed ($\chi_{\text{in}} = 45°$)

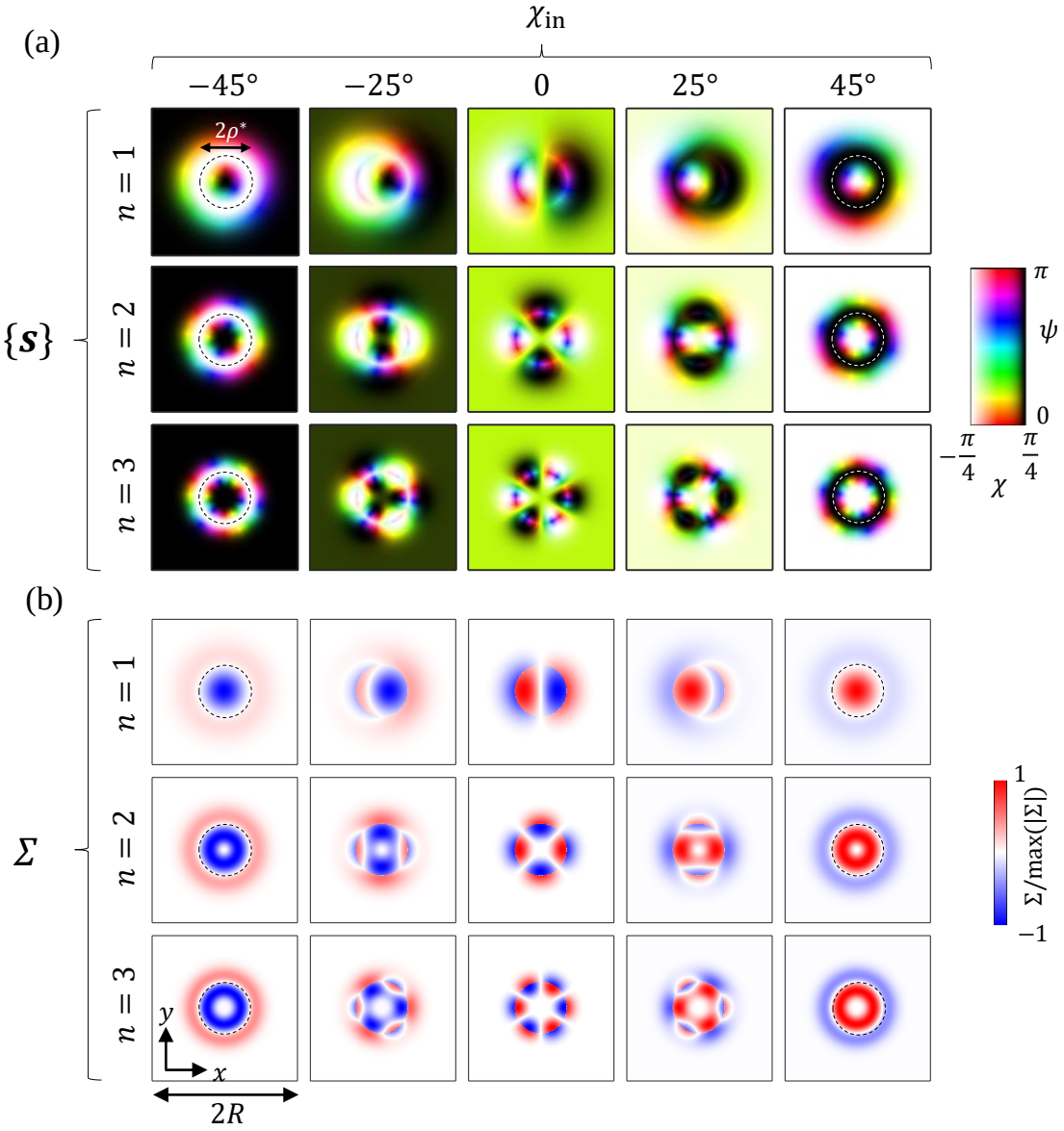

Figure 3.8 Simulation results of (a) Stokes textures {s} and (b) Skyrme density Σ corresponding to the the counterpart of Figs. 3.7(b) and 3.7(c).

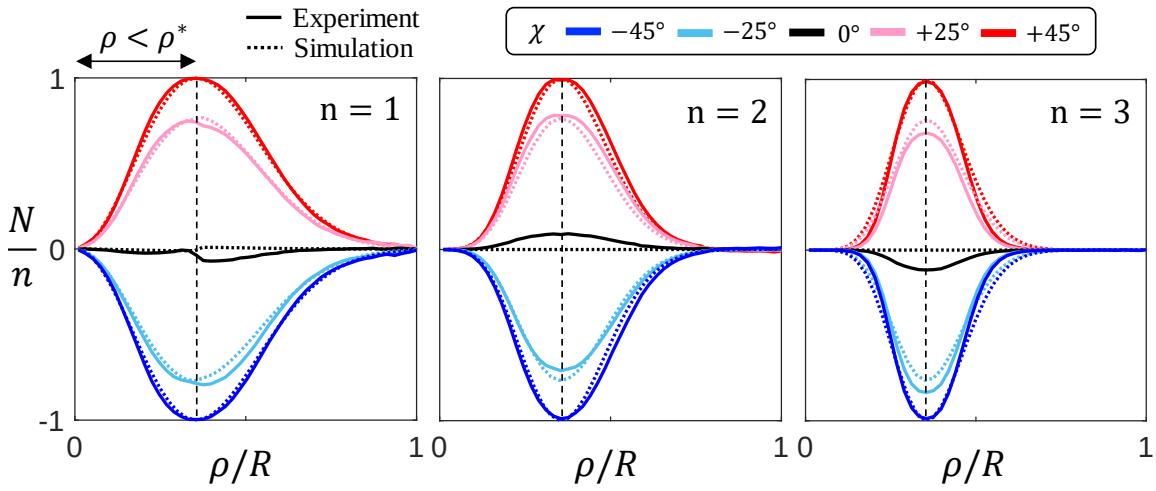

Figure 3.9 Quantitative assessment of the Skyrme number over a disk of radius ρ for the five incident polarization states and $n = (1, 2, 3)$ according to Eq. (3.9).

and right-handed ($\chi_{\text{in}} = -45°$) circular polarization states. The dashed circles refer to the disk of radius ρ^* that defines a nth-order skyrmion of charge $N^* = \sigma n$ for an incident helicity σ. The experimental Skyrme density, which tells how the Stokes vector field paves the Poincaré sphere is shown in Fig. 3.7(c) for $n = 1, 2, 3$ skyrmionic waveplates and above-mentioned input polarization states. The corresponding simulations illustrated in Fig 3.8 show a strong agreement with the experimental data.

These results demonstrate the generation of nth-order optical skyrmions with Skyrme number $N^* = \sigma n$ in the central part of the output beam defined as a disk of radius ρ^*. This is quantitatively assessed in Fig. 3.9 where the dependence of the Skyrme number inside a disk of radius ρ is shown for the five incident polarization states and $n = (1, 2, 3)$ according to the Eq. (3.9). In addition, the Skyrme number associated with the outer part of the disk with radius ρ^* satisfies $\overline{N}(\rho^*) = -N(\rho^*)$ as $N(R) \to 0$ for all n, see Fig. 3.9.

3.2.4 Management of experimental Stokes measurements

Experimentally, although we deal with fully polarized laser fields, the experimentally measured value $|\mathbf{s}_{\text{exp}}| = \sqrt{s_1^2 + s_2^2 + s_3^2}$ is not ideally constant, see Fig. 3.10. On top of that, the calculation of Skyrme number involves gradients of Stokes vectors which are highly susceptible to noise, especially in regions of low intensity, such as at large radial distances or near singularities, where the spatial derivatives of fluctuating noise can dominate the signal. We emphasize that all shown Skyrmionic textures are obtained without applying any noise filtering, though renormalizing of the experimental data

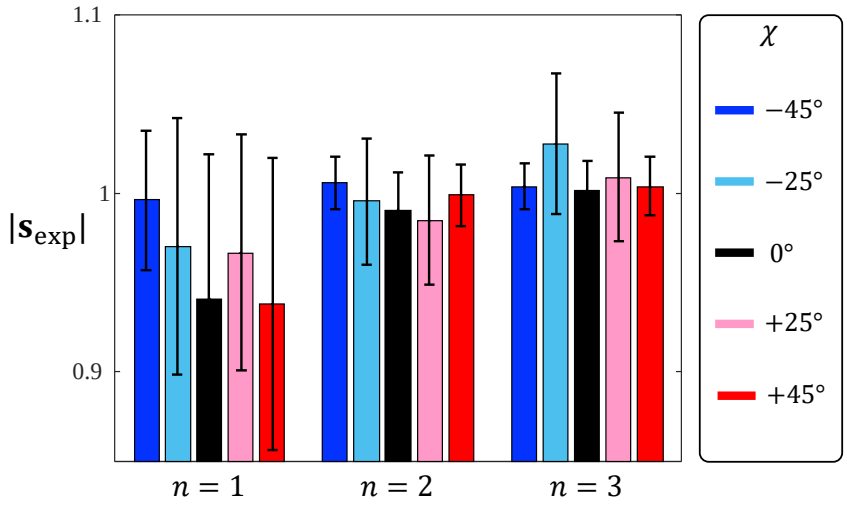

Figure 3.10 Experimental assessment of the level of deviation to ideal measurements for which one expects $|\mathbf{s}_{exp}| = 1$. Here the data corresponds to $|\mathbf{s}_{exp}| = \langle|\mathbf{s}_{exp}|\rangle \pm \mathrm{std}(|\mathbf{s}_{exp}|)$ over the area of the spin-orbit waveplates of order $n = (1, 2, 3)$ for the five incident polarization states.

according to $\mathbf{s} \to \bar{\mathbf{s}} = \mathbf{s}/|\mathbf{s}_{exp}|$, in order to take into account the nonideally constant norm of $\mathbf{s}_{exp}$. It is important to also note that the experimental Skyrme density maps shown in 3.7(c) are produced using a low-pass Fourier filter. However, the experimental curves $N(\rho)$ (Fig. 3.9) are relatively insensitive to this denoising process, so they are presented only taking into account the renormalization.

To address those effects quantitatively, we evaluate the Skyrme number using three approaches: without renormalization, with renormalization, and with noise filtering

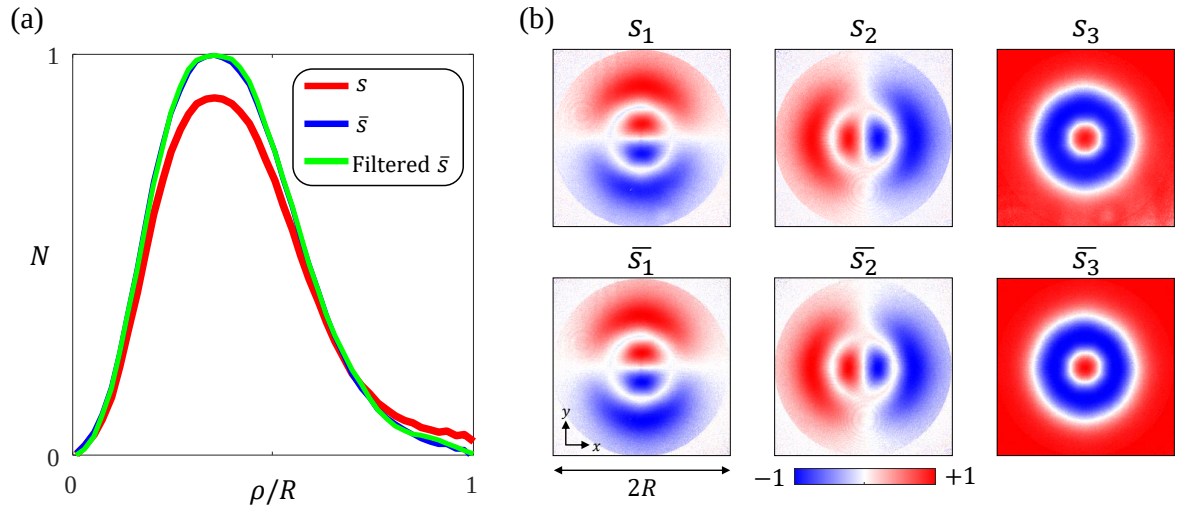

Figure 3.11 (a) Evaluation of Skyrme number over a disk of radius ρ with tree approaches. Red: without renormalization. Blue: with renormalization. Green: Applying Fourier filtering to the renormalized Stokes vectors. (b) Reduced Stokes parameters $(\mathbf{s}_1, \mathbf{s}_2, \mathbf{s}_3)$ and renormalized ones $(\bar{\mathbf{s}_1}, \bar{\mathbf{s}_2}, \bar{\mathbf{s}_3})$ according to $\bar{\mathbf{s}} = \mathbf{s}/|\mathbf{s}_{exp}|$. The results are shown for left-handed circularly polarized incident light and $n = 1$ waveplate, as an example.

applied to the renormalized Stokes vectors. The effect of renormalization and filtering on the calculation of Skyrme number is shown in Fig. 3.11(a), as an example taken $n = 1$ skyrmionic waveplate and in the case of left-handed circularly polarized incident light. We note that the renormalization leads to an expected increase in Skyrme number. In addition, it smoothens the experimental data as is shown in Fig. 3.11(b), while the Skyrme number is almost unchanged when noise filtering is applied. Thus, we use renormalized reduced Stokes vectors for further study.

3.2.5 Propagation of the central skyrmion

Here we report on the evaluation of the central optical skyrmion enclosed in the disk of radius ρ^* as a function of the propagation distance. This is done by determining experimentally the Stokes texture and the Skyrme density maps as a function of the propagation distance z for a circularly polarized incident beam with 1.5 mm beam waist at the sample plane. In practice, we evaluate $N(\rho)$ at the output of the skyrmionic waveplates ($z = 0$) by using the setup shown in Fig. 3.7(a), after free space propagation over 1 m (intermediate field, Fresnel number $F \approx 4.2$) by placing the camera at distance 1 m from the plate, see Fig 3.12(a), and in the far field by applying the Fourier-optics

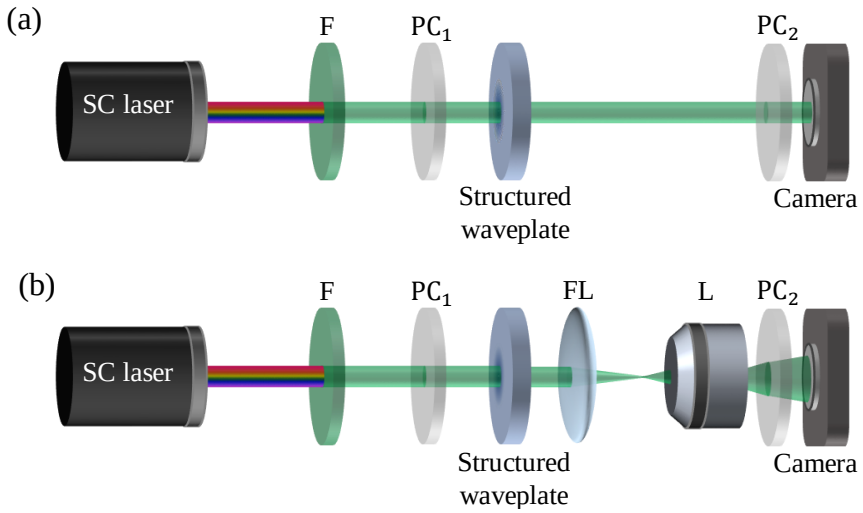

Figure 3.12 Experimental setup for full Stokes polarimetric analysis after (a) 1m of propagation of skyrmionic field and (b) in the far field. F: spectral filter for 532 nm wavelength. PC_1: polarization controller made of a linear polarizer, quarter-waveplate, and half-waveplate to achieve any arbitrary incident polarization state. PC_2: polarization controller allowing to record with the camera the intensity distribution of the output field projected on H, V, D, A, L, R polarization state. FL: Fourier lens with $f = 200$ mm focal length placed at f distance from the waveplate. L: 10× microscope objective lens with numerical aperture 0.25 to image the Fourier plane (located at $z = 2f$ from the waveplate) of the skyrmionic waveplate.

conjugation. The latter is achieved by placing a lens with focal length $f = 200$ mm at a distance $z = f$ from the waveplate and imaging the plane located at $z = 2f$ by a 10× microscope objective with numerical aperture 0.25 in order to properly resolve the Stokes texture on a camera, see Fig 3.12(b).

The corresponding experimental results for $z = (0, 1\,\mathrm{m}, \infty)$ are collected in Fig. 3.13(a), see markers, for left- and right-handed incident circular polarization state and $n = 1$. We find that the Skyrme number peaks at a value that only slightly departs from $N = \pm 1$ whatever the propagation distance, from which the radius ρ^* is identified. The corresponding experimental Stokes texture $\{\mathbf{s}\}$ and Skyrme density Σ of the skyrmion in the region $r < \rho^*$ are shown Fig. 3.13(b) and 3.13(c) respectively.

It is noteworthy to confront the experimental results with the simulated one by applying the polarization transformation to the incident field $\mathbf{E}_{\mathrm{in}} = E_0 \exp(-r^2/w^2)\,\mathbf{e}_\sigma$ by inserting Eqs. (3.6) and (3.7) in Eq. (3.5), which gives the field emerging from the structured waveplate, and then evaluating numerically the propagated field using two-dimensional Fourier propagation method, described in Chapter 2. The results are shown as the dotted curves in Fig. 3.13(a), which exhibit deviation from the experimental data, except at $z = 0$.

Qualitatively, this can be understood from the radially modulated dynamic phase profile $\Phi_{\mathrm{dyn}}(r)$ that results from the fact that the femtosecond laser processing of silica enabling on-demand 2D spatial profiles of both Ψ and Δ [49, 50] comes at the expense of average refractive index changes that depend on the level of the laser written optical anisotropy [81]. Quantitatively, this can be described with good accuracy by assuming a linear radial dependence with respect to the birefringent phase retardation, namely, $\Phi_{\mathrm{dyn}}(r) = -\epsilon\Delta(r)$. This is illustrated in Fig. 3.13(a) for various values of ϵ, see the gray color area corresponding to $0.45 \le \epsilon \le 0.85$. An overall satisfying description of the experiments is found for $\epsilon = 0.65$ as shown by the red curve for all z and summarized in Table. 3.1, where Skyrme number over a disk with radius ρ^* is presented.

	Experiment		Simulation	
	$\sigma = -1$	$\sigma = +1$	$\sigma = -1$	$\sigma = +1$
$z = 0$	-0.997	0.997	-1	1
$z = 1\,m$	-0.966	0.970	-0.950	0.950
$z = \infty$	-0.951	0.960	-0.978	0.978

Table 3.1 Summary of the experimental and simulated $\epsilon = 0.65$ values of N^* corresponding to the results collected in Fig. 3.13.

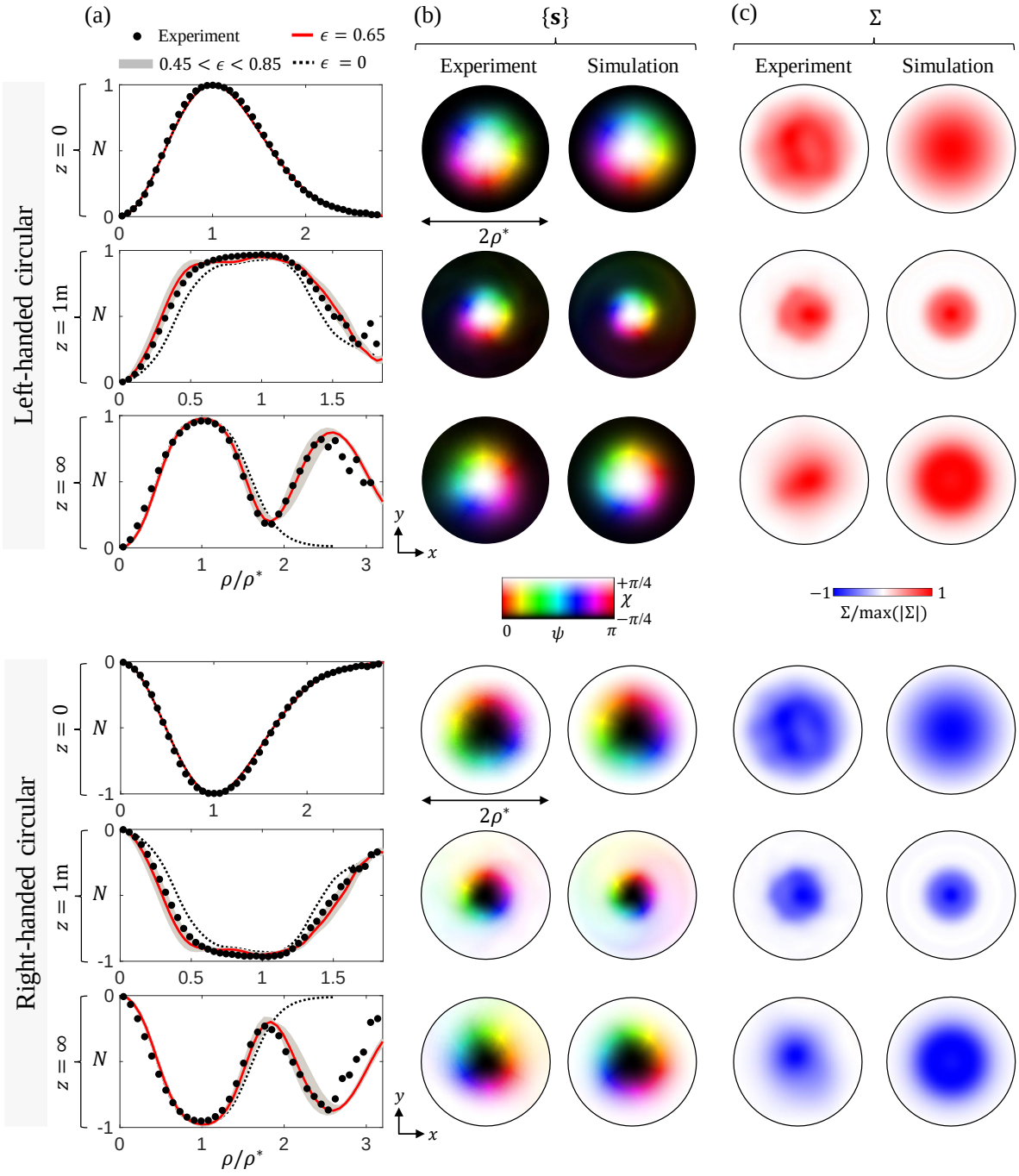

Figure 3.13 (a) Experimental (markers) and simulated (curves) $N(\rho)$ at propagation distances $z = (0, 1\,\text{m}, \infty)$ for $n = 1$ and $\chi_{\text{in}} = 45°$. The parameter ϵ refers to the ad hoc linear relationship between the birefringent phase retardation and the dynamic phase, $\Phi_{\text{dyn}}(r) = -\epsilon\Delta(r)$. Corresponding experimental and simulated (at $\epsilon = 0.65$) (b) Stokes textures $\{\mathbf{s}\}$ and (c) Skyrme density Σ maps inside the disk of radius ρ^*. The results are illustrated for both left-handed (top) and right-handed (bottom) circularly polarized incident beam.

3.2.6 Propagation of the skyrmionic field

So far, we have directed our attention to the Stokes texture inside the disk of radius ρ^*. However, for a circularly polarized incident beam, the entire field emerging from the skyrmionic waveplate contains two skyrmions nested within each other, as shown in Fig. 3.7. Although it has been shown in the previous section that the central skyrmion and the Skyrme number are subjected to only a slight deviation during its propagation, the peripheral field ($r > \rho^*$) strongly evolves.

The experimental and simulated Stokes textures of the entire beam at 1 m and in the far field are summarized in Fig. 3.14 for left-handed (top) and right-handed (bottom) circularly polarized incident beam and $n = 1, 2, 3$ waveplates. In the rightmost column of Figs. 3.14(a) and 3.14(b) we numerically consider ideal case $\epsilon = 0$. Its comparison with experimental data allows appreciating the role of the dynamic phase as the field

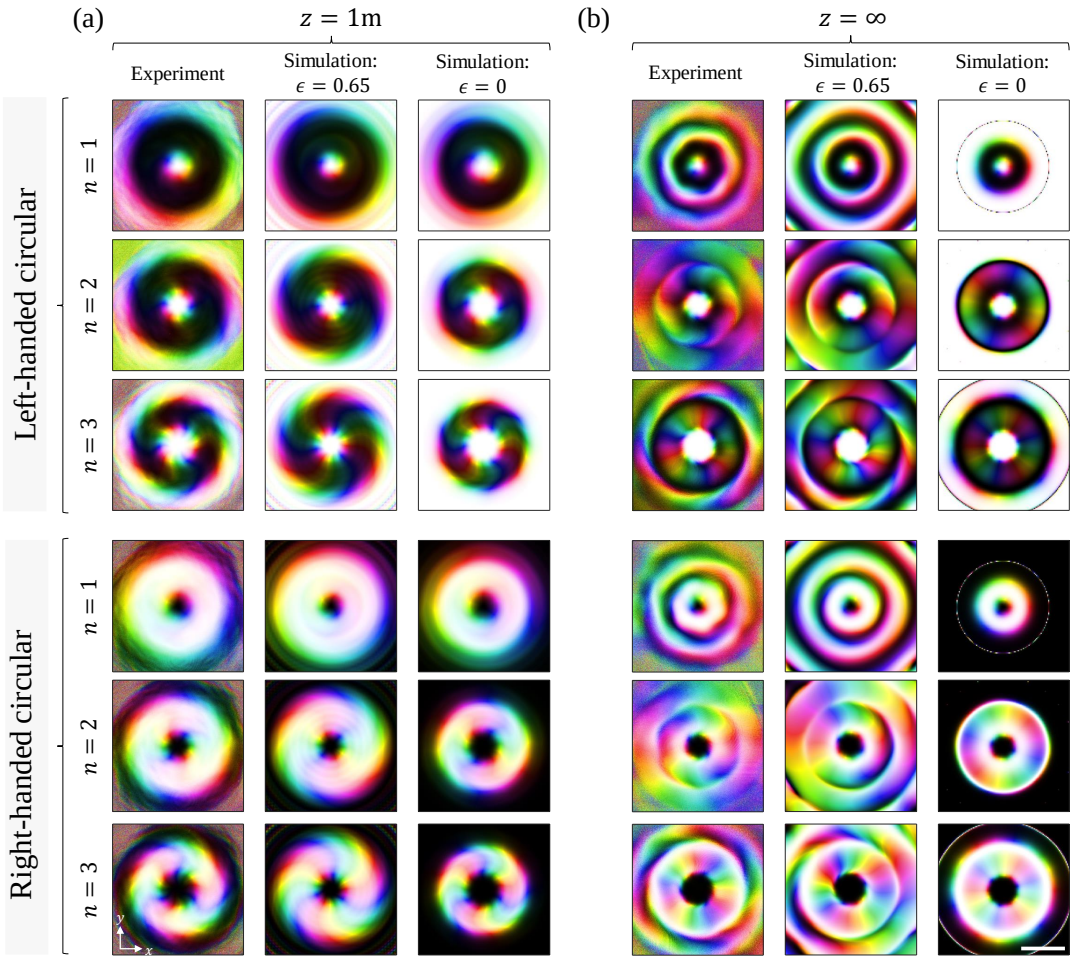

Figure 3.14 Full Stokes texture $\{\mathbf{s}\}$ at (a) $z = 1$m and (b) in the far field for left-(top) and right-(bottom) handed circularly polarized incident beam. Left column: Experiment. Middle column: simulation where $\epsilon = 0.65$. Right column: simulation where $\epsilon = 0$. Scale bar: 2 mm. See Fig. 3.1 for the colormap.

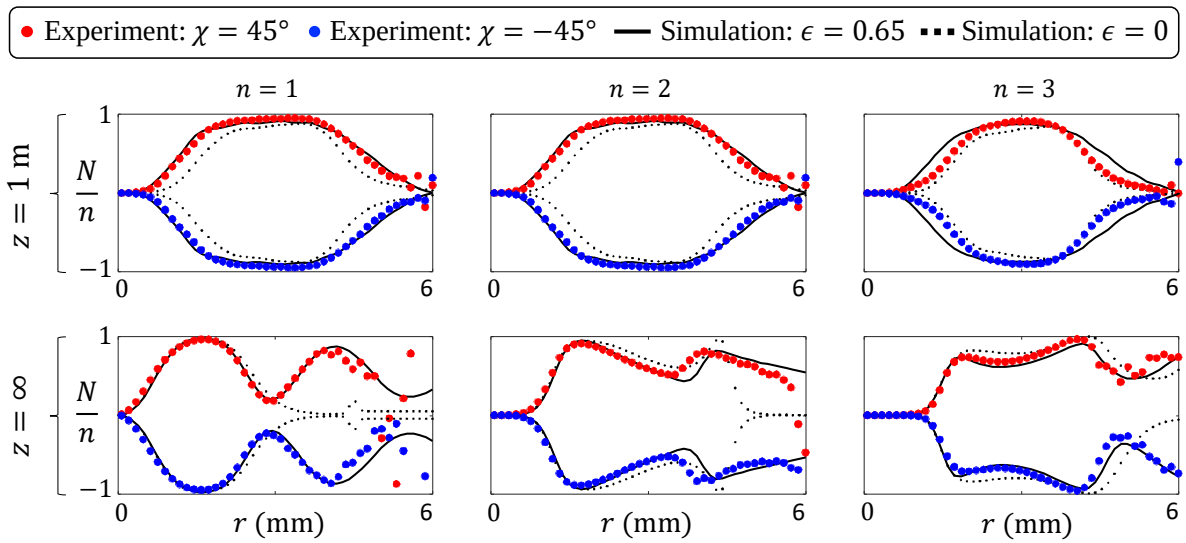

Figure 3.15 Experimentally and numerically calculated Skyrme number over a disk of radius $r \leq 6$ mm for $\chi_{\text{in}} = \pm 45°$ and $n = (1, 2, 3)$ for 1 m of propagation (top) and in far field (bottom) corresponding to the skyrmionic textures illustrated in Fig. 3.14.

propagates. We observe that the effect of a modulated dynamic phase becomes strikingly obvious at a sufficiently large propagation distance. Indeed, a ringing pattern develops after a few meters, which is illustrated in Fig. 3.14 by showcasing the far field situation. The oscillatory Stokes texture leads to the oscillation of the Skyrme number corresponding to a disk of increasing radius, shown in Fig. 3.15, after 1 m propagation and in the far field, for $n = 1, 2, 3$. This highlights that further design work is desirable to address the topological stability issue.

3.2.7 Polarization singularities and their evolution

The spin-orbit nature of the proposed topological beam shaping process allows precise vectorial field shaping by design. It provides a platform for continuously transforming vector fields in a topological manner. This is illustrated by the way the generated polarization singularities, embedded in the inhomogeneous spatial distribution of the polarization state, evolve as the incident polarization state varies from one pole of the Poincaré sphere to the other ($\chi_{\text{in}} = \pm 45°$) along a meridian ($\psi_{\text{in}} = 45°$). Considering fully polarized paraxial fields whose polarization state varies in the (x, y) plane, we deal here with two types of generic polarization singularities in the output field that are structurally stable upon perturbation and propagation [82]. Namely, C-points where the polarization state is circular (ψ_{out} is undefined) and L-lines where the polarization state

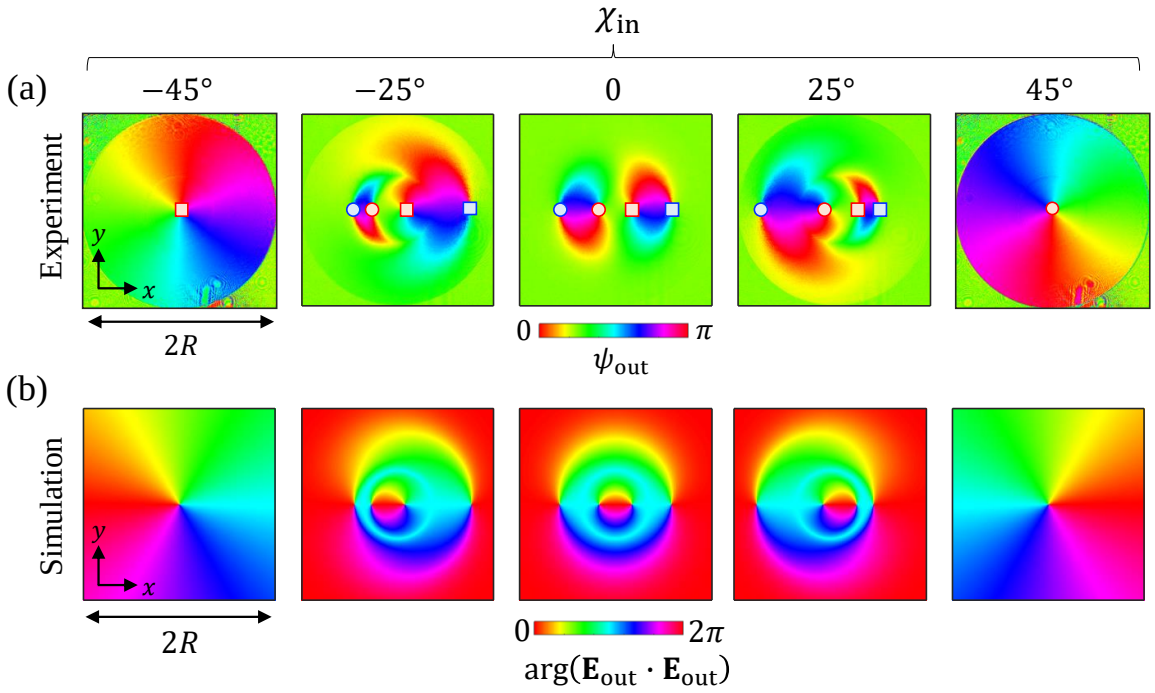

Figure 3.16 (a) Experimental polarization state azimuth ψ_{out} maps and (b) simulated $\arg(\mathbf{E}_{out} \cdot \mathbf{E}_{out})$ maps for the five values of χ_{in} and $n = 1$ skyrmionic waveplate where $\psi_{in} = 45°$.

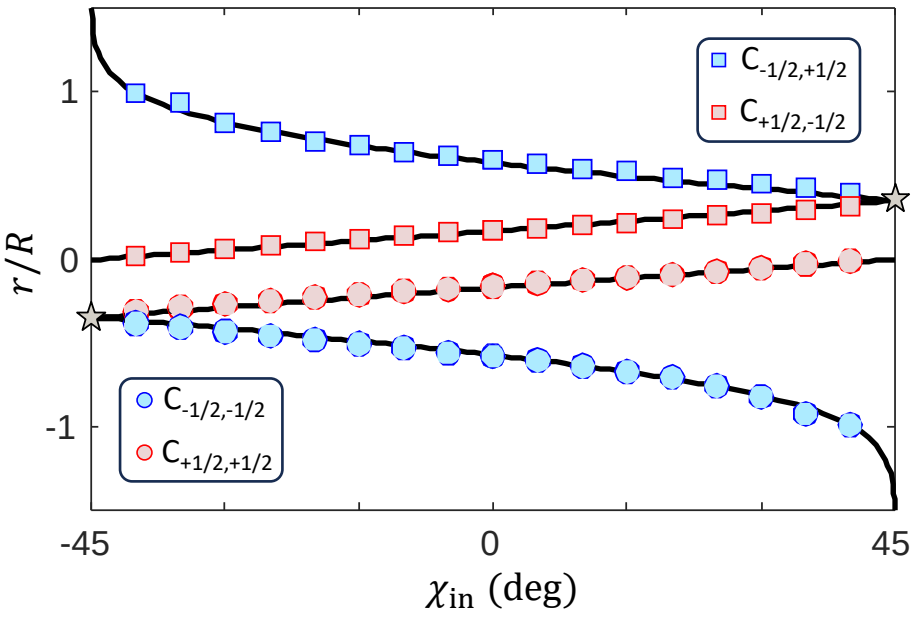

Figure 3.17 Experimental (markers) and simulated (solid curves) trajectories in the transverse plane of the various C-points labeled C_{m_1,m_2} (see text for definitions) as a function of χ_{in} for $\psi_{in} = 45°$ and $n = 1$. The star markers refer to creation and annihilation events.

is linear (the sign of χ_{out}, i.e., the handedness of the polarization state, is undefined), and here we will focus on C-points. The latter are experimentally identified as singularities in the real scalar field ψ_{out} while they can be numerically traced from phase singularities in the complex scalar field $\Phi = \mathbf{E}_{out} \cdot \mathbf{E}_{out}$ [83]. In turn, generic C-points can be characterized by two half-integer topological numbers [84]: the signed number of turns of the major axis of the polarization ellipse along a closed contour containing the C-point, m_1, and half the topological charge of the corresponding phase singularity in the field Φ, m_2. The identification of C-points are illustrated in Fig. 3.16 for $\chi_{in} = 0, \pm 25°, \pm 45°$ and fixed $\psi_{in} = 45°$ for the skyrmionic waveplate with $n = 1$. We observe that the topological transformation of the optical skyrmion inside the disk of radius ρ^* from the Skyrme number $N = \pm n$ to $N = \mp n$ along a meridian on the Poincaré sphere involves the creation/annihilation events of pairs of C-points with opposite pairs of topological numbers $\pm(m_1, m_2)$ at finite distance from the z axis, as well as the emergence/disappearance of C-points at infinity, as shown in Fig. 3.17.

The generalization to high-order waveplates with $n = 2$ and $n = 3$ is shown in Fig. 3.18, which highlights the nongeneric character of on-axis C-points. Meaning that for $\chi_{in} = \pm 45°$ when $n > 1$, the nongeneric C-point characterized by $(m_1, m_2) = (n/2, \pm n/2)$ splits into n generic C-points characterized by $(m_1, m_2) = (1/2, \pm 1/2)$ as the incident polariza-

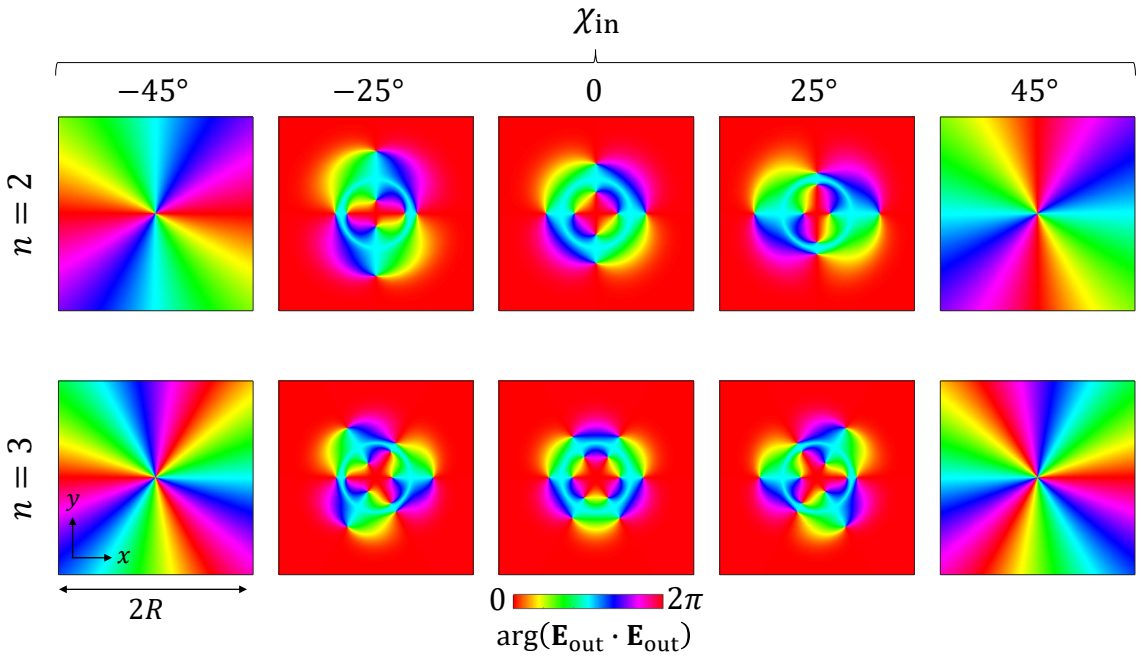

Figure 3.18 Simulated maps of $\arg(\mathbf{E}_{out} \cdot \mathbf{E}_{out})$ for the five values of χ_{in} and $n = 2, 3$ skyrmionic waveplates where $\psi_{in} = 45°$.

tion states departs from being circular. Beyond its fundamental interest from a singular optics point of view, such remote control of polarization singularities in skyrmionic optical fields provides alternative means for contactless optical manipulation of objects experiencing inhomogeneous force and torque fields, analogous to the recent demonstration using topological water-wave structures [85].

3.2.8 Concluding remarks

The possible realization of compact and robust single-stage spin-orbit topological optical elements producing skyrmionic beams from Gaussian beams has been discussed and a first experimental attempt has been reported. By demonstrating how inhomogeneous anisotropic media can serve the advent of skyrmionic photonics, the present results highlight the advantage to be gained by extending the usual designs of metasurfaces such as q-plates [86] and J-plates [87] to spatially varying retardance profiles. In addition, the laser machining technology used here, which combines the realization of macroscopic clear aperture devices (in this case on the order of centimeters) with arbitrary patterns for retardance and orientation of the optical axis [49, 50], makes this a user-friendly technological approach. Once combined with the possible generation of polarization-controlled topological features, we expect it to be useful for the development of optical communication protocols [78]. Finally, we emphasize that the present results are equally applicable to the near-infrared, thermal infrared, terahertz, and microwave domains, with as many potential applications in nanophotonics, optical communications, and biomedical imaging, to name a few. Beyond classical optics, the present approach of developing spin-orbit skyrmionic waveplates could also serve as novel platforms for quantum optics experiments that have begun to involve skyrmions [88].

Still, as previously implied, the reported results should be viewed as a first step towards the development of a novel class of topological spin-orbit photonic devices. In the next section, we propose an alternative approach allowing to obtain localized skyrmion embedded in a uniform polarization background, hence going beyond the limitations of the strategy discussed in the present section.

3.3 Q^2-plates: from optical vortex to optical skyrmion

3.3.1 Proposing an alternative design to q-plate

The waveplates presented in the preceding section provide a skyrmionic texture as a whole field with $N = 0$ topological charge regardless of the incident polarization state, as shown in Fig. 3.9. A skyrmion with topological charge $N = \sigma n$ is generated for incident polarization states $\sigma = \pm 1$ only in the central part of the beam, within a disc of radius ρ^*, where $\Delta(\rho^*) = \pi$. In order to have a skyrmion as a whole beam, an option is to provide a uniform birefringence phase retardation for $r > \rho^*$, which contrasts with the skyrmionic waveplates, where $\Delta \to 0$ as $r \to R$, see Fig. 3.19(a).

To this aim, here we propose a design restricting ourselves to linear functions for both slow axis orientation $\Psi(\phi)$ and birefringence phase retardation $\Delta(r)$:

$$\Psi = q\phi \tag{3.10}$$

$$\Delta = 2\pi q'(r/\rho^*), \text{ if } r < \rho^*, \text{ else } \Delta = 2\pi q', \tag{3.11}$$

where q' can be read as a second winding number of a radial nature that adds to the azimuthal winding number q of the doubly inhomogeneous waveplates. We will further refer to such elements as q^2-plates, in tribute to the q-plate terminology that is widely adopted in the optics and photonics community. This proposal can be considered as a

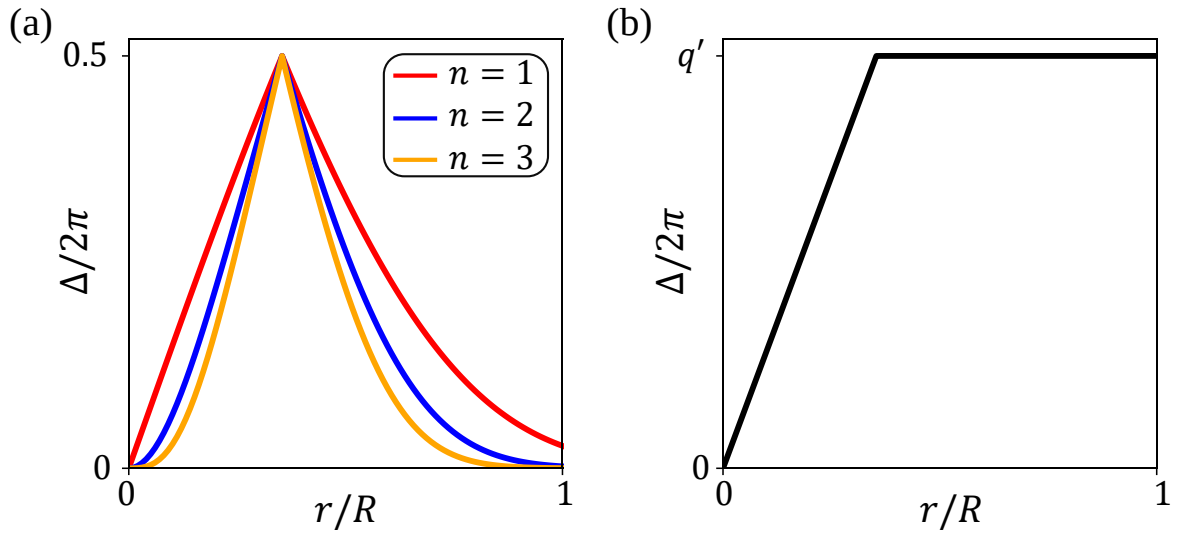

Figure 3.19 Analytical birefringent phase retardation Δ radial profiles of (a) $n = 1, 2, 3$ skyrmionic waveplates and (b) q^2-plate with q' radial winding number.

generalization of the q-plate since the second winding number q' is associated with the radial degrees of freedom, whereas the q-plate is limited to a single winding number q associated with the azimuthal degree of freedom. This "second quantization" acts not only on a different spatial degree of freedom, but also on a different property of the anisotropic medium.

3.3.2 Characterization of the plates

Two types of q^2-plates designed for $(q, q') = (1/2, 1/2)$ and $(q, q') = (1, 1/2)$ have been fabricated by femtosecond-laser nanostructuring on a silica glass substrate according to the Eqs. (3.10) and (3.11), with ρ^* =1 mm, and whose structural footprint corresponds to a disk of radius 3 mm. The experimental characterization was carried out by spatially resolved polarimetry (discussed in Chaper 2 and previous section) and summarized in Fig. 3.20. The doubly inhomogeneous structure of such waveplates is combined in a single map as illustrated in Fig. 3.20(a) where the optical axis orientation Ψ is presented by color and the brightness refers to the phase retardation Δ. Quantitative characterization of the plates is demonstrated in Figs. 3.20(b) and 3.20(c), showing the azimuthal de-

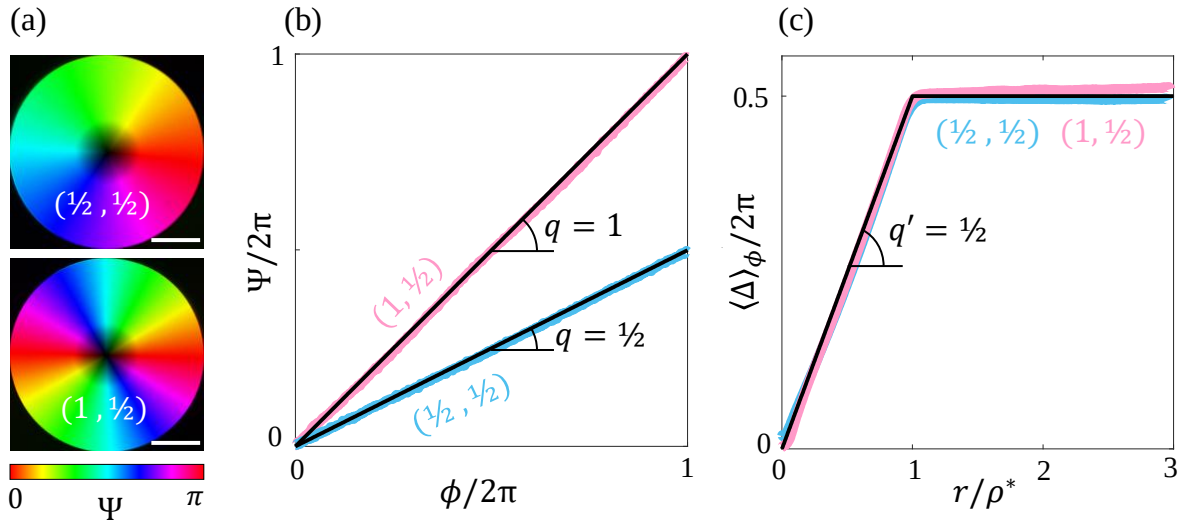

Figure 3.20 Optical characterization of q^2-plates with $(q, q') = (1/2, 1/2)$ and $(q, q') = (1, 1/2)$ designed with ρ^* =1 mm, and whose structural footprint corresponds to a disk of radius 3 mm. (a) Combined image of the birefringent phase retardation and optical axis orientation, where the brightness refers to Δ/π and the hue colormap refers to Ψ. Scale bar: 1 mm. (b) Azimuthal dependence of Ψ. (c) Radial dependence of azimuthally averaged Δ. Solid black lines refer to Eqs. (3.10) and (3.11)

pendence of Ψ and radial dependence of azimuthally averaged Δ, alongside simulations based on the Eqs. (3.10) and (3.11).

These plates enable complete control over how the output polarization state wraps around the Poincaré sphere, with each point P on the sphere uniquely corresponding to a specific polarization state described by the reduced Stokes vector. This capability allows the generation of optical skyrmions characterized by the Skyrme number N, which can be determined once the Stokes vector field $\mathbf{s}$ is known.

3.3.3 Skyrmion generation and detection

Various types of skyrmions are expected when using a circularly polarized Gaussian beam with the design specified by Eqs. (3.10) and (3.11). In particular, skyrmions with polarity $\sigma = \pm 1$, order $2|q|$, and Skyrme number $N = 2\sigma q$ for $q' = 1/2$ as is the case in this study.

Experimentally, the generation of optical skyrmions is demonstrated in a configuration that corresponds to common tabletop optical experiments involving laser beams. Namely, we use a 532 nm fundamental Gaussian beam with 1.5 mm incident waist radius and we resolve the spatial texture of the Stokes vector field $\mathbf{s}$ after propagation distances of the order of a meter from the q^2-plate as depicted in Fig. 3.21(a). This is done by recording the intensity profiles of H, V, D, A, L, and R components of the output field using a polarization controller, which gives access to the Stokes maps $\mathbf{s}(x, y)$. The camera is placed at a distance $D = 1.2$ m from the q^2-plate. An optional relay lens (RL) with focal length $f = 30$ cm is placed at the mid-distance between the q^2-plate and the camera. The results of Stokes texture are illustrated in Fig. 3.21(b) with and without the presence of a relay lens for the two possible incident circular polarization states ($\chi_{\text{in}} = \pm 45°$, i.i., $\sigma = \pm 1$). We observe that the Stokes texture is rotated by 180° when a relay lens is used. This rotation occurs because the lens flips the image, thereby inverting the orientation of the polarization pattern. In all cases, first- and second-order skyrmions are recovered quantitatively, and we find Skyrme numbers very close to the expected values. The corresponding Skyrme density is illustrated in Fig. 3.21(c) from which the Skyrme number is calculated according to the Eq. (3.9).

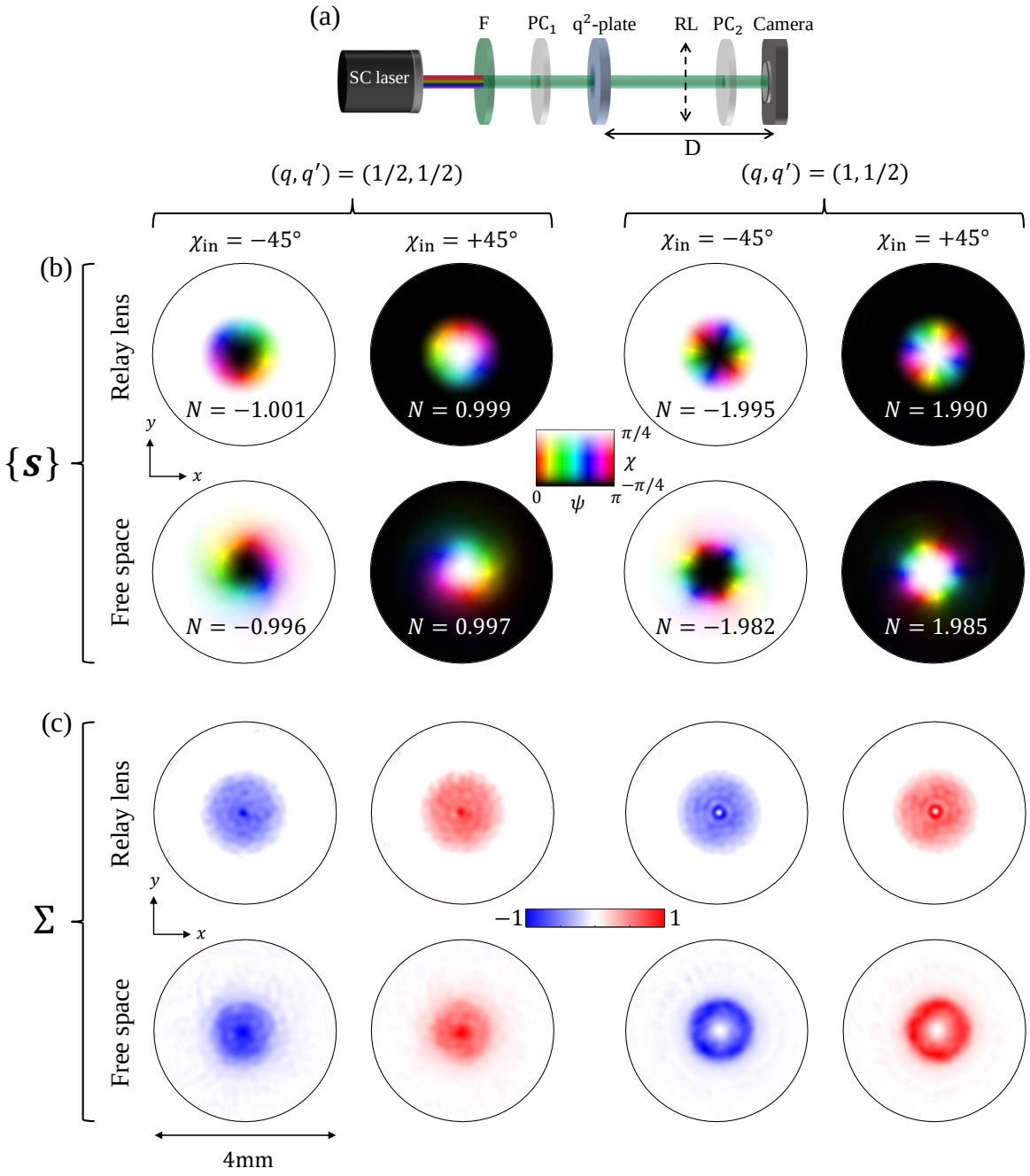

Figure 3.21 (a) Experimental setup for the observation of the generated skyrmion beam. It was used a supercontinuum laser with 1.5 mm beam waist radius and filtered by 532 nm spectral filter (F). PC_1: polarization controller made of a linear polarizer, quarter-waveplate, and half-waveplate to achieve any arbitrary incident polarization state. RL: relay lens with 30 cm focal length placed at mid-distance between the q^2-plate and the camera. PC_2: polarization controller allowing to project the intensity distribution of the output field on H, V, D, A, L, R polarization states and to record the corresponding intensity profiles with a camera placed at a distance D = 1.2 m from the q^2-plate. (b) Experimental Stokes textures $\{\mathbf{s}\}$ and (c) Skyrme density of q^2-plates with $(q, q') = (1/2, 1/2)$ and $(q, q') = (1, 1/2)$ that correspond to skyrmions with Skyrme number ideally equal to $N = 2\sigma q$, respectively and in the case of with (top) and without (bottom) the presence of the relay lens.

3.3.4 Polarization-controlled Skyrme number

Now that we have demonstrated that skyrmionic textures can be produced at the output of a q^2-plate, we recall that a key asset of a q-plate is to allow polarization-controlled orbital angular momentum content of a light beam. When using q^2-plates instead, such an asset is translated into the possible control of the Skyrme number by means of adjusting the incident polarization state. The experimental demonstration is reported in Fig. 3.22.

Experimentally we have calculated the Skyrme number over a disk of radius r for multiple values of the third Stokes vector s_3^{in} and fixed incident polarization state azimuth $\psi_{\text{in}} = 45°$ in a case of $(q, q') = (1/2, 1/2)$. The results are presented in Fig. 3.22(a) illustrating the outcomes both with and without the use of a relay lens. Then, the mean value of the Skyrme number in the highlighted gray region of Fig. 3.22(a) (top: $\{1 \text{ mm} \leq r \leq 2 \text{ mm}\}$ and bottom: $\{1.5 \text{ mm} \leq r \leq 2.5 \text{ mm}\}$) as a function of incident s_3^{in} Stokes vector is shown in Fig. 3.22(b). A linear relationship $N = 2s_3^{\text{in}}q$ is obtained. The corresponding Stokes textures are shown in Fig. 3.23

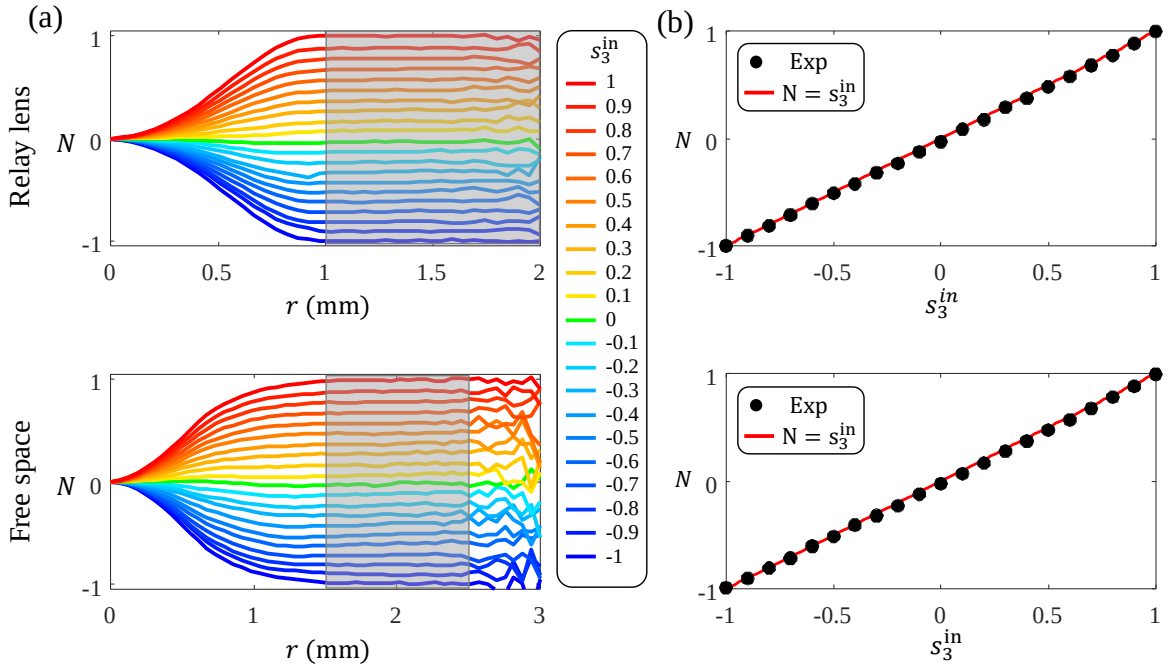

Figure 3.22 (a) Experimental Skyrme number obtained in the output field for a q^2-plate with $(q, q') = (1/2, 1/2)$ over a disk of radius r for multiple values of s_3^{in} Stokes vector and fixed $\psi_{\text{in}} = 45°$. (b) The mean value of Skyrme number over the gray region (black data points) as a function of s_3^{in} with $N = s_3^{\text{in}}$ linear relationship (red curve). Both cases, with (top) and without (bottom) relay lens, are shown.

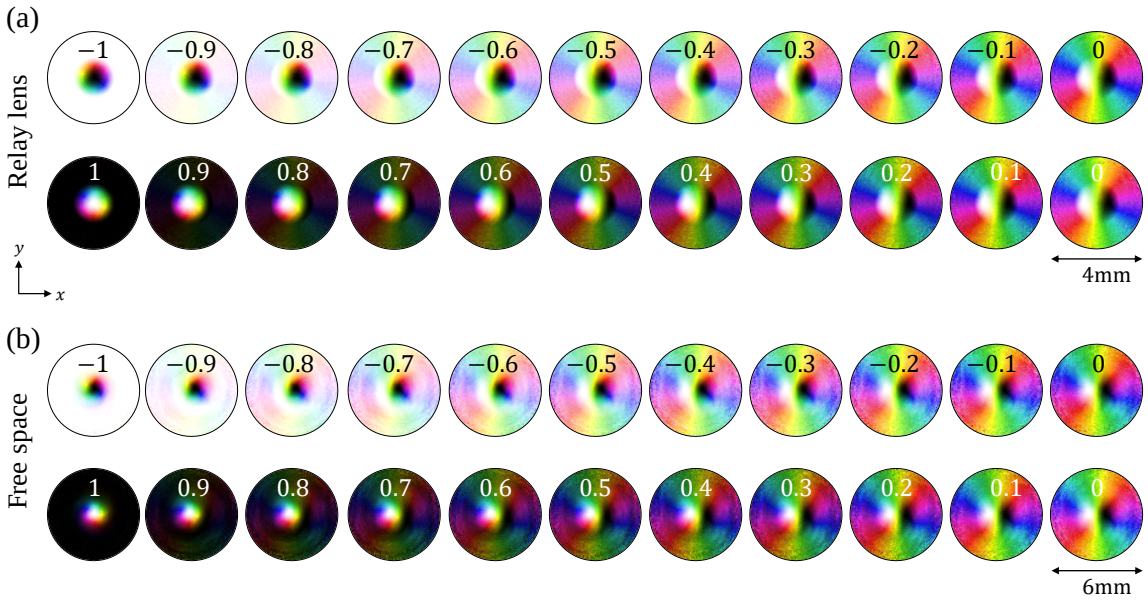

Figure 3.23 Experimentally retrieved Stokes textures with (a) and without (b) the relay lens for a q^2-plate with $(q, q') = (1/2, 1/2)$, using a fixed incident polarization state azimuth $\psi_{\text{in}} = 45°$. The numbers in the panels indicate the value of s_3^{in}. See Fig. 3.1 for the colormap.

Other types of optical skyrmions [66] can be obtained for $q' \neq 1/2$. For instance, when the incident beam is circularly polarized with helicity σ: (i) meron beams with polarity $\sigma = \pm 1$, order $2|q|$, and Skyrme number $N = \sigma q$ are expected for $q' = 1/4$, (ii) skyrmionium beams with polarity $\sigma = \pm 1$, order $2|q|$, and Skyrme number $N = 0$ are expected for $q' = 1$, and (iii) target skyrmion beams with polarity $\sigma = \pm 1$, order $2|q|$, and Skyrme number $N = 0$ or $N = \sigma$ are expected for integer or half-integer q', respectively.

3.4 Cascading q^2-plates

As mentioned in the conclusion of the previous section, a rich portfolio of skyrmionic textures can be obtained by changing the design of the plates. However, it is noteworthy that this can also be done using a limited number of q^2-plates of the same type, by cascading them in series. For the sake of illustration, we consider a circularly polarized incident light beam $\mathbf{E}_{\text{in}} = E_{\text{in}}\mathbf{e}_\sigma$ passing through m identical q^2-plates placed in series. Then, let us construct the Jones matrix $\hat{\mathbf{Q}}_{\text{eff}}$ associated to such a sequence of q^2-plates. It starts with the definition of the Jones matrix of a single q^2-plate $\hat{\mathbf{Q}}$,

$$\hat{\mathbf{Q}} = \begin{pmatrix} \cos(\Delta/2) + i\sin(\Delta/2)\cos(2\Psi) & i\sin(\Delta/2)\sin(2\Psi) \\ i\sin(\Delta)/2\sin(2\Psi) & \cos(\Delta/2) - i\sin(\Delta/2)\cos(2\Psi) \end{pmatrix} \tag{3.12}$$

where Δ and Ψ are defined in Eqs. (3.11) and (3.10). The effective Jones matrix is therefore

$$\hat{\mathbf{Q}}_{\text{eff}} = \hat{\mathbf{Q}}^{m} \tag{3.13}$$

Performing the analytical calculation we find that cascading m identical q²-plates leads to an effective q^2_{eff}-plate characterized by

$$q_{\text{eff}} = q \tag{3.14}$$

$$q'_{\text{eff}} = mq' \tag{3.15}$$

Therefore, one can obtain $m\pi$-skyrmions with Skyrme number $N = 0$ or $N = \sigma$ for even and odd numbers of m, respectively, as illustrated in Fig. 3.24 for $\sigma = +1$. In fact, one can imagine any kind of combination using not only q²-plates but also homogeneous or inhomogeneous waveplates with arbitrary retardance, which can be tested by iterating the single-stage spin-orbit optical process described by Eq. (3.5), and performing Jones calculus.

Without going into the zoology of possible options, we just illustrate with a couple of examples how powerful the principle of placing elements in series can be. First, we show that inserting a half-waveplate between two successive q²-plates of the same type allows generating multiskyrmions as shown in Fig. 3.25(a). Such a combination of m q²-plates with $m-1$ half-waveplates leads to the production of m individual skyrmions that are copies of the skyrmions generated by a single q²-plate. Such linear arrays of multiskyrmions are similar to those produced in a recent work by Shen *et al.* dealing

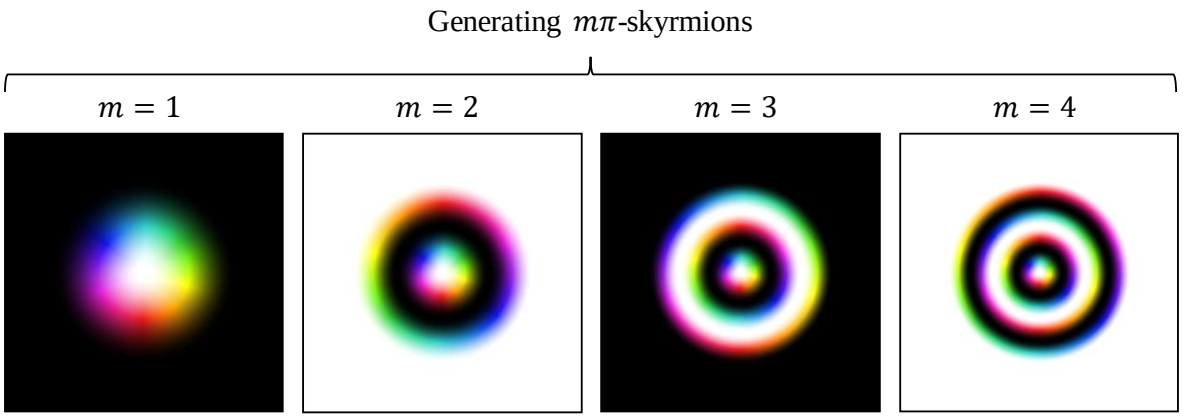

Figure 3.24 Numerical simulation of the output Stokes vector textures in the (x, y) plane when cascading in series m q²-plates with $(q, q') = (1/2, 1/2)$. The incident beam is left-handed circularly polarized. The box size is $2w \times 2w$. See Fig. 3.1 for the colormap.

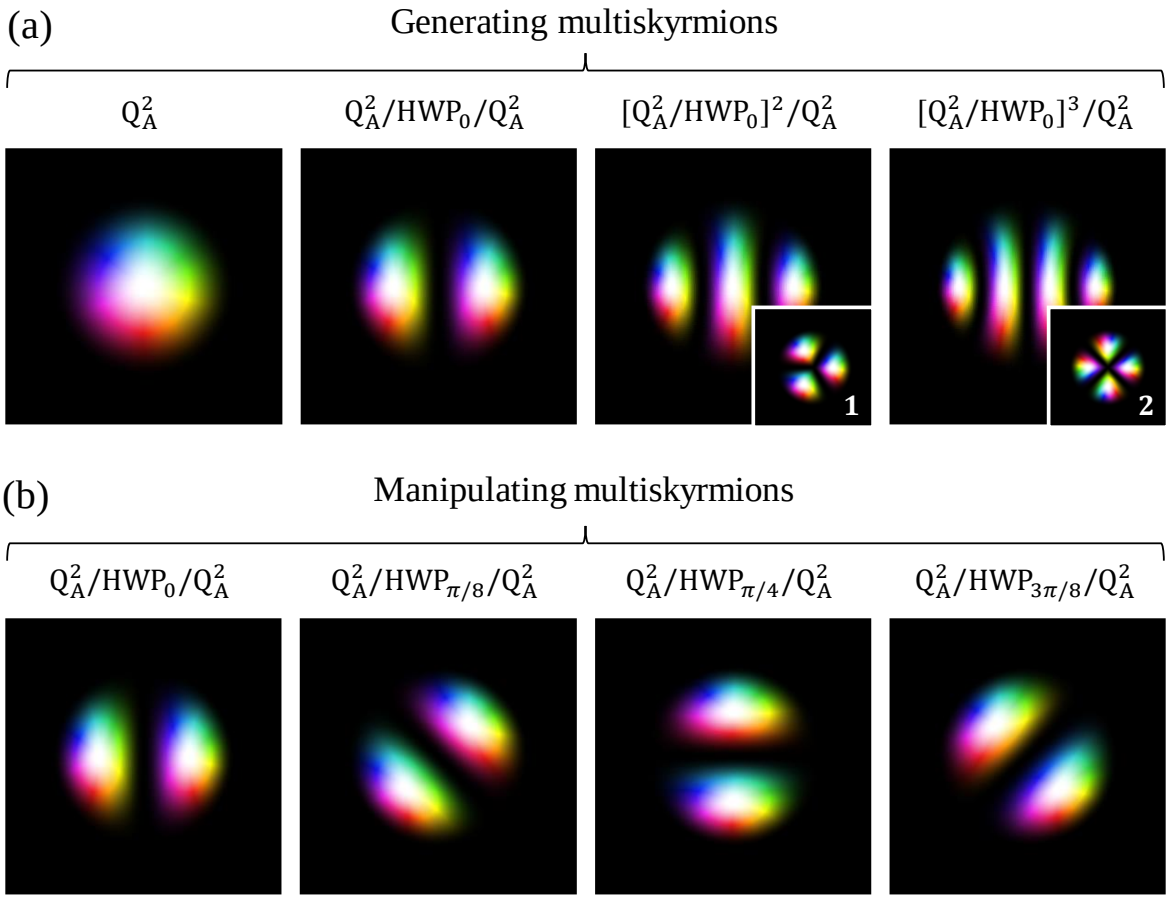

Figure 3.25 Numerical simulation of the Stokes vector textures in the (x, y) plane when cascading q^2-plates with HWP in between. The indices A and B respectively refer to (q, q') = $(1/2, 1/2)$ and (q, q') = $(1, 1/2)$, and HWP_θ refers to half-waveplate having its slow axis oriented at an angle θ from the x axis. Inset 1: the sequence of elements is $Q_B^2/\mathrm{HWP}_0/Q_A^2$. Inset 2: the sequence of elements is $Q_B^2/\mathrm{HWP}_0/Q_B^2$. The box size is $2w \times 2w$ except for the panels referring to the cascading schemes $[Q_A^2/\mathrm{HWP}_0]^2/Q_A^2$ and $[Q_A^2/\mathrm{HWP}_0]^3/Q_A^2$, for which it is $w \times w$. See Fig. 3.1 for the colormap.

with gradient-index lenses [89], though here the structured optical elements are compact and robust waveplates instead of several centimeter-long fragile devices. Circular arrays can also be obtained by replacing one or many of the q^2-plate as illustrated in the insets of Fig. 3.25(a). Second, we show that multiskyrmions can be manipulated by rotating the HWP around the beam propagation direction, see Fig. 3.25(b).

The experimental demonstration of cascading is performed using two (q, q') = $(1/2, 1/2)$ plates. As illustrated in Fig. 3.26, two q^2-plates arranged in series generate a skyrmionium, while placing an HWP between them enables the formation of a multiskyrmion. We further demonstrate the manipulation of the multiskyrmion by rotating the HWP, as depicted in Fig. 3.26 for $\theta = 0, \pi/8, \pi/4, 3\pi/8$.

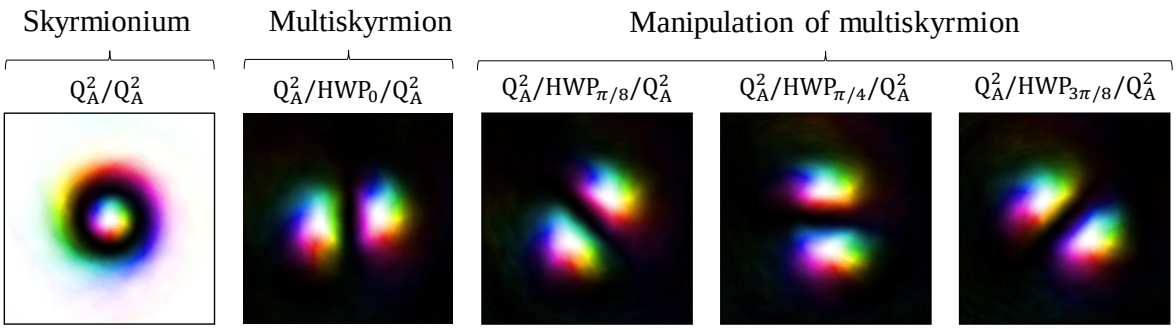

Figure 3.26 Experimental output Stokes textures in the (x, y) plane when cascading in series n q^2-plates with $(q, q') = (1/2, 1/2)$, and with HWP in between. The data is recorded after 50 cm-long free propagation from the sample. The incident beam is left-handed circularly polarized. The box size is $2w \times 2w$. See Fig. 3.1 for the colormap.

3.5 Concluding remarks

An important property of optical skyrmions is the stability of their topological structure without perturbations, which presents some limitations in the present case that should not be eluded. Indeed, the Stokes textures evolve during free space propagation even though the evolution is not substantial after meter-long propagation distances when using an incident laser beam with a millimeter-size beam waist, as reported in Fig. 3.7(c). This is experimentally illustrated by retrieving the Stokes vector in the far field. This is done by using a Fourier lens with focal length $f = 15$ cm placed at a distance f from the q^2-plate and performing spatially resolved polarimetric analysis in the plane located at a distance f from the lens, which corresponds to the reciprocal space. Then the "truncated" Skyrme number $N(\kappa)$ is calculated over a disk with radius κ centered on the beam propagation axis, as a function of κ,

$$N(\kappa) = \frac{1}{4\pi} \iint_{\sqrt{\kappa_x^2+\kappa_y^2}<\kappa} \mathbf{s} \cdot \left(\frac{\partial \mathbf{s}}{\partial \kappa_x} \times \frac{\partial \mathbf{s}}{\partial \kappa_y} \right) d\kappa_x d\kappa_y. \tag{3.16}$$

The experimental results are shown in Fig. 3.27(a) for $(q, q') = (1/2, 1/2)$ and $\chi_{\text{in}} = \pm 45°$ (i.e., $\sigma = \pm 1$), and compared with numerical simulations in two situations. First, accounting for the radial modulation of the dynamic phase prefactor $\exp(-i\epsilon\Delta)$ in the right-hand side of Eq. (3.5) associated with the inevitable change in the average refractive index of glass when artificial birefringence is encoded by laser nanostructuring [81], using the optimal parameter $\epsilon = 0.65$ obtained in Sec. 3.2.5 of the present chapter. Second, assuming that an effective compensation strategy has been developed ($\epsilon = 0$).

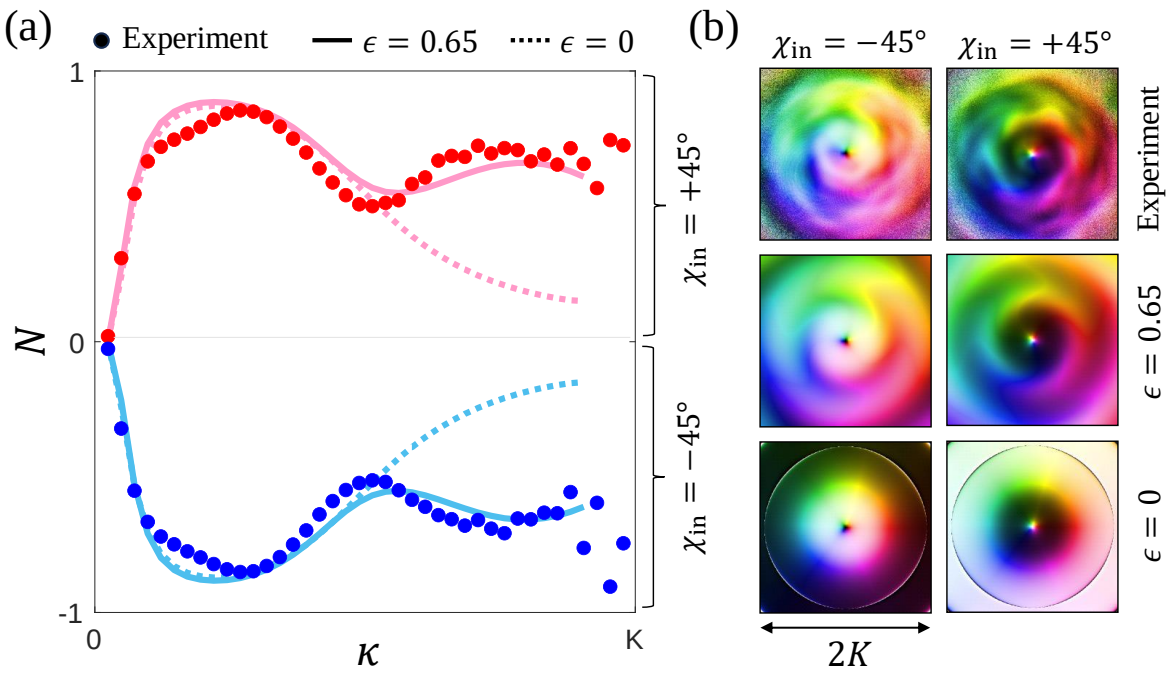

Figure 3.27 (a) Skyrme number over a disk of increasing radius in the Fourier plane of the q^2-plate with $(q, q') = (1/2, 1/2)$ for right-handed and left-handed circularly polarized incident beam. (b) Corresponding experimental and simulated Stokes vector textures. See Fig. 3.1 for the colormap.

In both cases, degradation is observed, which calls for future work in order to address the question of topological stability over long propagation distances.

As we mentioned at the beginning of the chapter, here we deal only with Stokes skyrmions. We anticipate various types of skyrmions to emerge from q^2-plates once the field is further focused, especially those involving the longitudinal component of the electric field (E_z), which is already planned as a direct continuation of this work.

The proposed generalization of q-plates, which takes place in the framework of the development of spin-orbit topological photonics, thus provides a simple way to generate optical skyrmions from inhomogeneous anisotropic waveplates, whose topology can be controlled by design. Notably, as is the case for the structured waveplates discussed in Sec. 2.3, our approach is also distinguished by its high level of compactness compared to existing bulky strategies. Also, its concept formally applies to any wavelength. This should widely promote the development of skyrmionic beam shaping technologies and the use of optical skyrmions towards the advent of optical skyrmionics—just as q-plates have done and keep doing for optical vortices both in the classical and quantum regimes for almost two decades.

CHAPTER 4

Structured light beam shaping in spectral domain

The development of spatial light modulators now makes it possible to spatially structure different degrees of freedom of light fields, such as amplitude, phase, polarization, and spatial coherence. Adding extra degrees of freedom to all these possibilities opens up new perspectives, such as the formation of optical pulses with on-demand temporal profiles, by controlling the phase and amplitude of the frequencies that constitute optical wave packets. In particular, the combination of ultrashort pulse duration, high optical power and the orbital angular momentum of light is a typical case study in a much broader field of interest dealing with spatiotemporal laser physics [90, 91]. Early works on the generation of femtosecond vortex pulses with well-defined topological charge dates back two decades ago [92, 93], for which the main challenge was the topological charge dispersion associated with strategies based on azimuthal shaping of the dynamic phase. At that time, it was also realized that achromatic optical vortex generation can be achieved using geometric rather than dynamic phase modulation [94, 95]. The geometric phase route to the management of OAM of ultrashort pulses was then implemented soon after [96, 97]. Today, the ability to obtain vortex pulses of a few optical cycles with a fixed topological charge and increasingly high energies [98] means that spatiotemporally structured light in the attosecond regime is on the way to practical use. It is noteworthy that the development of reconfigurable spatiotemporal shaping of optical pulses basically relies on the use of *dynamic phase* spatial light modulators [99, 100]. In this chapter, we report on the possible use of *geometric phase* spatial light modulators in order to prepare spatiotemporal coupling for polychromatic light fields. Such an approach being based on the spin-orbit interaction of light, it opens a path for preparing pulses with tailored vectorial spatiotemporal properties that could be reconfigured by exploiting the polarization state of light as a control parameter, as well as external fields when dealing with liquid crystal (LC) devices as done in this chapter.

Indeed, here we propose a single liquid crystal waveplate for polychromatic light shaping and modulation of OAM in the visible domain and its envisioned use for 3D topological shaping of ultrashort optical pulses.

4.1 Tunable spin-orbit liquid crystal waveplates

4.1.1 Liquid crystal topological defects

Liquid crystals are widely used in almost all areas of modern life. They have become popular in singular optics research due to their anisotropic and inhomogeneous optical properties [101, 102]. The high birefringence and tunability indeed give opportunities to develop optical elements capable of shaping the phase, amplitude, and polarization of light. The advantage of LCs over other optical materials is that the change of their properties can be achieved either locally or nonlocally [103]. In the most common phase of LCs, the so-called nematic phase, the LC molecules tend to align parallel one to the other, with a local average orientation given by headless unit vector **n** (**n** and -**n** representing identical oriental states), as shown in Fig. 4.1 The orientational state of a nematic liquid crystal system depends on the temperature (nematic phase exists only in a limited temperature range), the boundary conditions, and the possible external fields (electric, magnetic, thermal, optical, etc) applied to it. In particular, the orientational state can be associated to topological features, which, in turn, can be transferred to light via light-matter interaction [104]. Topological defects on nematics can be of two types: singular or nonsingular. Singular topological defects are associated with locations where the order itself is not defined (i.e., **n**), while nonsingular topological defects refer to locations where the director field can be associated with well-defined winding numbers although it is continuously and smoothly defined everywhere. See Ref. 105 for a review on LC defects.

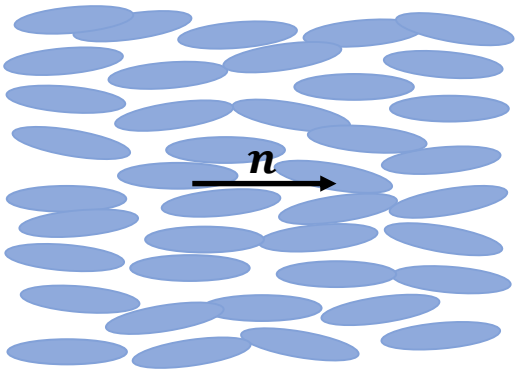

Figure 4.1 Representation of a nematic liquid crystal with the local average orientation of the molecules given by unit vector **n**.

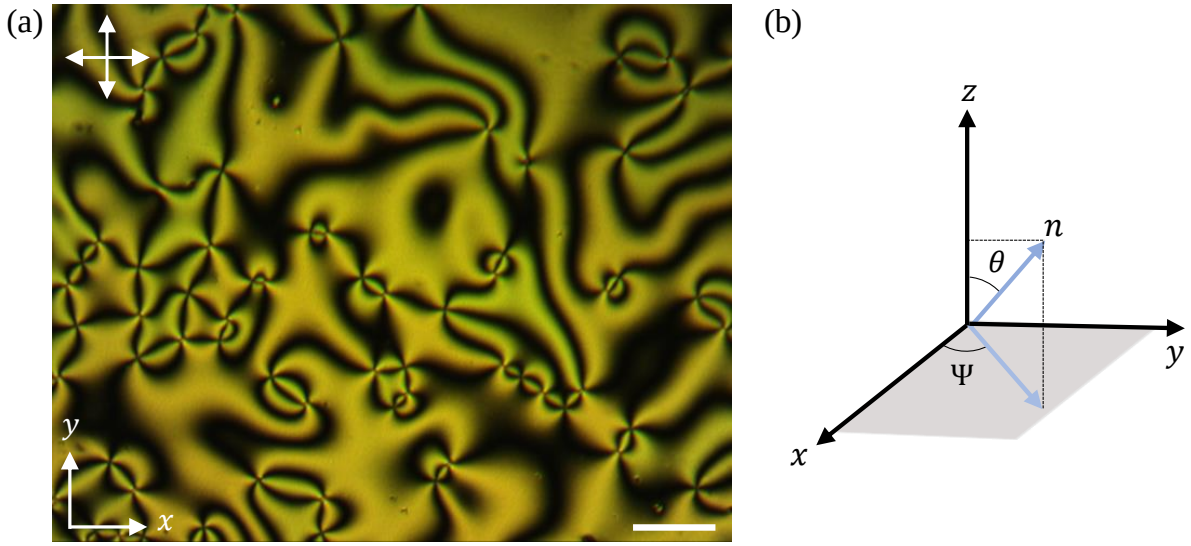

Figure 4.2 (a) Umbilical defects with topological charge $q = \pm 1$ above threshold voltage under white light illumination and between crossed linear polarizers. Scale bar: 100 μm. (b) Representation of a director $\mathbf{n}$ in x, y, z frame.

Liquid crystal topological defects have been shown since a long time to allow shaping light beams endowed with topological features, see [106–110]. Nowadays, photopatterning technology allows obtaining arbitrary space-variant 2D orientation of the director field, and commercial solutions are available. However, there is a practical tradeoff between the quality of LC structuring and the ability to control the effective birefringence of LC slab by external fields. This can be solved by exploiting spontaneous or field-generated LC defect structures as reviewed in [104]. In particular, self-engineered spin-orbit LC waveplates could be obtained by using so-called umbilical defects [111]. This kind of nonsingular 3D microscopic topological defects randomly appear in nematic liquid crystal films (with typical thickness 1-100 μm) with negative dielectric anisotropy and above electric field Fréedericksz transition threshold voltage (U_F) that have tunable features with uniform electric field alone [109,110]. As an example, randomly distributed umbilical defects under white light illumination and between crossed linear polarizers are shown in Fig. 4.2(a).

The director orientation of umbilics can be represented in (x, y, z) laboratory frame as a continuous director field described with two space-dependent angles (θ and Ψ)

$$\mathbf{n} = (\sin\vartheta\cos\Psi, \sin\vartheta\sin\Psi, \cos\vartheta)\,, \tag{4.1}$$

where Ψ is the director azimuthal angle in the (x, y) transverse plane and ϑ is the director tilt with respect to the z axis, see Fig. 4.2(b). The 3D structure of the director

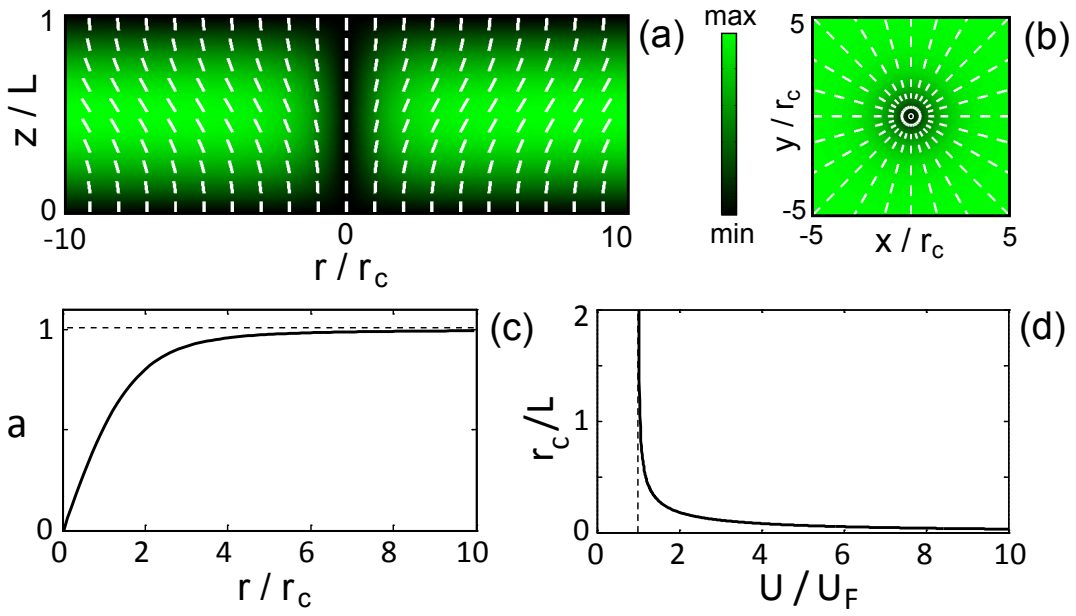

Figure 4.3 Typical meridional (a) and equatorial (b) cross sections of the director field of a $q = +1$ umbilic. r_c is the core radius of the defect and L is the nematic film thickness. The color scale refers to the amplitude of the transverse part of **n**. The white segments represent the local orientation of the director. (c) Calculated reduced amplitude a of the tilt angle nearby the defect located at $r = 0$. (d) Calculated reduced core r_c/L vs reduced voltage U/U_F, where U_F is the Fréedericksz threshold voltage. Image source: Ref. [110].

is depicted in Fig. 4.3(a) and 4.3(b) in the case of a $q = +1$ umbilic. Following [111], if the ϑ tilt angle is small, an isolated umbilic can be described by

$$\Psi = q\phi + \phi_0\,, \tag{4.2}$$

$$\vartheta(r,z) = \vartheta_{\max} a(r) \sin(\pi z/L)\,, \tag{4.3}$$

where r is the radial and ϕ is the polar coordinates in (x,y) plane, ϕ_0 is a constant, q is the topological charge, L is the film thickness, $0 \le a \le 1$ is the reduced tilt amplitude and $\vartheta_{\max}$ is the asymptotic value of ϑ at large r [110]. Finally, the profile of reduced tilt amplitude can be obtained from the following differential equation

$$\frac{\mathrm{d}^2 a}{\mathrm{d}\rho^2} + \frac{1}{\rho}\frac{\mathrm{d}a}{\mathrm{d}\rho} + \left(1 - \frac{1}{\rho^2}\right) a - a^3 = 0\,, \tag{4.4}$$

where $a(0) = 0$ and $a(\infty) = 1$ are the boundary conditions, $\rho = r/r_c$ is the reduced radial coordinate with core radius $r_c = (L/\pi)[(U/U_F)^2 - 1]^{-1/2}$ [111]. Eq. (4.4) is solved numerically and shown in Fig. 4.3(c), and the reduced core radius r_c/L as a function of the reduced voltage U/U_F is shown in Fig. 4.3(d).

Summarizing, the analytical description of umbilics is available. Still, in our case, we will omit the role of the core region and simply view umbilics as liquid crystal q-plates when the birefringence phase retardation Δ can be controlled by electrical means. Before doing so, we note that random distribution of umbilics as shown in Fig. 4.2(a) are not suitable for robust implementation as tunable q-plates. Indeed, umbilics with opposite topological charges tend to annihilate with time, leaving eventually to a uniform director field [112]. Such practical limitation has been addressed by using localized virtual (owing to the use of photoconductive substrate) [113] or real electrodes [114]. This however comes with practical tradeoff, for instance, regarding uncontrolled symmetry-breaking effects and efficiency. This has been solved in 2018 by introducing the additional use of an axisymmetric static magnetic field [115], which is described in the next section.

4.1.2 Magnetoelectric liquid crystal tunable q-plate

Stable and tunable isolated umbilical defect over macroscopic clear aperture can be achieved by using initially homogeneous nematic films under the combined action of a static magnetic field and a quasistatic electric field, as described in [115]. This electrically tunable liquid crystal q-plate behaves optically as an effective uniaxial slab with adjustable uniform birefringent phase retardation Δ and azimuthally varying slow axis lying in the (x, y) plane of the slab and orientated at angle $\Psi = \phi$ from the x axis, where ϕ is the polar angle in the plane of the waveplate. Moreover, its structural quality nearby the origin ($r = 0$) outperforms that obtained by photopatterning technology [31]. This leads to the polarization-controlled generation of optical vortices with topological charges $l = \pm 2$ [30].

Its experimental realization is illustrated in Fig. 4.4(a). A cylindrical Neodymium ring magnet with 6 mm height, 8 mm outer diameter and 2 mm inner diameter, and having its revolution axis along the z axis, is placed at $\simeq 2$ mm from the nematic slab lying in the (x, y) plane. At rest, the liquid crystal orientation is homogeneous and aligned along the z axis, as shown in Fig. 4.4(c). When a uniform quasistatic electric field is applied alone, a collection of umbilical defects with topological charges ± 1 appears randomly above a threshold applied voltage (see Fig. 4.2) and undergoes long-term collective annihilation dynamics, as early discussed by Rapini [111]. On the other hand, a single defect with topological charge +1 can be obtained by applying an extra magnetic field alone, as shown by Pieransky *et al.* [116] when using a disk magnet, but without providing a clear aperture or quasiuniform birefringent phase retardation. In

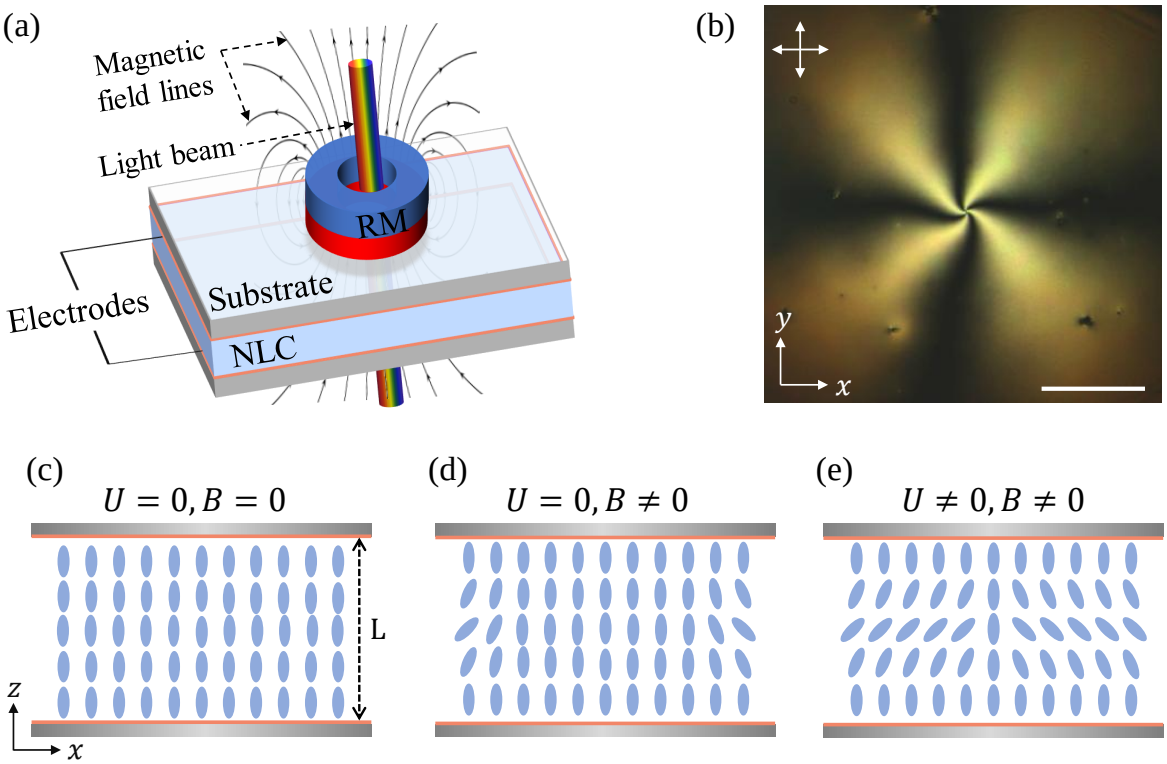

Figure 4.4 (a) Sketch of the magnetoelectric approach to producing a liquid crystal q-plate from nematic liquid crystal (NLC) film. RM: ring magnet and its associated magnetic field streamlines. (b) Observation of the structured waveplate between crossed linear polarizers under illumination from a supercontinuum laser beam with 0.75 mm waist radius, at an applied voltage of U = 6.2 V_{rms}. Scale bar: 400 μm Side view of the liquid crystal molecules and their orientation in the cell (c) at rest, (d) under the magnetic field alone, and (e) under the combined action of the magnetic and electric fields.

our case, the 3D magnetic field alone seeds the clear aperture of the annular magnet with a peripheral umbilical liquid crystal structure, as depicted in Fig. 4.4(d). This structure emerges from the thresholdless magnetic torque associated with the axisymmetric transverse component of the magnetic field. Then, applying an electric field, the director field eventually adopts a macroscopic, steady umbilical structure with a topological charge of +1 centered on the axis, see Fig. 4.4(e), as well as the experimental observation reported in Fig. 4.4(b). We note that the in-plane distribution of the director field exhibits an axisymmetric twisted pattern. This results from elastic anisotropy, with the twist elastic constant K_2 being the smallest. Consequently, the nematic tends to develop twist distortions where the director gradients are largest, even though the peripheral orientational boundary conditions tend to impose a splay umbilical structure [115]. In addition, the distance between the magnet and LC is a parameter that needs to be taken into account when preparing the umbilical structure. Indeed, a too

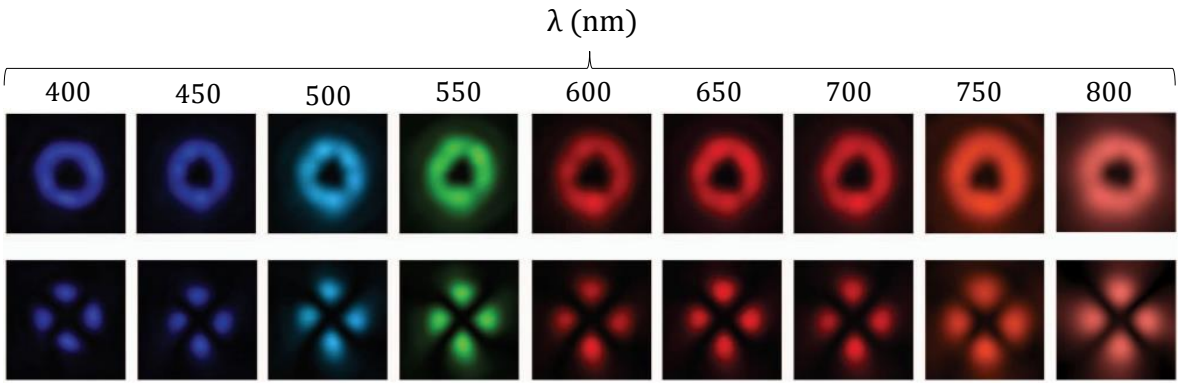

Figure 4.5 Optical vortex beams generated by LC magnetoelectric device from supercontinuum laser beam filtered with a set of nine wavelengths from 400 to 800 nm in steps of 50 nm, in the case of a horizontally polarized incident polarization state. The study is performed for $\Delta = \pi$ for all the wavelengths by adjusting the applied voltage accordingly. Top: far field total intensity profiles. Bottom: far field intensity profiles when a linear polarizer oriented along the x axis is placed at the output of the device. Image source: Ref. [115].

short distance can reverse the magnetic field lines [115, 117], while a too large distance weakens the magnetic field strength applied to the nematic, which leads to a random distribution of umbilical defects. In practice, the affordable range of distance varies for different nematics because their response to an applied magnetic field depends on the anisotropic part of the magnetic permeability tensor of the material.

Such liquid crystal q-plate can be used to generate vortex beams at any wavelength by tuning the applied voltage, as illustrated in Fig. 4.5, and we use it in this chapter for polychromatic light shaping.

4.2 Polychromatic structured beam shaping

4.2.1 State of the art

To date, the only previous work dealing with the structured beam shaping and the management of OAM across the spectral bandwidth of polychromatic beam via geometric phase optical elements adopted a multispectral approach. The latter is illustrated in Fig. 4.6(a) and consists in the use of a discrete set of geometric phase vortex generators with fixed [118] or distinct [119] topological charges, each generator being optimized for the wavelength to be processed. In order to avoid the preparation of a bulky system consisting of a set of macroscopic optical vortex generators that would prevent for possible applied developments, such an approach must come at the expense of technological

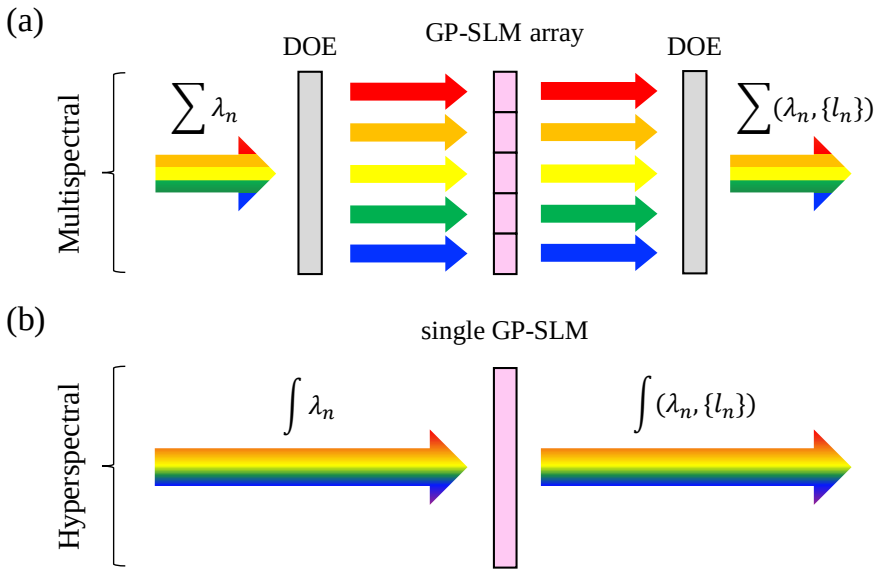

Figure 4.6 Principle of multispectral (top) and hyperspectral (bottom) optical OAM modulation of an incident polychromatic laser beam. DOE: dispersive optical element. The integers $\{l_n\}$ refer to the orbital angular momentum content of the wavelength λ_n.

efforts regarding the miniaturization and parallelization of individual monochromatic vortex shapers. So far, two experimental implementation have been made. The first one was based on the use of an array of electrically tunable liquid crystal q-plates with $q = \pm 1$ (microscopic umbilic defect localized by square electrodes) and 50 μm $\times$ 50 μm footprint [118], every q-plate of the array being possibly tuned to the chosen discrete set of wavelengths. The second demonstration was based on the use of an array of q-plates made of diamond metasurface, each of them having a disc-shaped footprint of 150 μm diameter, with distinct topological charges from 1/2 to 7/2. In that case, the topological charge diversity comes at the expense of the tunability.

Now, in contrast with the previous multispectral (discrete set of wavelengths) operation, we propose a hyperspectral approach (wavelength continuum). This is done by using a single-path liquid crystal q-plate, such as that described in Sec. 4.1.2, as depicted in Fig. 4.6(b). The idea is to exploit optically thick liquid crystal q-plate, for which different wavelengths can experience substantially different birefringence phase retardations.

For the sake of illustration, we chose a liquid crystal film that typically allows imparting a birefringent phase retardation difference $\delta\Delta \sim 2\pi$ of a polychromatic field, which we take as an ultrashort optical pulse with 10 fs duration, towards the development of novel tools for topological pulse shaping. Therefore, we consider the case study of a fully developed optical OAM modulation across the pulse spectrum. Let us define the

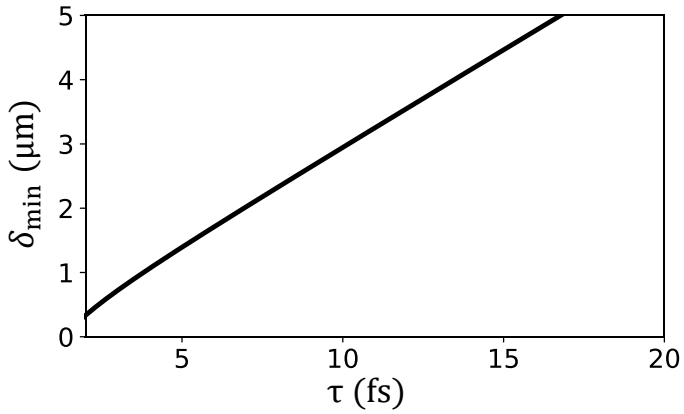

Figure 4.7 Minimal anisotropic optical path delay (retardance) ensuring $\delta\Delta = 2\pi$ across the characteristic spectral bandwidth of an optical pulse with characteristic duration τ, here plotted with $\bar{\lambda} = 800$ nm that is chosen as a representative wavelength for ultrashort pulses.

wavelength bandwidth of an optical pulse with central wavelength $\bar{\lambda}$ and characteristic duration τ as $\delta\lambda = \bar{\lambda}^2/(c\tau)$, where c is the speed of light in vacuum. Then we reformulate the criterion $\delta\Delta = 2\pi$ as a function of the corresponding required minimal anisotropic optical path difference δ_{min} between the extraordinary and the ordinary waves. Namely, $\delta_{\text{min}}\,(1/\lambda_1 - 1/\lambda_2) = 1$ where $\lambda_{1,2} = \bar{\lambda} \mp \delta\lambda/2$. This gives $\delta_{\text{min}} = c\tau[1 - (\bar{\lambda}/2c\tau)^2]$. As shown in Fig. 4.7 this gives $\delta_{\text{min}} \simeq 3$ μm for $\tau = 10$ fs.

Accordingly, based on the previous discussion, we use a $L = 10 \pm 0.5$ μm-thick cell (from EHC Co. Ltd.) provided with indium-tin-oxide electrodes and perpendicular molecular anchoring boundary conditions at both ends of the cell, filled with the nematic mixture 1910B (from Military University of Technology, Warsaw, Poland). This liquid crystal has a birefringence $dn \simeq 0.31$ at 589 nm wavelength and a negative dielectric anisotropy at 100 kHz frequency. Since the sample satisfies $Ldn \simeq 3$ μm condition, we expect to meet the discussed typical requirement by applying a sufficiently large voltage difference U, though keeping in mind that our experimental demonstration is restricted to the use of a supercontinuum light field in the framework of a proof-of-principle demonstration.

4.2.2 Spin-orbit beam shaping over the visible domain

The spectral optical OAM modulation capabilities of our device are first assessed using the experimental setup shown in Fig. 4.8(a). A collimated circularly polarized Gaussian beam with helicity $\sigma = \pm 1$ and waist radius ~ 0.7 mm impinges at normal incidence on the sample, centered on the liquid crystal topological defect. The output beam is

then redirected to a camera by a ruled reflective diffraction grating (GR13-0605 from Thorlabs) and analyzed as a function of the applied voltage difference U in the visible domain.

We record the spectrally dispersed beam intensity distribution in X, Y plane of the camera, see Fig. 4.8(a), as U increases with 0.05V step. At $U = 0$, the output light exhibits typical angular dispersion, as shown in Fig. 4.8(b). For $U < U_{\mathrm{F}}$, the spectrally dispersed intensity pattern is unchanged, as expected from the absence of liquid crystal reorientation below the Fréedericksz threshold. For $U > U_{\mathrm{F}}$, the pattern exhibits spectral modulation, as shown in Fig. 4.8(c), which is related to wavelength-dependent Δ. Indeed, when Δ is an odd multiple of π for a given wavelength the liquid crystal behaves as a pure optical vortex generator for the topological charge $l = 2\sigma$ [30], which depletes on-axis intensity as indicated by the white arrows in Fig. 4.8(c). All data is eventually collected into a single map by selecting the spectral intensity profile along the X axis at the value of Y where the modulation depth is the largest, see dashed line in Fig. 4.8(b), which leads to Fig. 4.8(d). There, the dark stripes correspond to $\Delta = n\pi$ with n odd integer. We note that the contrast of the latter is not maximal because of the overlap of the intensity patterns of distinct wavelengths in the plane of the camera. Moreover, we calibrate the X coordinate as a function of λ, by placing a homemade monochromator module (MC in Fig. 4.8(a), which is described in the next section) at the output of the supercontinuum laser source.

4.2.3 Implementation of a monochromator

The monochromator module is made of a ruled reflective diffraction grating (GR13-0605 from Thorlabs) in a rotation stage followed by a lens and a pinhole, see the experimental setup illustrated in Fig. 4.9(a). The goal is to select a narrow bandwidth of approximately $\delta\lambda \approx 1$ nm, with the ability to tune the wavelength by 1 nm steps over the visible spectrum from a supercontinuum laser source. To estimate the characteristics of the monochromator module, first, we define an angle $\delta\theta$, that corresponds to the angular spread of $\delta\lambda$ wavelength. Within the small divergence angle approximation, it can be expressed as a ratio between the diameter of the pinhole D and the focal length f of the lens

$$\delta\theta \approx \frac{D}{f}, \tag{4.5}$$

which indicates that only a particular $\delta\lambda$ wavelength can pass through the pinhole.

Then, we recall that the divergence angle of a Gaussian beam is given by $\theta_0 = \frac{\lambda}{\pi w_0}$ (see Sec. 1.1.1). Thus, the achievable beam waist w_0 in the focus can be expressed as

$$w_0 \approx \frac{\lambda f}{\pi w_{\text{in}}}. \tag{4.6}$$

where w_{in} is the beam waist radius at the plane of the focusing lens. To achieve the focused beam in the center of the pinhole we define $D = 2w_0$. Thus, combining Eqs. (4.5) and (4.6) we obtain a relationship between $\delta\theta$ and w_{in}

$$\delta\theta \approx \frac{2\lambda}{\pi w_{\text{in}}}. \tag{4.7}$$

Considering $\lambda = 500$ μm and $w_{\text{in}} = 1$ mm from Eq. (4.7) we find $\delta\theta \approx 0.32 \cdot 10^{-3}$. We have used a pinhole with $D = 2w = 100$ μm diameter, which accordingly, leads to the use of a lens with $f = \frac{D}{\delta\theta} \approx 310$ mm. The evaluation of the spectral bandwidth of the beam out of the monochromator module is made considering characteristic approximate numbers, such as $\Delta\theta \approx 5°$ for the angular spread over the whole visible spectrum from the grating, and $\Delta\lambda \approx 350$ nm for the range of the spectrum. This gives $\delta\lambda = \frac{\Delta\lambda\delta\theta}{\Delta\theta} \approx 1.3$ nm.

In the experiment, a lens with $f = 400$ nm is used, and the pinhole selects a typical full-width half-maximum spectral band of approximately 1.4 nm over the visible domain, as measured with a fiber-optics spectrometer Avantes AvaSpec-3648, see Fig. 4.9(b). A lens with 150 mm focal length is then placed after the pinhole in order to recollimate the beam with a typical waist radius of ~ 0.75 mm.

For the calibration of X coordinate with respect to λ, as implemented in Fig. 4.8(d), we change the wavelength by rotating the grating and find the coordinate of the beam on the camera with 5 nm step. This allows to establish a linear relationship between pixels and wavelength, as shown in Fig. 4.9(c). Moreover, the monochromator is also used to shape the light beam at any given wavelength, which is exploited in the next section.

4.2.4 Wavelength-resolved spin-orbit processing

By using the monochromator module, we can proceed to the fine analyses of optical OAM modulation. This is done by recording the transverse intensity profiles of the output field at every wavelength using the setup depicted in Fig. 4.10(a). Typical far field results are shown in Fig. 4.10(b) for wavelengths λ_n satisfying $\Delta(\lambda_n) = n\pi$ with n integer from $n = 7$ to $n = 13$, at $U = 2.2\ U_{\text{F}}$. The odd [even] values of n refer to

labels (A,B,C,D) [(A',B',C')] of Fig. 4.8(d). Qualitatively, the fact that optical vortex generation is complete for n odd and absent for n even is assessed by recording the fringes interference pattern resulting from the superposition of the output field at λ_n with a reference Gaussian beam at the same wavelength, at ~ 40 cm distance from the sample. Regular fringes pattern is indeed observed for even values of n whereas the interferograms exhibit a dislocation in the fringes pattern for odd values of n, as shown in Fig. 4.11(b). Moreover, the flipped orientation of the double-fork intensity patterns as the handedness of the incident circular polarization is flipped ascertains the generation of optical vortices with topological charges $l = 2\sigma = \pm 2$.

Quantitatively, the spectral dependence of the purity of the optical vortex generation process is assessed by measuring the power fraction η of the output beam that is contra-circularly polarized with respect to the incident circular polarization state with helicity σ. Namely, $\eta = P_{\text{out},-\sigma}/(P_{\text{out},\sigma} + P_{\text{out},-\sigma})$. As shown in Fig. 4.12(a), the purity of optical vortex generation oscillates with wavelength. Moreover, the shorter the wavelength, the faster the oscillation, as expected from the dependence on Δ, $\eta = \sin^2(\Delta/2)$, recalling that $\Delta = 2\pi L dn_{\text{eff}}/\lambda$ where dn_{eff} is the voltage-dependent effective birefringence of the slab. Interestingly, we find that assuming a constant dn_{eff} over the visible spectrum does not satisfactorily explain the observations, highlighting the need to account for the dispersive nature of birefringence. To a first approximation, the latter can be taken into account in a simple manner from the simplest Cauchy law $dn_{\text{eff}} = a + b/\lambda^2$ and using a and b as adjustable parameters, see the solid curve in Fig. 4.12(a).

The wavelength-dependent optical vortex generation purity allows producing the spatiospectral analog of a monochromatic bottle beam, which refers to a dark focus surrounded by regions of higher intensity [120]. Such a spatiospectral bottle beam demonstration is made by retrieving experimentally the wavelength dependence of the azimuth-averaged radial intensity profiles $\langle I \rangle_\phi$ of the output beam in the far field by using a wavelength step of 1 nm. The results are displayed in Fig. 4.12(b), where the observed array of spatiospectral bottles is shown together with its simulated counterpart. The simulations are made by calculating the Fourier transform of the field emerging from the sample, which is described as the sum of two orthogonally circularly polarized vortex and nonvortex fields, respectively weighted by the factors $\sin(\Delta/2)$ and $\cos(\Delta/2)$, using the analytical wavelength dependence of Δ found from Fig. 4.12(a). As described in Sec. 1.4.2, for an incident monochromatic circularly polarized field $E_{\text{in}}\mathbf{e}_\sigma$, the output

field can be written as

$$\mathbf{E}_{\text{out}} \propto E_{\text{in}}[\cos(\Delta/2)\mathbf{e}_{\sigma} + i\sin(\Delta/2)\exp(2i\sigma\phi)\mathbf{e}_{-\sigma}]. \tag{4.8}$$

Therefore, assuming an incident Gaussian beam, one gets a total far field intensity distribution

$$I = |\mathcal{F}_{\text{S}}[\sin(\Delta/2)\exp(-r^2/w^2 + 2i\sigma\phi)]|^2 + |\mathcal{F}_{\text{S}}[\cos(\Delta/2)\exp(-r^2/w_0^2)]|^2, \tag{4.9}$$

where $\mathcal{F}_{\text{S}}$ refers to the spatial Fourier transform and the beam waist radius w_0 is taken as 500 μm. By collecting calculations for the visible domain, we obtain the spatiospectral map shown in Fig. 4.12(b). We note that the color mismatch for wavelength between experiments and simulations results from the use of an ad hoc color bar for representing the visible domain in the calculations. In addition, the mismatch between experiment and simulation regarding the spectral positions of the bottles results from the fact that the experimental data shown in Fig. 4.12(a) and 4.12(b) corresponds to distinct experimental realizations (different days and sample positions). This allows appreciating the level of quantitative variability while the generation of the spatiospectral bottle beam chain is robust.

4.2.5 Ultrashort pulse shaping

The present results also enable spatiotemporal shaping of light through spectral optical OAM modulation of optical pulses. By considering a chirped optical pulse, where the frequency varies over time within the pulse, we can qualitatively approach spatiotemporal pulse shaping. Therefore, since the generation of optical vortices is wavelength-dependent, different temporal parts of the pulse will be distinctively shaped in the spatial domain. This is numerically explored by using an incident chirped Gaussian pulse centered on time $t = 0$ and described by the spatiotemporal waveform amplitude

$$E_{\text{in}}(\mathbf{r}, t) = E_0 e^{-r^2/w_0^2 + i\omega_0 t - \alpha t^2}, \tag{4.10}$$

where $\mathbf{r}$ is the position vector in the transverse plane, $\alpha = 1/t_0^2 - i\delta\omega/(2t_0)$, ω_0 is the central angular frequency, w_0 and t_0 are respectively the characteristic spatial and temporal pulse radius, and $\delta\omega$ denotes the instantaneous angular frequency shift at t_0, noting that $\omega(t) = \omega_0 + (t/t_0)\delta\omega$. The output field in the momentum-time domain is obtained by successive temporal ($\mathcal{F}_{\text{T}}$) and spatial ($\mathcal{F}_{\text{S}}$) Fourier transforms. First, the optical OAM

modulation process in the frequency domain is described by a straightforward extension of the monochromatic situation described above, namely,

$$\mathbf{E}_{\text{in}}(\mathbf{r},t) \rightarrow \mathbf{E}_{\text{out}}(\mathbf{r},\omega) = \mathcal{F}_{\text{T}}[\mathbf{E}_{\text{in}}(\mathbf{r},t)][\cos(\Delta(\omega)/2)\mathbf{c}_{\sigma} + i\sin(\Delta(\omega)/2)e^{2i\sigma\phi}\mathbf{c}_{-\sigma}]. \quad (4.11)$$

Here the temporal Fourier transform allows us to get the field in the space-frequency domain, where each frequency is modulated individually. From this we get back to the output field in the space-time domain by applying inverse temporal Fourier transform

$$\mathbf{E}_{\text{out}}(\mathbf{r},t) = \mathcal{F}_{\text{T}}^{-1}[\mathbf{E}_{\text{out}}(\mathbf{r},\omega)]. \quad (4.12)$$

The output field in the momentum-time domain is eventually obtained by applying spatial Fourier transform,

$$\mathbf{E}_{\text{out}}(\boldsymbol{\kappa},t) = \mathcal{F}_{\text{S}}[\mathbf{E}_{\text{out}}(\mathbf{r},t)]. \quad (4.13)$$

By using the spectral features extracted from the experiments in Fig. 4.11(c), we report in Fig. 4.13 a few kinds of axisymmetric pulses that could be obtained by adjusting the pulse parameters, provided that the spectrally dependent dynamic phase experienced by light as it passes through the optical element is compensated.

As the present manuscript is written, our liquid crystal device is being explored experimentally at the University of Shanghai for Science and Technology, China, in the group of Q. Zhan, towards the first implementation of single-path spatiotemporal pulse shaping.

Also, the reported approach could be extended to vectorial spatiotemporal shaping by using an arbitrary elliptical polarization state. Indeed, when the incident polarization state is not circular, every spectral component generates a superposition of contra-circularly polarized optical vortices carrying opposite topological charges, hence spatially varying polarization states. Finally, we emphasize that present results highlight previously overlooked advantages of optically thick geometric phase optical elements compared to those operating in the prototypical situation $\Delta = \pi$ that corresponds to zeroth-order structured half-waveplates.

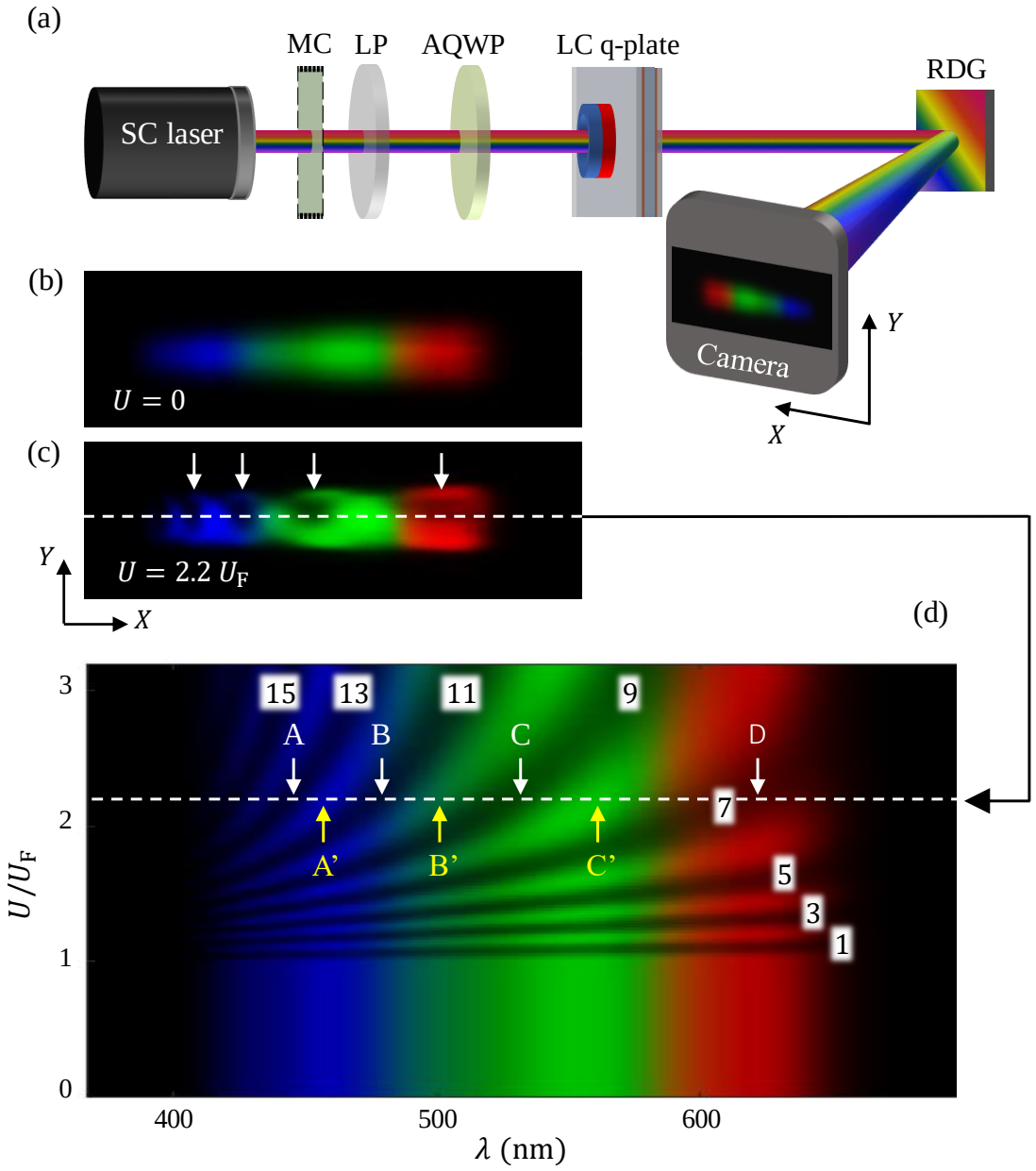

Figure 4.8 (a) Experimental setup to observe hyperspectral optical OAM modulation. SC laser: supercontinuum laser (NKT Photonics), visible output. MC: homemade monochromator that can be inserted on demand (see Sec. 4.2.3 for the description). LP: linear polarizer. AQWP: achromatic quarter-waveplate. RDG: ruled reflective diffraction grating. (b) Spatially dispersed output light field at zero applied voltage, which corresponds to the incident field spectrum. (c) Same as in panel (b) for U = 2.2 U_{F}. White arrows refers to wavelength experiencing pure optical vortex generation. (d) Summary of electrically controlled optical OAM modulation across the whole visible domain, where the white arrows refer to that shown in panel (c) and the odd integers from 1 to 15 refer to multiples of π for Δ.

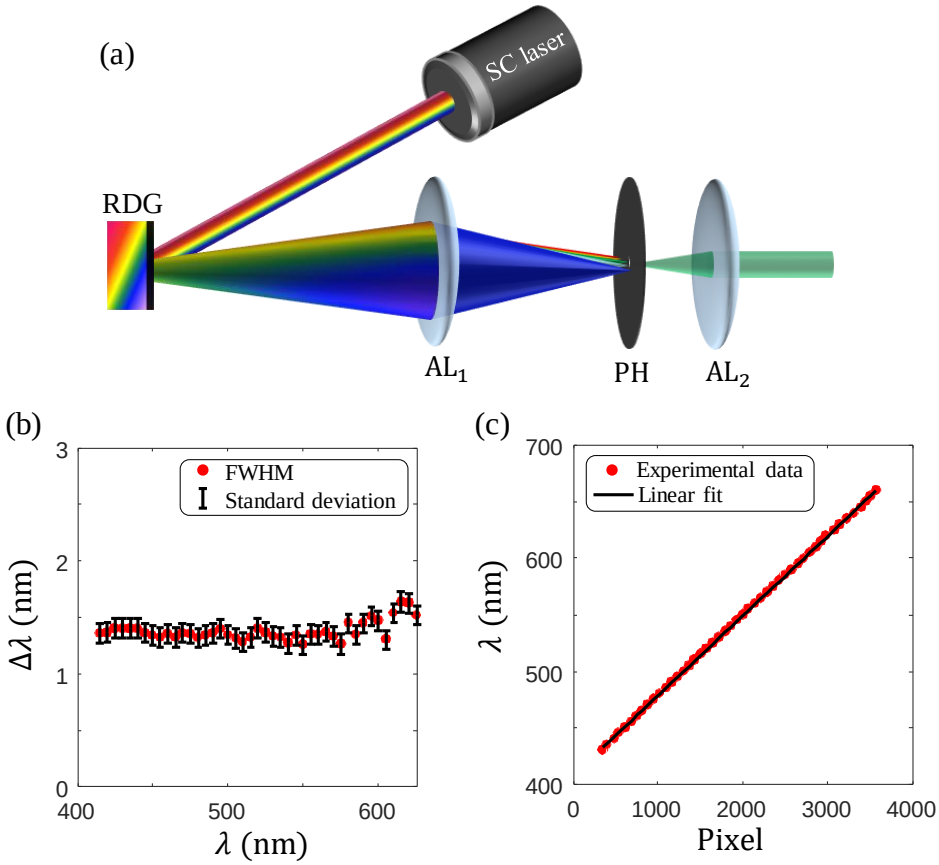

Figure 4.9 (a) Experimental setup of the monochromator. SC laser: supercontinuum laser. RDG: ruled reflective diffraction grating. AL_1: Achromatic lens with 400 mm focal length. PH: Pinhole with a 100 μm diameter. AL_2: Achromatic lens with 150 mm focal length. (b) Full-width half-maximum (FWHM) of the spectrum over the visible range with 5 nm wavelength step measured by fiber-optics spectrometer Avantes AvaSpec-3648 and the standard deviation from the mean value of FWHM. (c) Experimental data points with 5 nm wavelength step and a linear fit for pixel-to-wavelength calibration.

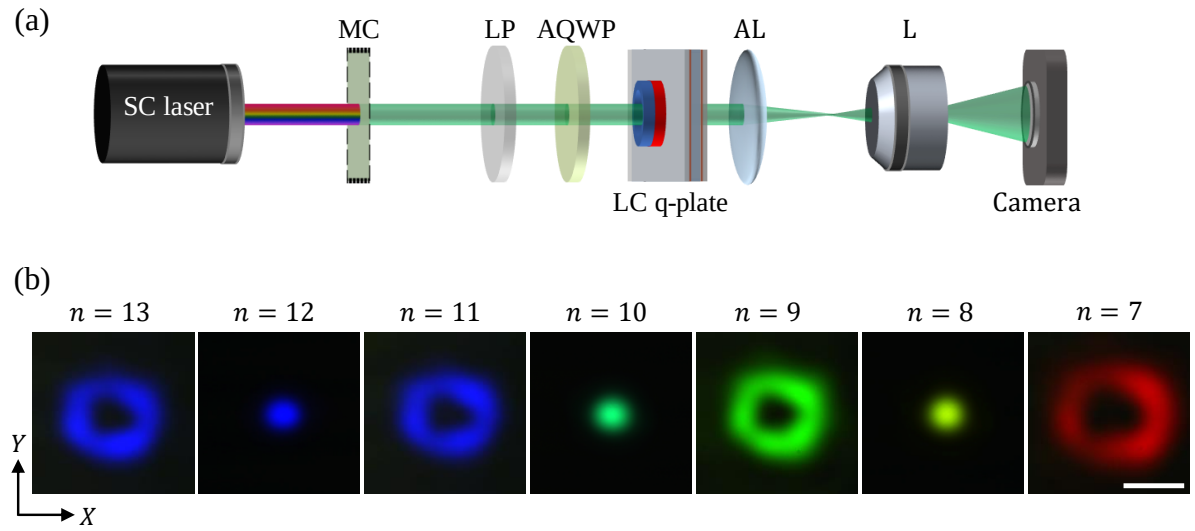

Figure 4.10 (a) Experimental setup to observe the far field transverse intensity profiles. SC laser: supercontinuum laser. MC: homemade monochromator. LP: linear polarizer. AQWP: achromatic quarter-waveplate. AL: Achromatic lens with 150 mm focal length. L: 4× microscope objective with numerical aperture NA = 0.1. (b) Experimental far field transverse intensity profiles for wavelength at which the birefringent phase retardation satisfies $\Delta = n\pi$ with n integer, at $U = 2.2\ U_{\mathrm{F}}$, which correspond to $\lambda_7 = 630$ nm, $\lambda_8 = 580$ nm, $\lambda_9 = 535$ nm, $\lambda_{10} = 505$ nm, $\lambda_{11} = 480$ nm, $\lambda_{12} = 460$ nm, and $\lambda_{13} = 445$ nm. Scale bar: 1 mm.

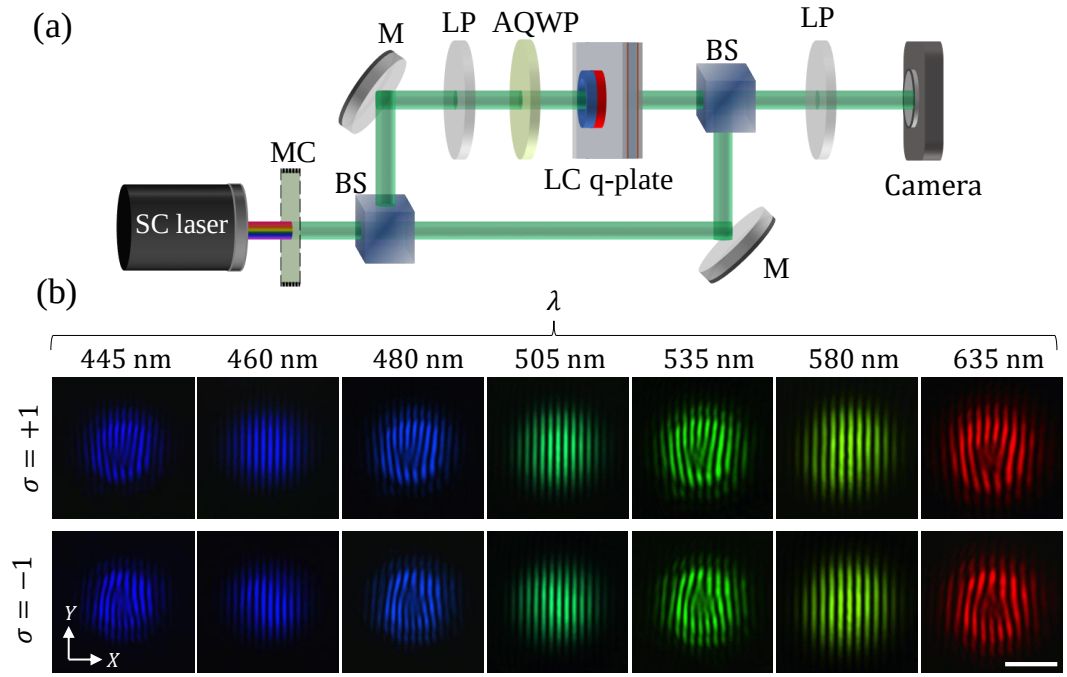

Figure 4.11 (a) Experimental setup to observe interference patterns between the output field and a Gaussian reference beam. SC laser: supercontinuum laser. MC: monochromator. BS: beamsplitter. LP: linear polarizer. AQWP: achromatic quarter-waveplate. M: mirror. (b) Interference intensity patterns between the output field and a Gaussian reference beam for the set of seven wavelengths λ_n used in Fig. 4.10 and for both incident circular polarization states. Scale bar: 1 mm.

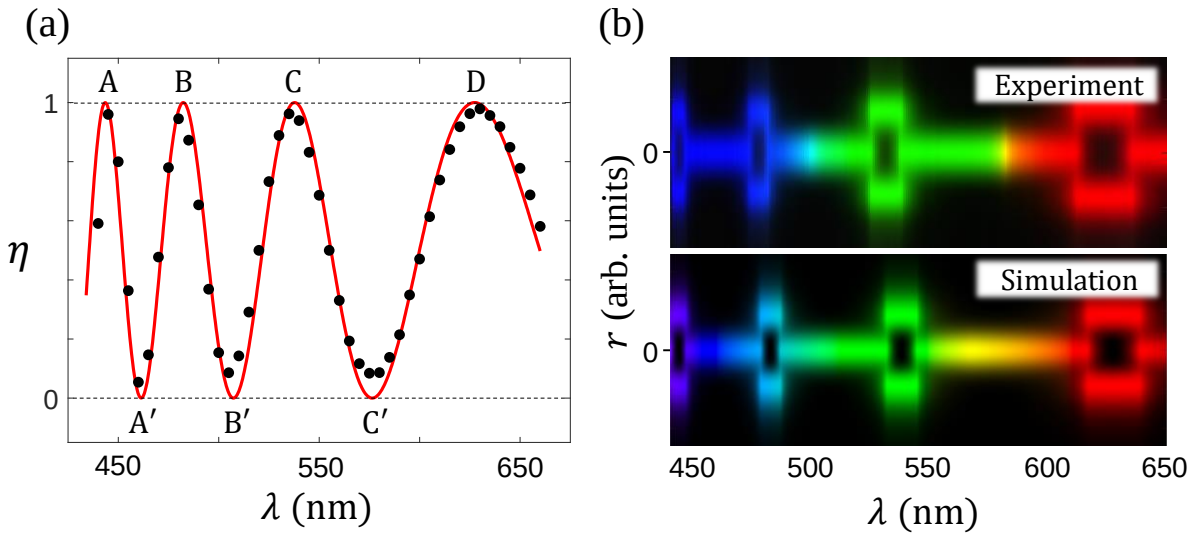

Figure 4.12 (a) Spectral behavior of the optical vortex generation purity. Markers: experimental data. Red curve: best-fit adjustment accounting for the dispersion of the birefringence. The letters (A, A', B, B', C, C', D) refer to Fig. 4.8(d). (b) Spectral bottle beam experimental demonstration and its simulated counterpart, obtained from the spatiospectral map of $\langle I \rangle_\phi$.

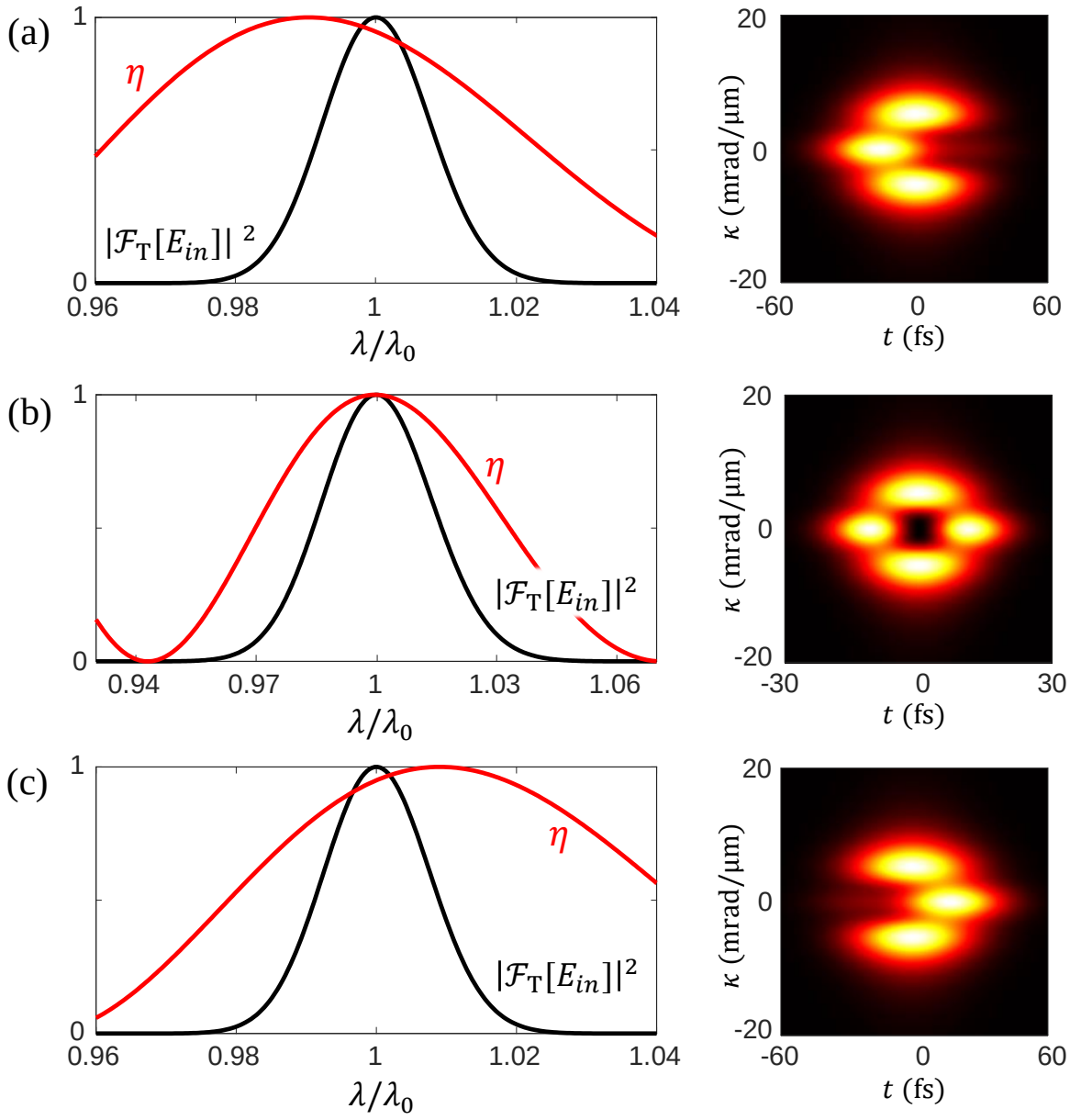

Figure 4.13 Demonstration of spatiotemporal shaping of chirped optical pulses for three distinct situations leading to backward arrow (a), bottle (b), and forward arrow (c) pulses. For each case, the normalized intensity spectrum (black curve), the optical vortex generation purity (red curve), and the shaped pulse in the momentum-time domain are shown. The hyperspectral vortex modulator characteristics are those of the experiments at $U = 2.2U_F$. Pulse parameters: (a) $\lambda_0 = 543$ nm, $t_0 = 50$ fs, $\delta\omega = 34.7$ mrad fs^{-1}. (b) $\lambda_0 = 538$ nm, $t_0 = 24$ fs, $\delta\omega = 46.7$ mrad fs^{-1}. (c) $\lambda_0 = 533$ nm, $t_0 = 50$ fs, $\delta\omega = 35.3$ mrad fs^{-1}. Incident beam waist $w_0 = 500$ μm.

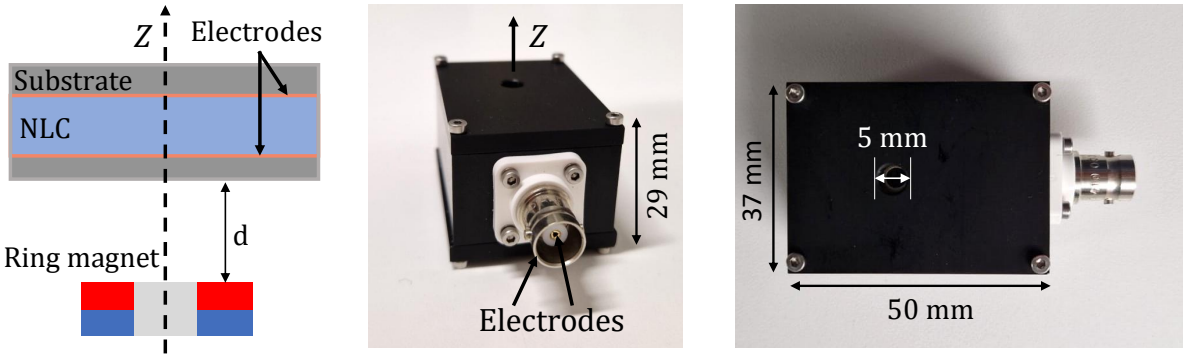

Figure 4.14 The schematic representation and direct image of the dual-wavelength devices.

4.3 Developing two-wavelength bimodal devices

In this section, we present the design and realization of liquid crystal structured waveplates designed to shape two distinct wavelengths: one into a vortex beam with $l = \pm 2\sigma$ and the other into a Gaussian beam from an incident circularly polarized Gaussian beam. This was motivated by the discussion with the group of A. Forbes, Wits University, South Africa. These devices are intended for use in two different experiments. One in the classical regime with the demonstration that nonlinear optics can be used to characterize the linear spin-orbit properties of a structured waveplate. The second one is planned in the quantum regime, with the demonstration of electrically controlled entanglement properties. The devices are made from the magnetoelectrical liquid crystal q-plate presented in Sec. 4.1.2.

4.3.1 Dual-wavelength device in the visible domain

Here we target a bimodal behavior for the wavelength $\lambda_1 = 532$ nm and $\lambda_2 = 633$ nm. Namely, we are interested in situation characterized by $(\eta_1, \eta_2) = (1, 0)$ or $(0, 1)$, where $\eta_{1,2}$ refers to the polarization conversion efficiency. For this purpose, we use a $L = 20$ μm-thick cell (from BeamCo.) provided with indium-tin-oxide electrodes and perpendicular molecular anchoring boundary conditions at both ends of the cell, filled with a nematic liquid crystal with birefringence $dn \simeq 0.097$ at 589 nm wavelength and a negative dielectric anisotropy $\epsilon_a = -6.4$ at 1 kHz frequency. A cylindrical Neodymium ring magnet with 6 mm height, 8 mm outer diameter and 4 mm inner diameter, and having its revolution axis along the z axis, is placed at $d \simeq 2$ mm from the nematic slab lying in the (x, y) plane. The schematic representation and the packaged version of the device are shown in Fig. 4.14.

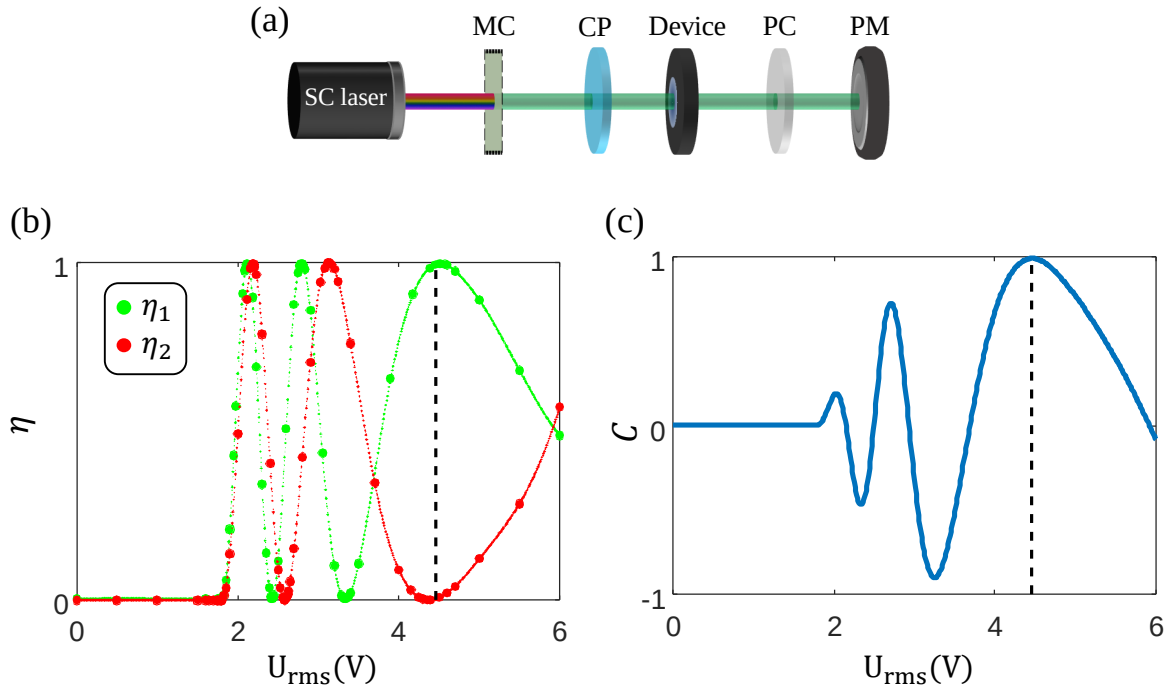

Figure 4.15 (a) Experimental setup for output power measurements. MC: monochromator described in 4.2.3 that allows us to switch between 532 nm and 633 nm wavelengths. CP: circular polarizer. PC: Polarization controller made of linear polarizer and quarter-waveplate to project co-circular and contra-circular components. PM: powermeter. Note that the quarter-waveplate and circular polarizer are switched between those made for 532 nm and 633 nm wavelengths, accordingly. (b) Experimentally measured vortex conversion purity factors η_1 and η_2 for 532 nm and 633 nm wavelengths, respectively. (c) The discriminatory parameter defined by $C = \eta_1 - \eta_2$, which allows us to find the operating voltage for two mentioned wavelengths.

The quantitative assessment of the device is carried out by measuring the power fraction η_1 and η_2 of the output beam that is contra-circularly polarized with respect to the incident circular polarization state with helicity σ. Namely, $\eta_{1,2} = P^{1,2}_{\text{out},-\sigma}/(P^{1,2}_{\text{out},\sigma} + P^{1,2}_{\text{out},-\sigma})$. The experiment was carried out with a 1.5 mm beam waist diameter continuous-wave laser. The experimental setup is shown in Fig. 4.15(a), and the results as a function of the applied voltage are shown in see Fig. 4.15(b). The determination of the voltage value satisfying $(\eta_1, \eta_2) = (1, 0)$ or $(0, 1)$ is grasped by introducing the quantity $C = \eta_1 - \eta_2$ and plotting it as a function of the applied voltage. Indeed, the sought-after corresponds to $C = \pm 1$. As shown in Fig. 4.15(c) the discriminatory parameter $C \approx 1$ when the applied voltage difference is 4.5 V_{rms}. This means that under that voltage value, the device behaves as a pure vortex generator for 532 nm and as an anisotropic medium for 633 nm wavelength.

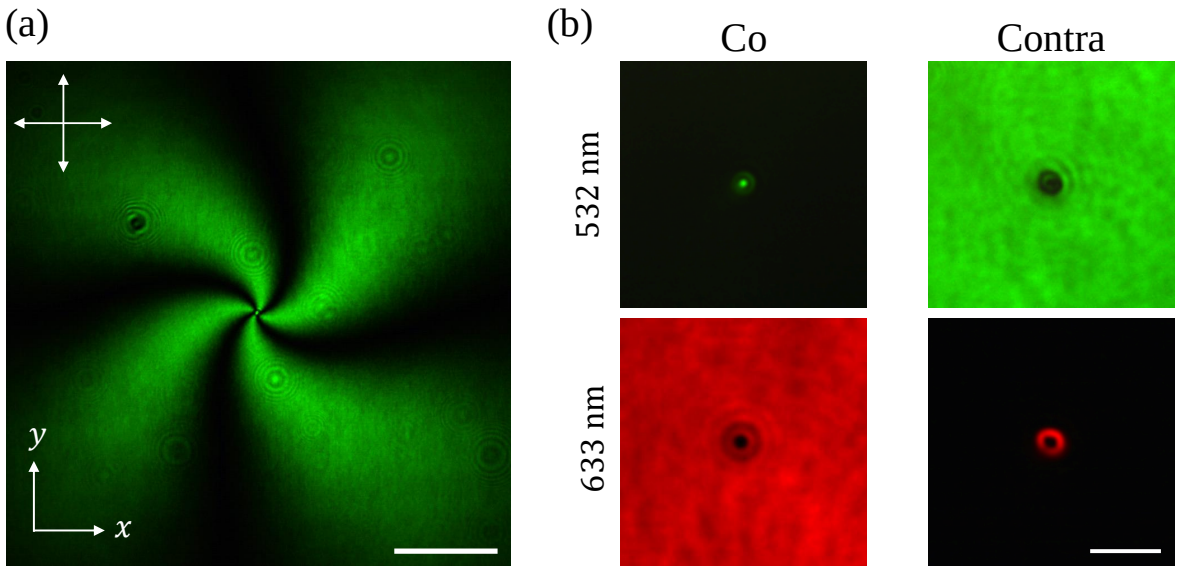

Figure 4.16 (a) Observation of the structure between crossed linear polarizers under illumination from a 532 nm laser beam with 0.75 mm waist radius. Scale bar: 300 μm. (b) Co- and contra-circularly polarized components of the core of the structure for both 532 nm and 633 nm wavelengths. Scale bar: 20 μm. In all cases, U = 4.5 V_{rms} voltage difference was applied.

A typical umbilical structure of LC between crossed linear polarizers and at an operating voltage ($\approx 4.5\ V$) is shown in Fig. 4.16(a) using green laser. Meanwhile, co-circular and contra-circular projections of the output field at the sample plane are shown in Fig. 4.16(b), which highlights the detection of almost null intensity of co-circular and contra-circular components of the output field, respectively, for 532 nm and 633 nm wavelengths, except in the core region of the umbilic, as anticipated by the fact that $\Delta \to 0$ as $r \to 0$ whatever the wavelength.

The intensity profiles of the beam after 60 cm of propagation from the device at 4.5 V_{rms} are presented in Fig. 4.17 for two different beam waists. The red arrow indicates the effect of beam clipping for a 2 mm beam waist diameter when no voltage is applied. This clipping also contributes to the ringing pattern observed in the vortex beam when the voltage is applied. In contrast, a pure vortex beam is generated with a smaller beam.

Then intensity profiles recorded at a distance of $\approx$ 60 cm from the device are shown in Fig. 4.17 for two different beam waist values. The red arrow indicates the effect of beam cropping for a 2 mm beam waist diameter when no voltage is applied. This cropping also contributes to the ringing pattern observed in the vortex beam when the corresponding voltage is applied. In contrast, a pure vortex is generated with a smaller beam. This invites to properly choose the beam waist in order to avoid such unwanted extra intensity modulation.

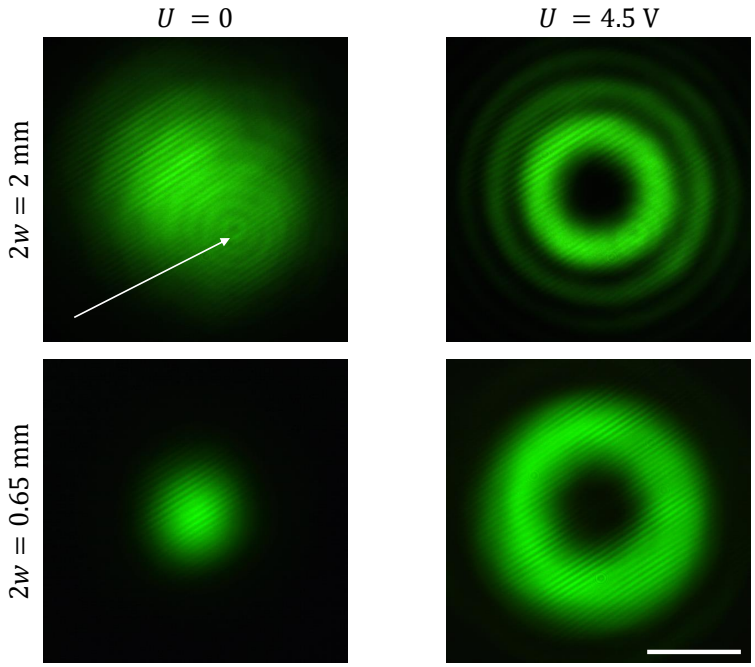

Figure 4.17 Total output intensity after 60 cm from the device when the applied voltage is 0 (left column) and $U = 4.5\ V_{rms}$ (right column) for 0.65 mm (top) and 2 mm (bottom) incident beam waist diameter. Scale bar: 1 mm

4.3.2 Dual-wavelength device in the infrared domain

In this section, we present a similar device, this time operating in the infrared domain. It specifically leaves the $\lambda_1 = 800$ nm wavelength unaffected, while generating a vortex beam from a $\lambda_2 = 1550$ nm laser beam. We use a $L = 10 \pm 0.5$ μm-thick cell (from EHC Co. Ltd.) provided with indium-tin-oxide electrodes and perpendicular molecular anchoring boundary conditions at both ends of the cell, filled with the nematic mixture 1859A. This liquid crystal has a birefringence $dn \simeq 0.229$ at 589 nm wavelength and a negative dielectric anisotropy at 100 kHz frequency.

In contrast to the previous section dealing with visible wavelengths, here the experiment is conducted in two steps. First, the evaluation of η_1 is made using the visible output port of a supercontinuum laser source along with a 800 nm bandpass filter having a 12 nm spectral bandwidth. A linear polarizer and an achromatic quarter-waveplate (AQWP05M-600 from Thorlabs) were employed to prepare the circular polarization state and its corresponding co-circular and contra-circular projections. Second, the evaluation of η_2 is carried out using the infrared output port of the supercontinuum laser source with a 1550 nm bandpass filter, also with a 12 nm spectral bandwidth. A

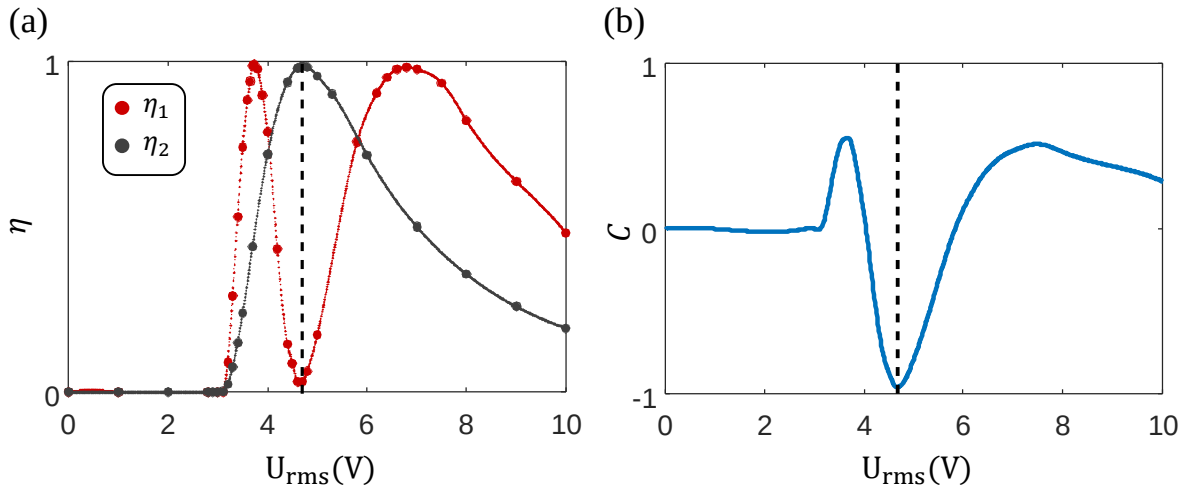

Figure 4.18 (a) Experimentally measured vortex conversion purity factors η_1 and η_2 for 1550 nm and 800 nm wavelenghts, respectively. (b) The discriminatory parameter $C = \eta_1 - \eta_2$ for the above-mentioned mentioned wavelengths.

linear polarizer and an achromatic quarter-waveplate (AQWP05M-1600 from Thorlabs), designed for infrared are used.

The results are shown in Fig. 4.18. We find $C \approx -1$ when the applied voltage difference is 4.7 V_{rms}. The image of the structure between crossed linear polarizers under an applied operating voltage of 4.7 V is shown in Fig. 4.19(a) and the generated vortex beam intensity profile after $\approx$ 60 cm propagation when using a 1550 nm laser beam is presented in Fig. 4.19(b).

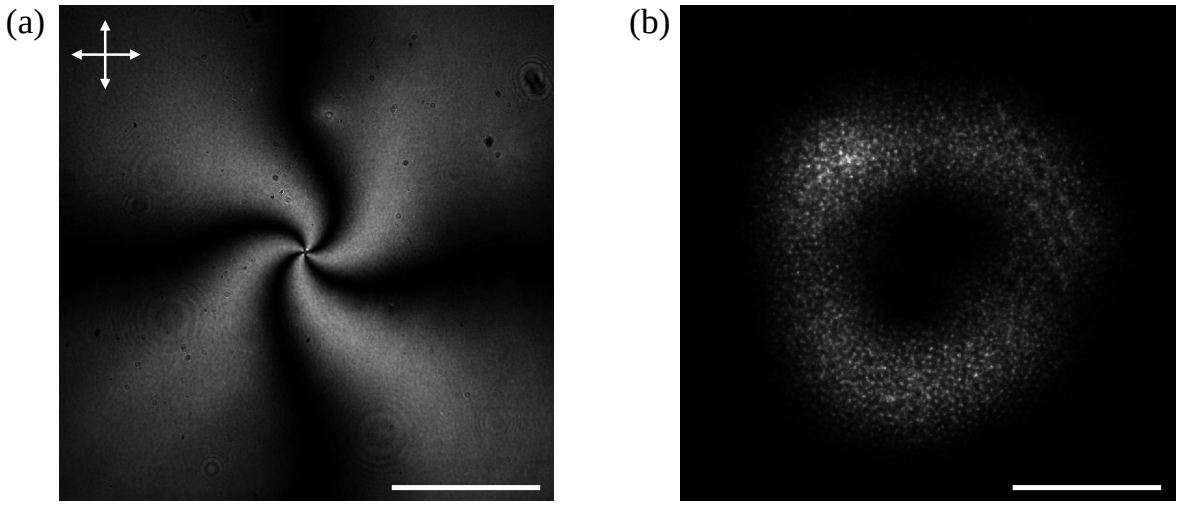

Figure 4.19 (a) Observation of the structure between crossed linear polarizers under illumination from a supercontinuum source filtered by 1550 nm bandpass filter. Scale bar: 300 μm (b) Total output intensity after 60 cm of propagation from the device when for 1550 nm incident laser beam. The applied voltage is $U = 4.7$ V_{rms} for both cases. Scale bar: 1 mm.

4.4 Concluding remarks

The results presented in this chapter demonstrate the capability of self-engineered liquid crystal devices to reconfigure and tune, by electrical means, the spatial and spectral distribution of light. Such flexible spatiospectral asset is not limited to the specific wavelengths discussed here and can be readily extended to other spectral regions with appropriate design and optimization. New future results that will be obtained from ongoing experimental developments with our collaborators from China and South Africa, as previously mentioned, are expected to further highlight that new classes of experiments that would hardly be realized otherwise become possible with our tunable structured liquid crystal waveplates.

Conclusion and perspectives

In this work, we have addressed three aspects of single-path spin-orbit beam shaping: modal beam shaping, vectorial beam shaping, and spatiospectral beam shaping. The first aspect enables precise control over the radial and azimuthal degrees of freedom of light. The second tailors the polarization texture of the beam towards the development of robust optical elements generating skyrmionic beams. Finally, the third aspect provides not only spatial but also spectral modulation of polychromatic light fields.

In chapter 2 we have detailed the experimental realization of modal beam shaping using anisotropic inhomogeneous dielectric flat media, as theoretically proposed in 2017 [40]. These "modal plates" are designed to convert an incident Gaussian beam into a pure Laguerre-Gaussian beam with arbitrary radial and azimuthal indices owing to space-varying retardance and slow axis orientation which allows modulating both the amplitude and phase of the incident beam. Two different experimental approaches based on nanostructured silica glass and dielectric metasurfaces have been discussed, highlighting the generic nature of the presented modal beam shaping approach. The underlying method can be applied to any family of spatial modes and to any material that can be inhomogeneously structured to meet the modal requirements. Pure Laguerre-Gaussian modes with fundamental radial order have been achieved using nanostructured silica glass plates while being modal only for one spin state, so far. The first experimental attempt to achieve spin symmetric modal plates has been introduced in the framework of optical dielectric metasurfaces and its extension to generate high-order radial modes has been presented in the infrared domain. So far, the work presented in Sec. 2.3 has led to a publication [81].

In chapter 3 we have proposed the use of anisotropic and inhomogeneous waveplates to generate skyrmionic beams from uniformly polarized Gaussian beams. We have demonstrated the generation of skyrmions in the central part of the beam and we have shown that the Skyrme number is subjected to deviation with propagation, which calls for further work regarding to topological stability. Also, we have extended the original q-plate design by adding a second winding number associated with the radial

degree of freedom. We have shown that this new design of structured waveplates results in the generation of skyrmions with well-defined Skyrme number related to the design choice. We have experimentally shown the generation and detection of skyrmions as well as the ability to control the Skyrme number via incident polarization state. Moreover, cascading such q^2-plates allows generating and manipulating high-order skyrmions and multiskyrmions from low-order structured optical elements. We highlighted that the topological stability of the generated skyrmionic beams with respect to propagation in free space suffers from the nonuniform dynamic phase and also from the presence of more than two modes in the superposition. Future works are planned to address these limitations. Sec. 3.2 has led to a publication [121] and Sec. 3.3 has led to an article currently being under review.

In chapter 4 we extended the idea of multispectral orbital angular momentum modulation to its hyperspectral counterpart with the use of a single-path scheme in contrast to the previous multispectral approach. We have experimentally reported orbital angular momentum modulation over the entire visible spectrum using a monochromatic laser source. Also, numerical simulations allowed us to articulate an anticipated use for 3D topological shaping of ultrashort optical pulses, which is being implemented experimentally with ongoing collaboration with Q. Zhan. Finally, we have developed customized liquid crystal devices capable of shaping two distinct wavelengths with distinct modality. Further experimental developments using these devices are currently being pursued in both classical and quantum regimes within another collaborative framework with A. Forbes. So far, Sec. 4.2 has led to a publication [122], while another one exploiting dual-wavelength devices is being prepared.

The results presented in this thesis provide an original single-path approach to spin-orbit beam shaping in temporal, spatial, spectral, and polarization domains, which might eventually seed the emergence of novel applications owing to the compactness of the approach and its polarization control capabilities, thus opening new avenues for preparing pulses with tailored vectorial spatiotemporal properties.

Bibliography

[1] A. Forbes, M. de Oliveira, and M. R. Dennis, "Structured light", *Nature Photonics* **15**, 253 (2021).

[2] M. A. Alonso, "Geometric descriptions for the polarization of nonparaxial light: a tutorial", *Advances in Optics and Photonics* **15**, 176 (2023).

[3] M. Born and E. Wolf, *Principles of optics: electromagnetic theory of propagation, interference and diffraction of light* (Elsevier, 2013).

[4] H. Poincaré, *Théorie mathématique de la lumière II.: Nouvelles études sur la diffraction.–Théorie de la dispersion de Helmholtz. Leçons professées pendant le premier semestre 1891-1892* (G. Carré, 1889), Vol. 1.

[5] H. Jerrard, "Transmission of light through birefringent and optically active media: the Poincaré sphere", *Journal of the Optical Society of America* **44**, 634 (1954).

[6] B. Kahr, "Poincaré and his polarization sphere", *Chirality* **33**, 758 (2021).

[7] A. E. Siegman, *Lasers* (University Science Books, 1986).

[8] C. Rosales-Guzmán, B. Ndagano, and A. Forbes, "A review of complex vector light fields and their applications", *Journal of Optics* **20**, 123001 (2018).

[9] W.-H. Lee, "Binary computer-generated holograms", *Applied Optics* **18**, 3661 (1979).

[10] C. Rosales-Guzmán and A. Forbes, *How to shape light with spatial light modulators* (Society of Photo-Optical Instrumentation Engineers (SPIE), 2017).

[11] V. Arrizón, U. Ruiz, R. Carrada, and L. A. González, "Pixelated phase computer holograms for the accurate encoding of scalar complex fields", *Journal of the Optical Society of America A* **24**, 3500 (2007).

[12] Y.-X. Ren, R.-D. Lu, and L. Gong, "Tailoring light with a digital micromirror device", *Annalen der Physik* **527**, 447 (2015).

[13] V. Lerner, D. Shwa, Y. Drori, and N. Katz, "Shaping Laguerre–Gaussian laser modes with binary gratings using a digital micromirror device", *Optics Letters* **37**, 4826 (2012).

[14] S. Scholes, R. Kara, J. Pinnell, V. Rodríguez-Fajardo, and A. Forbes, "Structured light with digital micromirror devices: a guide to best practice", *Optical Engineering* **59**, 041202 (2020).

[15] L. J. Hornbeck, "From cathode rays to digital micromirrors: A history of electronic projection display technology", *Texas Instruments Technical Journal* **15**, 7 (1998).

[16] D. Dudley, W. M. Duncan, and J. Slaughter, "Emerging digital micromirror device (DMD) applications", *SPIE digital library: MOEMS display and imaging systems* **4985**, 14 (2003).

[17] M. Mirhosseini, O. S. Magana-Loaiza, C. Chen, B. Rodenburg, M. Malik, and R. W. Boyd, "Rapid generation of light beams carrying orbital angular momentum", *Optics Express* **21**, 30196 (2013).

[18] M. A. Neil, F. Massoumian, R. Juškaitis, and T. Wilson, "Method for the generation of arbitrary complex vector wave fronts", *Optics Letters* **27**, 1929 (2002).

[19] X.-L. Wang, J. Ding, W.-J. Ni, C.-S. Guo, and H.-T. Wang, "Generation of arbitrary vector beams with a spatial light modulator and a common path interferometric arrangement", *Optics Letters* **32**, 3549 (2007).

[20] M. Bashkansky, D. Park, and F. K. Fatemi, "Azimuthally and radially polarized light with a nematic SLM", *Optics Express* **18**, 212 (2009).

[21] H. Chen, J. Hao, B.-F. Zhang, J. Xu, J. Ding, and H.-T. Wang, "Generation of vector beam with space-variant distribution of both polarization and phase", *Optics Letters* **36**, 3179 (2011).

[22] S. Liu, P. Li, T. Peng, and J. Zhao, "Generation of arbitrary spatially variant polarization beams with a trapezoid Sagnac interferometer", *Optics Express* **20**, 21715 (2012).

[23] Z.-Y. Rong, Y.-J. Han, S.-Z. Wang, and C.-S. Guo, "Generation of arbitrary vector beams with cascaded liquid crystal spatial light modulators", *Optics Express* **22**, 1636 (2014).

[24] B. Rodenburg, M. Mirhosseini, O. S. Magaña-Loaiza, and R. W. Boyd, "Experimental generation of an optical field with arbitrary spatial coherence properties", *Journal of the Optical Society of America B* **31**, A51 (2014).

[25] L. Gong, Y. Ren, W. Liu, M. Wang, M. Zhong, Z. Wang, and Y. Li, "Generation of cylindrically polarized vector vortex beams with digital micromirror device", *Journal of Applied Physics* **116**, (2014).

[26] C. Maurer, A. Jesacher, S. Fürhapter, S. Bernet, and M. Ritsch-Marte, "Tailoring of arbitrary optical vector beams", *New Journal of Physics* **9**, 78 (2007).

[27] S. Tripathi and K. C. Toussaint Jr, "Versatile generation of optical vector fields and vector beams using a non-interferometric approach", *Optics Express* **20**, 10788 (2012).

[28] K. Y. Bliokh, F. J. Rodríguez-Fortuño, F. Nori, and A. V. Zayats, "Spin–orbit interactions of light", *Nature Photonics* **9**, 796 (2015).

[29] V. Liberman and B. Y. Zel'dovich, "Spin-orbit interaction of a photon in an inhomogeneous medium", *Physical Review A* **46**, 5199 (1992).

[30] L. Marrucci, C. Manzo, and D. Paparo, "Optical spin-to-orbital angular momentum conversion in inhomogeneous anisotropic media", *Phyical Review Letters* **96**, 163905 (2006).

[31] B. Piccirillo, V. D'Ambrosio, S. Slussarenko, L. Marrucci, and E. Santamato, "Photon spin-to-orbital angular momentum conversion via an electrically tunable q-plate", *Applied Physics Letter* **97**, 241104 (2010).

[32] P. Török and P. Munro, "The use of Gauss-Laguerre vector beams in STED microscopy", *Optics Express* **12**, 3605 (2004).

[33] M. G. Gustafsson, "Nonlinear structured-illumination microscopy: wide-field fluorescence imaging with theoretically unlimited resolution", *Proceedings of the National Academy of Sciences* **102**, 13081 (2005).

[34] D. L. Andrews, *Structured light and its applications: An introduction to phase-structured beams and nanoscale optical forces* (Academic press, 2011).

[35] J. Wang *et al.*, "Terabit free-space data transmission employing orbital angular momentum multiplexing", *Nature Photonics* **6**, 488 (2012).

[36] S. Segawa, Y. Kozawa, and S. Sato, "Resolution enhancement of confocal microscopy by subtraction method with vector beams", *Optics Letters* **39**, 3118 (2014).

[37] M. Chen, K. Dholakia, and M. Mazilu, "Is there an optimal basis to maximise optical information transfer?", *Scientific Reports* **6**, 22821 (2016).

[38] V. Arrizón, G. Méndez, and D. Sánchez-de La-Llave, "Accurate encoding of arbitrary complex fields with amplitude-only liquid crystal spatial light modulators", *Optics Express* **13**, 7913 (2005).

[39] A. Forbes, A. Dudley, and M. McLaren, "Creation and detection of optical modes with spatial light modulators", *Advances in Optics and Photonics* **8**, 200 (2016).

[40] M. Rafayelyan and E. Brasselet, "Laguerre-Gaussian modal q-plates", *Optics Letters* **42**, 1966 (2017).

[41] M. Rafayelyan, T. Gertus, and E. Brasselet, "Laguerre-Gaussian quasi-modal q-plates from nanostructured glasses", *Applied Physics Letters* **110**, 261108 (2017).

[42] D. Coursault and E. Brasselet, "Nanostructured silica spin-orbit optics for modal vortex beam shaping", *Nanophotonics* **11**, 805 (2022).

[43] H. Mao, Y.-X. Ren, Y. Yu, Z. Yu, X. Sun, S. Zhang, and K. K. Wong, "Broadband meta-converters for multiple Laguerre-Gaussian modes", *Photonics Research* **9**, 1689 (2021).

[44] M. Piccardo and A. Ambrosio, "Arbitrary polarization conversion for pure vortex generation with a single metasurface", *Nanophotonics* **10**, 727 (2021).

[45] M. Jin, B. Sanchez-Padilla, X. Liu, Y. Tang, Z. Hu, K. Li, D. Coursault, G. Li, and E. Brasselet, "Spin-Orbit Modal Optical Vortex

Beam Shaping from Dielectric Metasurfaces", *Advanced Optical Materials* 2202149 (2022).

[46] M. de Oliveira, M. Piccardo, S. Eslami, V. Aglieri, A. Toma, and A. Ambrosio, "Radially and azimuthally pure vortex beams from phase-amplitude metasurfaces", *ACS Photonics* **10**, 290 (2023).

[47] M. Jin, B. Sanchez-Padilla, X. Liu, Y. Tang, Z. Hu, K. Li, D. Coursault, G. Li, and E. Brasselet, "Spin-Orbit Modal Optical Vortex Beam Shaping from Dielectric Metasurfaces", *Advanced Optical Materials* **12**, 2202149 (2024).

[48] G. Della Valle, R. Osellame, and P. Laporta, "Micromachining of photonic devices by femtosecond laser pulses", *Journal of Optics A: Pure and Applied Optics* **11**, 013001 (2008).

[49] M. Sakakura, Y. Lei, L. Wang, Y.-H. Yu, and P. G. Kazansky, "Ultralow-loss geometric phase and polarization shaping by ultrafast laser writing in silica glass", *Light: Science & Applications* **9**, 15 (2020).

[50] Y. Lei, H. Wang, G. Shayeganrad, and P. G. Kazansky, "Ultrafast laser nanostructuring in transparent materials for beam shaping and data storage", *Optical Materials Express* **12**, 3327 (2022).

[51] G. Shayeganrad, X. Chang, H. Wang, C. Deng, Y. Lei, and P. G. Kazansky, "High damage threshold birefringent elements produced by ultrafast laser nanostructuring in silica glass", *Optics Express* **30**, 41002 (2022).

[52] M. Born and E. Wolf, *Principles of Optics* (Cambridge University Press, Cambridge, England, 2019).

[53] G. Vallone, A. Sponselli, V. D'Ambrosio, L. Marrucci, F. Sciarrino, and P. Villoresi, "Birth and evolution of an optical vortex", *Optics Express* **24**, 16390 (2016).

[54] B. Sephton, A. Dudley, and A. Forbes, "Revealing the radial modes in vortex beams", *Applied Optics* **55**, 7830 (2016).

[55] J. Pinnell, I. Nape, B. Sephton, M. A. Cox, V. Rodríguez-Fajardo, and A. Forbes, "Modal analysis of structured light with spatial light modulators: a practical tutorial", *Journal of the Optical Society of America A* **37**, C146 (2020).

[56] G. Vallone, "Role of beam waist in Laguerre–Gauss expansion of vortex beams", *Optics Letters* **42**, 1097 (2017).

[57] I. Nape, B. Sephton, Y.-W. Huang, A. Vallés, C.-W. Qiu, A. Ambrosio, F. Capasso, and A. Forbes, "Enhancing the modal purity of orbital angular momentum photons", *Applied Physics Letters Photonics* **5**, 070802 (2020).

[58] F. Mei *et al.*, "Cascaded metasurfaces for high-purity vortex generation", *Nature Communications* **14**, 6410 (2023).

[59] R. Drevinskas and P. G. Kazansky, "High-performance geometric phase elements in silica glass", *Applied Physics Letters Photonics* **2**, (2017).

[60] J. Harrison, W. T. Buono, A. Forbes, and D. Naidoo, "Aberration-induced vortex splitting in amplified orbital angular momentum beams", *Optics Express* **31**, 17593 (2023).

[61] E. Brasselet, "Babinet-bilayered geometric phase optical elements", *Optics Letters* **43**, 2623 (2018).

[62] T. H. R. Skyrme, "A unified field theory of mesons and baryons", *Nuclear Physics* **31**, 556 (1962).

[63] H. Ge, X.-Y. Xu, L. Liu, R. Xu, Z.-K. Lin, S.-Y. Yu, M. Bao, J.-H. Jiang, M.-H. Lu, and Y.-F. Chen, "Observation of Acoustic Skyrmions", *Phyical Review Letters* **127**, 144502 (2021).

[64] R. D. Muelas-Hurtado, K. Volke-Sepúlveda, J. L. Ealo, F. Nori, M. A. Alonso, K. Y. Bliokh, and E. Brasselet, "Observation of Polarization Singularities and Topological Textures in Sound Waves", *Phyical Review Letters* **129**, 204301 (2022).

[65] D. A. Smirnova, F. Nori, and K. Y. Bliokh, "Water-Wave Vortices and Skyrmions", *Phyical Review Letters* **132**, 054003 (2024).

[66] Y. Shen, Q. Zhang, P. Shi, L. Du, X. Yuan, and A. V. Zayats, "Optical skyrmions and other topological quasiparticles of light", *Nature Photonics* **18**, 15 (2024).

[67] S. Tsesses, E. Ostrovsky, K. Cohen, B. Gjonaj, N. Lindner, and G. Bartal, "Optical skyrmion lattice in evanescent electromagnetic fields", *Science* **361**, 993 (2018).

[68] H. Wang and S. Fan, "Photonic spin hopfions and monopole loops", *Physical Review Letters* **131**, 263801 (2023).

[69] A. A. Wang *et al.*, "Topological Protection of Optical Skyrmions through Complex Media", *arXiv preprint arXiv:2403.07837* (2024).

[70] S. Gao, F. C. Speirits, F. Castellucci, S. Franke-Arnold, S. M. Barnett, and J. B. Götte, "Paraxial skyrmionic beams", *Physical Review A* **102**, 053513 (2020).

[71] Y. Shen, E. C. Martínez, and C. Rosales-Guzmán, "Generation of optical skyrmions with tunable topological textures", *ACS Photonics* **9**, 296 (2022).

[72] D. Sugic, R. Droop, E. Otte, D. Ehrmanntraut, F. Nori, J. Ruostekoski, C. Denz, and M. R. Dennis, "Particle-like topologies in light", *Nature communications* **12**, 1 (2021).

[73] Y. Shen, Y. Hou, N. Papasimakis, and N. I. Zheludev, "Supertoroidal light pulses as electromagnetic skyrmions propagating in free space", *Nature communications* **12**, 5891 (2021).

[74] A. Zdagkas, C. McDonnell, J. Deng, Y. Shen, G. Li, T. Ellenbogen, N. Papasimakis, and N. I. Zheludev, "Observation of toroidal pulses of light", *Nature Photonics* **16**, 523 (2022).

[75] Y. Shen, B. Yu, H. Wu, C. Li, Z. Zhu, and A. V. Zayats, "Topological transformation and free-space transport of photonic hopfions", *Advanced Photonics* **5**, 015001 (2023).

[76] D. Ehrmanntraut, R. Droop, D. Sugic, E. Otte, M. R. Dennis, and C. Denz, "Optical second-order skyrmionic hopfion", *Optica* **10**, 725 (2023).

[77] C. He, Y. Shen, and A. Forbes, "Towards higher-dimensional structured light", *Light: Science & Applications* **11**, 205 (2022).

[78] Z. Wan, H. Wang, Q. Liu, X. Fu, and Y. Shen, "Ultra-degree-of-freedom structured light for ultracapacity information carriers", *ACS Photonics* **10**, 2149 (2023).

[79] Y. Shen, "Topological bimeronic beams", *Optics Letters* **46**, 3737 (2021).

[80] V. D'Ambrosio, F. Baccari, S. Slussarenko, L. Marrucci, and F. Sciarrino, "Arbitrary, direct and deterministic manipulation of vector beams via electrically-tuned q-plates", *Scientific Reports* **5**, 7840 (2015).

[81] V. Hakobyan, K. Singh, Y. Lei, P. Kazansky, D. Coursault, A. Forbes, and E. Brasselet, "Single-stage spin-orbit Laguerre-Gaussian modal beam shaping from silica optics", *Physical Review Applied* **21**, 064003 (2024).

[82] J. F. Nye, "Lines of circular polarization in electromagnetic wave fields", *Proceedings of the Royal Society of London. A. Mathematical and Physical Sciences* **389**, 279 (1983).

[83] M. Berry and M. Dennis, "Polarization singularities in isotropic random vector waves", *Proceedings of the Royal Society of London. Series A: Mathematical, Physical and Engineering Sciences* **457**, 141 (2001).

[84] K. Y. Bliokh, M. A. Alonso, and M. R. Dennis, "Geometric phases in 2D and 3D polarized fields: geometrical, dynamical, and topological aspects", *Reports on Progress in Physics* **82**, 122401 (2019).

[85] B. Wang, Z. Che, C. Cheng, C. Tong, L. Shi, Y. Shen, K. Y. Bliokh, and J. Zi, "Topological water-wave structures manipulating particles", *arXiv preprint arXiv:2406.08515* (2024).

[86] A. Rubano, F. Cardano, B. Piccirillo, and L. Marrucci, "Q-plate technology: a progress review", *Journal of the Optical Society of America B* **36**, D70 (2019).

[87] R. C. Devlin, A. Ambrosio, N. A. Rubin, J. B. Mueller, and F. Capasso, "Arbitrary spin-to–orbital angular momentum conversion of light", *Science* **358**, 896 (2017).

[88] P. Ornelas, I. Nape, R. de Mello Koch, and A. Forbes, "Non-local skyrmions as topologically resilient quantum entangled states of light", *Nature Photonics* **18**, 258 (2024).

[89] Y. Shen *et al.*, "Topologically controlled multiskyrmions in photonic gradient-index lenses", *Physical Review Applied* **21**, 024025 (2024).

[90] M. Yessenov, L. A. Hall, K. L. Schepler, and A. F. Abouraddy, "Space-time wave packets", *Advances in Optics and Photonics* **14**, 455 (2022).

[91] Y. Shen *et al.*, "Roadmap on spatiotemporal light fields", *Journal of Optics* **25**, 093001 (2023).

[92] K. Bezuhanov, A. Dreischuh, G. G. Paulus, M. G. Schätzel, and H. Walther, "Vortices in femtosecond laser fields", *Optics Letters* **29**, 1942 (2004).

[93] I. Mariyenko, J. Strohaber, and C. Uiterwaal, "Creation of optical vortices in femtosecond pulses", *Optics Express* **13**, 7599 (2005).

[94] A. Volyar and T. Fadeyeva, "Generation of singular beams in uniaxial crystals", *Optics and Spectroscopy* **94**, 235 (2003).

[95] A. Niv, G. Biener, V. Kleiner, and E. Hasman, "Polychromatic vectorial vortex formed by geometric phase elements", *Optics Letters* **32**, 847 (2007).

[96] Y. Tokizane, K. Oka, and R. Morita, "Supercontinuum optical vortex pulse generation without spatial or topological-charge dispersion", *Optics Express* **17**, 14517 (2009).

[97] V. G. Shvedov, C. Hnatovsky, W. Krolikowski, and A. V. Rode, "Efficient beam converter for the generation of high-power femtosecond vortices", *Optics Letters* **35**, 2660 (2010).

[98] M. Guer, M. Luttmann, J.-F. Hergott, F. Lepetit, O. Tcherbakoff, T. Ruchon, and R. Géneaux, "Few-cycle optical vortices for strong-field physics", *Optics Letters* **49**, 93 (2024).

[99] D. Cruz-Delgado, S. Yerolatsitis, N. K. Fontaine, D. N. Christodoulides, R. Amezcua-Correa, and M. A. Bandres, "Synthesis of ultrafast wavepackets with tailored spatiotemporal properties", *Nature Photonics* **16**, 686 (2022).

[100] M. Piccardo *et al.*, "Broadband control of topological–spectral correlations in space–time beams", *Nature Photonics* **17**, 822 (2023).

[101] M. Soskin and M. Vasnetsov, "Singular optics", *Progress in optics* **42**, 219 (2001).

[102] M. R. Dennis, K. O'Holleran, and M. J. Padgett, "Singular optics: optical vortices and polarization singularities", *Progress in Optics* **53**, 293 (2009).

[103] P.-G. De Gennes and J. Prost, *The physics of liquid crystals* (Oxford university press, 1993), No. 83.

[104] E. Brasselet, "Singular optics of liquid crystal defects", *Liquid Crystals: New Perspectives (eds Pieranski P. and Godinho MH).(Hoboken: John Wiley & Sons, 2021)* 1 (2021).

[105] O. D. Lavrentovich, "Defects and textures of liquid crystals", *Handbook of Liquid Crystals* 1 (2014).

[106] D. Voloschenko and O. Lavrentovich, "Optical vortices generated by dislocations in a cholesteric liquid crystal", *Optics Letters* **25**, 317 (2000).

[107] C. Loussert, U. Delabre, and E. Brasselet, "Manipulating the orbital angular momentum of light at the micron scale with nematic disclinations in a liquid crystal film", *Physical Review Letters* **111**, 037802 (2013).

[108] E. Brasselet, N. Murazawa, H. Misawa, and S. Juodkazis, "Optical vortices from liquid crystal droplets", *Physical Review Letters* **103**, 103903 (2009).

[109] E. Brasselet and C. Loussert, "Electrically controlled topological defects in liquid crystals as tunable spin-orbit encoders for photons", *Optics Letters* **36**, 719 (2011).

[110] E. Brasselet, "Tunable optical vortex arrays from a single nematic topological defect", *Physical Review Letters* **108**, 087801 (2012).

[111] A. Rapini, "Umbilics: static properties and shear-induced displacements", *Journal de Physique* **34**, 629 (1973).

[112] P. Oswald and P. Pieranski, *Nematic and cholesteric liquid crystals: concepts and physical properties illustrated by experiments* (CRC press, 2005).

[113] R. Barboza, U. Bortolozzo, G. Assanto, E. Vidal-Henriquez, M. Clerc, and S. Residori, "Vortex induction via anisotropy stabilized light-matter interaction", *Physical Review Letters* **109**, 143901 (2012).

[114] R. Barboza, U. Bortolozzo, M. Clerc, S. Residori, and E. Vidal-Henriquez, "Light–matter interaction induces a single positive vortex with swirling arms", *Philosophical Transactions of the Royal Society A: Mathematical, Physical and Engineering Sciences* **372**, 20140019 (2014).

[115] E. Brasselet, "Tunable high-resolution macroscopic self-engineered geometric phase optical elements", *Phyical Review Letters* **121**, 033901 (2018).

[116] P. Pieranski, B. Yang, L.-J. Burtz, A. Camu, and F. Simonetti, "Generation of umbilics by magnets and flows", *Liquid Crystals* **40**, 1593 (2013).

[117] J. Gilli, M. Morabito, and T. Frisch, "Ising-Bloch transition in a nematic liquid crystal", *Journal de Physique II* **4**, 319 (1994).

[118] M. Ghadimi Nassiri and E. Brasselet, "Multispectral management of the photon orbital angular momentum", *Phyical Review Letters* **121**, 213901 (2018).

[119] M. Ghadimi Nassiri, G. Seniutinas, C. David, S. Juodkazis, and E. Brasselet, "Spectral optical vortex modulation from geometric phase diamond metasurface arrays", *Applied Physics Letters* **118**, 201104 (2021).

[120] J. Arlt and M. J. Padgett, "Generation of a beam with a dark focus surrounded by regions of higher intensity: The optical bottle beam", *Optics Letters* **25**, 191 (2000).

[121] V. Hakobyan, Y. Shen, and E. Brasselet, "Unitary spin-orbit optical-skyrmionic wave plates", *Physical Review Applied* **22**, 054038 (2024).

[122] V. Hakobyan and E. Brasselet, "Hyperspectral optical orbital angular momentum modulation from tunable structured waveplates", *Optics Letters* **49**, 2089 (2024).